A CRITICAL ASSESSMENT OF THE FINITE ELEMENT METHOD FOR CALCULATING ELECTRIC AND MAGNETIC FIELDS

A Thesis submitted for the degree
of
DOCTOR OF PHILOSOPHY
in
The University of Aston in Birmingham

by

Hamed Ahmad Ibrahim Nasr, B.Sc., M.Sc.

July, 1981 Department of Physics

DEDICATED TO MY WIFE, MARIAM, AND
MY DAUGHTERS, IMAN, INAS AND IKRAM.

A CRITICAL ASSESSMENT OF THE FINITE ELEMENT METHOD FOR CALCULATING ELECTRIC AND MAGNETIC FIELDS

A THESIS
FOR THE DEGREE OF
DOCTOR OF PHILOSOPHY
BY
Hamed Ahmad Ibrahim Nasr

SUMMARY

The present dissertation is concerned with the determination of the magnetic field distribution in magnetic electron lenses by means of the finite element method. In the differential form of this method a Poisson type equation is solved by numerical methods over a finite boundary. Previous methods of adapting this procedure to the requirements of digital computers have restricted its use to computers of extremely large core size. It is shown that by reformulating the boundary conditions, a considerable reduction in core store can be achieved for a given accuracy of field distribution.

The magnetic field distribution of a lens may also be calculated by the integral form of the finite element method. This eliminates boundary problems mentioned but introduces other difficulties.

After a careful analysis of both methods it has proved possible to combine the advantages of both in a new approach to the problem which may be called the 'differential-integral' finite element method. The application of this method to the determination of the magnetic field distribution of some new types of magnetic lenses is described.

In the course of the work considerable re-programming of standard programs was necessary in order to reduce the core store requirements to a minimum. Attention was also paid to special requirements of modern mini-computers which are indispensable in interactive computer-aided design. In addition some new programs have been developed for calculating lens focal properties and aberrations.

Key words: finite element method, magnetic lenses, lens aberrations,
magnetic field distribution, computer-aided design.

ACKNOWLEDGEMENTS

I am most grateful to my supervisor, Professor T. Mulvey, for his help and advice throughout this work.

My thanks are due to my colleagues, Miss S. Al-Hilly and Mr. S. Christofides, for providing their experimental lenses which I used in this work and also for their help in the final preparation of the thesis. I am indebted to Mr. W. James for many useful discussions.

I would like to thank Mr. W. Chen of the Department of Physics, Beijing University, Beijing, Chinese Peoples Republic and Dr. P. W. Hawkes of the Laboratoire d'Optique Electronique du CNRS, Toulouse for many helpful discussions.

I would also like to acknowledge the helpful comments received from Professor J. B. Le Poole of the University of Technology of Delft, Netherlands during the course of investigation.

My thanks are also due to Mr. C. W. Trowbridge of the S.R.C., Rutherford Laboratory, Chilton, Berkshire, for useful discussions and for practical demonstration of the integral form of the finite element method.

Finally, I am very grateful to those of my family who have contributed financial help. In particular, I wish to thank my wife for her patience and encouragement throughout this work.

CONTENTS

LIST OF FIGURES

LIST OF TABLES

LIST OF SYMBOLS

A	Magnetic vector potential
A_θ	Azimuthal component of magnetic vector potential
Area	Area of a triangle
A-t	Ampere turns
B	Magnetic flux density
$B_c(z)$	Axial magnetic flux density due to electric current
$B_m(z)$	Axial magnetic flux density due to magnetisation
B_r	Radial component of magnetic flux density
B_z	Axial component of magnetic flux density
$B_z(z)$	Total axial flux density
C_c	Chromatic aberration coefficient
C_{ci}	Chromatic aberration coefficient referred to image plane
C_{co}	Chromatic aberration coefficient referred to object plane
C_M	Coefficient of chromatic change in magnification
C_{Mi}	Coefficient of chromatic change in magnification referred to image plane
C_{Mo}	Coefficient of chromatic change in magnification referred to object plane
$C_{\theta i}$	Coefficient of chromatic change in image rotation referred to image plane
$C_{\theta o}$	Coefficient of chromatic change in image rotation referred to object plane
C_s	Spherical aberration coefficient
C_{si}	Spherical aberration coefficient referred to image plane
C_{so}	Spherical aberration coefficient referred to object plane
Det	Determinant of triangle = 2.Area
D_{rd}	Radial distortion coefficient

D_{sp}	Spiral distortion coefficient
f_{proj}	Projector focal length
F_{rd}	Radial distortion factor
F_{sp}	Spiral distortion factor
g	Particular Gaussian ray for a system with aperture
G	Asymptotic particular Gaussian ray
h	Particular Gaussian ray for a system with aperture
H	Asymptotic particular Gaussian ray for infinite magnification condition
$\overset{*}{H}$	Magnetic strength (A/m)
$\overset{*}{H}_c$	Magnetic strength due to electric currents
$\overset{*}{H}_m$	Magnetic strength due to magnetic material
I	Energy functional
I_c	Electric current
J	Electric current density
M	Magnification
$\overset{*}{M}$	Magnetisation
$\overset{*}{M}_r$	Radial component of magnetisation
$\overset{*}{M}_z$	Axial component of magnetisation
NI	Excitation of the lens (A-t)
$NI/V_r^{\frac{1}{2}}$	Excitation parameter
P_L	Projection length
s	Particular Gaussian ray for an aperture-free system
t	Particular Gaussian ray for an aperture-free system
V_r	Relativistically corrected accelerating voltage, $V_r = V\ (1 + 0.978 \times 10^{-6}V)$, where V is the applied accelerating voltage of electrons
W	Stored magnetic energy per unit volume
X	Asymptotic particular Gaussian ray for finite conjugate condition

η	Electron charge to mass ratio $\left\|e/m\right\|$
μ_o	Permeability of free space
μ_r	Relative permeability
ρ	Image radius
$\Delta\rho$	Displacement in image position
χ	Magnetic susceptibility
ψ	Magnetic flux

η	Electron charge to mass ratio $\left\|e/m\right\|$
μ_o	Permeability of free space
μ_r	Relative permeability
ρ	Image radius
$\Delta\rho$	Displacement in image position
χ	Magnetic susceptibility
Ψ	Magnetic flux

CHAPTER 1

INTRODUCTION

The finite element method (Zienkiewicz and Cheung, 1965) in the solution of field problems, has proved invaluable in the design of magnetic electron lenses (Munro, 1971). The method was applied in its differential form.

1.1 The differential finite element method:

The magnetic field within a specified region is governed by a differential equation. For rotational symmetric structures that involve current carrying conductors, the differential equation is a Poisson's type equation,

$$\frac{\partial}{\partial z}\left[\frac{1}{\mu_0\mu_r}\frac{\partial A}{\partial z}\right] + \frac{\partial}{\partial r}\left[\frac{1}{\mu_0\mu_r}\left(\frac{\partial A}{\partial r} + \frac{A}{r}\right)\right] + J = 0 \qquad (1.1)$$

where A is called the magnetic vector potential, which will be defined later, μ_0 is the permeability of free space, μ_r is the relative permeability of the magnetic material and J is the electric current density in the current carrying conductors.

In order to solve equation 1.1, the magnetic vector potential must be known at the boundary of the specified region. In general this is not known in advance.

Since some confusion has occurred in the past concerning the correct setting of the boundary condition, it may be useful to recall the mathematical definition of the magnetic vector potential, A, and its relation to the associated property of flux density (B) which can be more readily measured. Figure 1.1 represents the magnetic flux of rotationally symmetric lens. In this case cylindrical coordinates are used. The current in the lens flows azimuthally and therefore has the component J_θ. The vector potential has only the azimuthal component A_θ. Assume a point P at a distance r from the axis of symmetry of the lens. To define the vector potential A_θ at

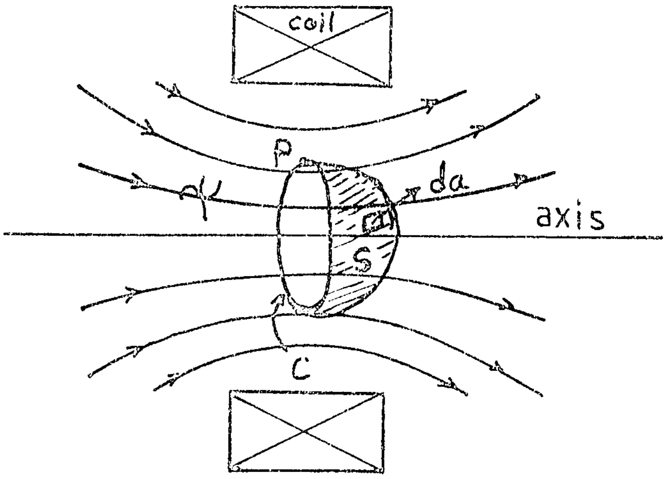

Figure 1.1: Definition of magnetic vector potential, A.

the point P, we assume a surface S whose circular boundary C passes through the point P. The magnetic flux through the surface S is given by,

$$\Psi = \int_S \underline{B} \cdot d\underline{a} \tag{1.2}$$

where $d\underline{a}$ is an element of area of the surface S. Since,

$$\operatorname{div} \underline{B} = 0 \tag{1.3}$$

then $\underline{B}$ can be expressed as the curl of a vector quantity which is called the magnetic vector potential $\underline{A}$.

$$\underline{B} = \text{curl } \underline{A} \tag{1.4}$$

The magnetic flux Ψ through S is then given by,

$$\Psi = \int_S \text{curl } \underline{A} \cdot d\underline{a} \tag{1.5}$$

and from Stokes' theorem,

$$\Psi = \oint \underline{A} \cdot d\underline{l} \tag{1.6}$$

where dl is an element of length of the circle C. So,

$$\Psi = 2\pi r . A_\theta \tag{1.7}$$

and hence the magnetic vector potential A_θ is defined as,

$$A_\theta = \frac{1}{2\pi r} . \Psi \tag{1.8}$$

In general $A_\theta=0$ on the axis and at infinity. Most Gaussmeters in fact measure the quantity Ψ over a small area Δ a.

In the differential finite element method, the differential equation 1.1 is solved by the minimisation of an appropriate energy functional which is given, over a region S, by

$$I = 2\pi \iint_S (W - JA) \; r \; dz \; dr \tag{1.9}$$

subject to the same boundary conditions. For a derivation of equation 1.9 see Appendix 1. W is the stored magnetic energy per unit volume, i.e. the work per unit volume required to produce a final magnetic flux density B. For a non-linear magnetic material, W is given (Pugh and Pugh, 1970) by

$$W = \int_0^B \overset{*}{\underline{H}} \cdot d\underline{B} = \frac{1}{\mu_o}\int_0^B \frac{B}{\mu_r} \cdot dB \qquad (1.10)$$

where H is the magnetic intensity.

W is shown as the shaded area in Figure 1.2. For a linear magnetic material, W is given by,

$$W = \frac{B^2}{\mu_o\mu_r} \qquad (1.11)$$

as shown by the shaded area in Figure 1.3. It can be shown (Appendix 2) that the minimisation of equation 1.9 is equivalent to solving the Poisson equation 1.1. The minimisation of the functional 1.9 is carried out by the finite element method. Figure 1.4 represents the cross-section of an axially symmetric magnetic structure; this includes the current carrying coil, the magnetic material and the space around it within the outer rectangular boundary abcd. Because of this symmetry, the functional 1.9 is minimised over the area defined by the boundary az_1z_2d where the axis of symmetry constitutes one side of this boundary and extends between the distances z_1 and z_2.

The structure is divided into a grid of quadrilaterals. The boundary of the coil and the magnetic material have to coincide with a grid line. Furthermore each quadrilateral is subdivided into two triangular finite elements. This can be carried out in two ways. A lattice of nodes is formed; at each inner side node the vertices of six triangular elements meet as shown in Figure 1.5a. An alternative arrangement is shown in Figure 1.5b, where the finite elements are

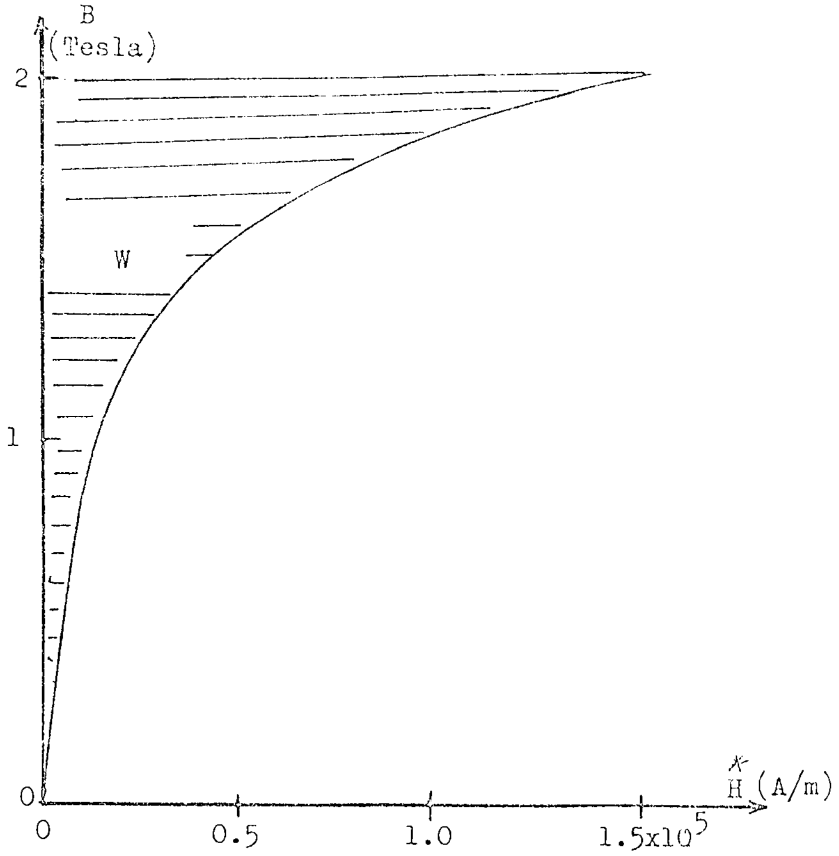

Figure 1.2: The B-$\overset{*}{H}$ curve for a non-linear magnetic material. W is the stored energy per unit volume of the magnetic material.

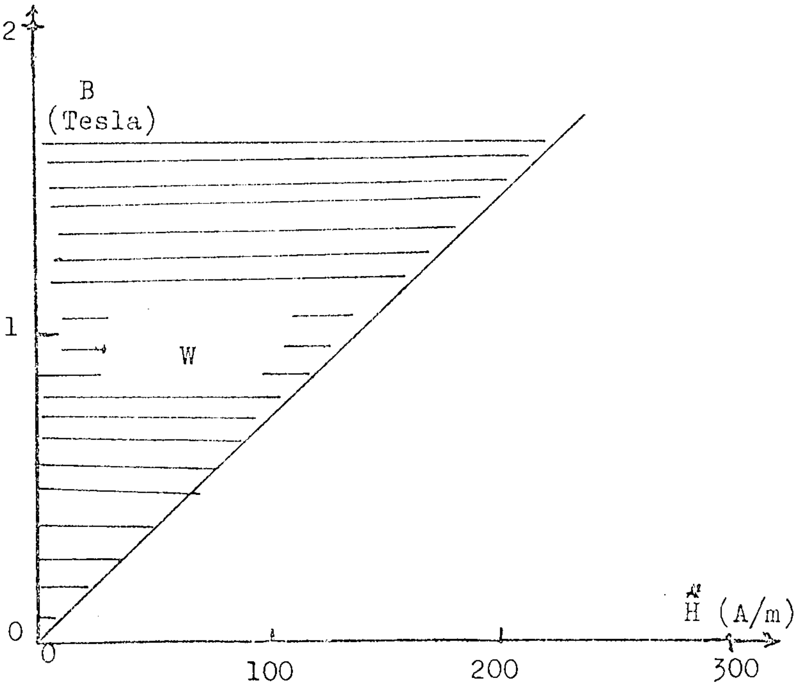

Figure 1.3: The B-$\overset{*}{H}$ curve for a linear magnetic material. W is the stored energy per unit volume of the magnetic material, $W=\frac{1}{2}HB$.

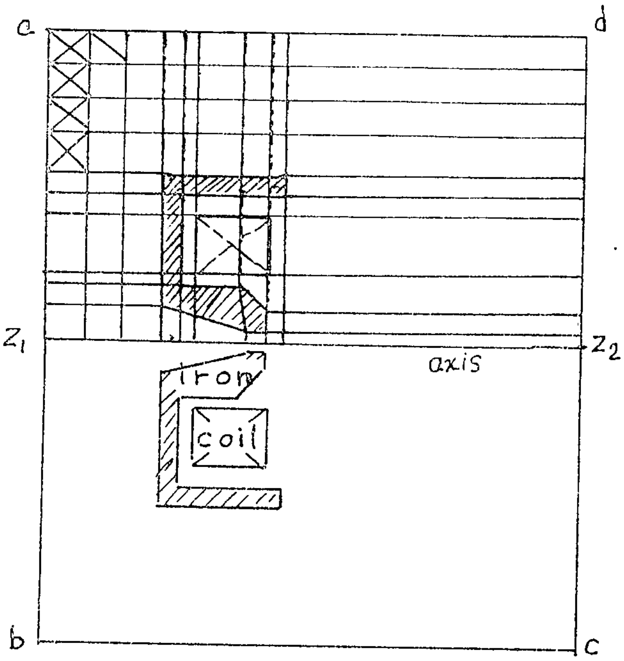

Figure 1.4: Cross-section of an axially symmetric magnetic structure; this includes the current carrying coil, the magnetic material and the space around it within the rectangular boundary abcd. The finite element boundary is az_1z_2d. Dividing the structure into quadrilaterals and triangular finite elements.

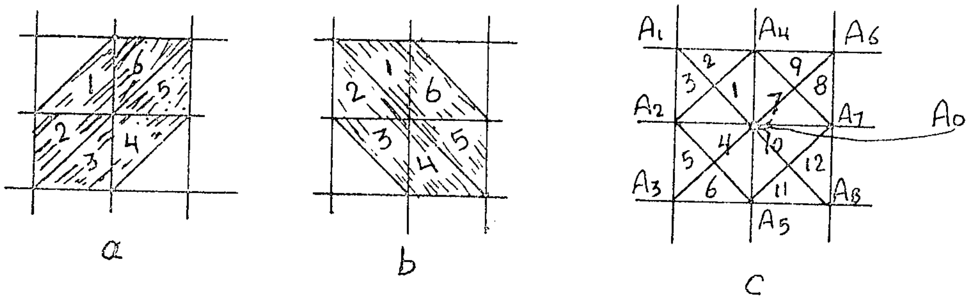

Figure 1.5: Subdivision of quadrilaterals into triangular finite elements. a) one possible way, b) alternative way c) combination of a and b for better accuracy. The vector potential at the node A_0 is affected by the eight vector potential values at the other vertices of the triangles, A_1, A_2 ....A_8. A nine point equation is formed at the node.

formed across the other diagonals; this gives the same nodal points but with six different triangles. Accuracy can be improved by combining arrangements a and b as shown in Figure 1.5c. This gives the same nodal arrangements but with twelve triangles in contact with each node. At each node the contribution to the functional 1.9 now comes from twelve triangles thereby improving the accuracy of the calculation. This arrangement leads to a nine point equation for each node in terms of the vector potentials at the node and the eight vector potential values at the other vertices of the triangles in contact with the node as shown in Figure 1.5c. The values of the known vector potentials at the boundary are substituted and the equations are solved for the unknown vector potentials at each node.

The derivation of the nodal equations given in Munro's Ph.D. thesis (1971) was presented in a form that was inconvenient for a complete revision of the finite element program. Hence it proved necessary to rederive these nodal equations and to present them in the more convenient form given in Appendix 3.

The two components of the magnetic flux density (radial B_r and axial B_z) can be defined by considering Figure 1.6. Consider a cylindrical element of radius r and length dz around the axis of symmetry. The radial flux through the surface with boundary abcd is given by the line integral of A over the boundary abcd, where we put A for A_θ. So,

$$(d\Psi)_r = B_r \cdot rd\theta.dz = (\Psi)_z - (\Psi)_{z+dz}$$

$$= (A.rd\theta)_z - (A.rd\theta)_{z+dz} \qquad (1.12)$$

and hence for B_r we have,

$$B_r = -\frac{\partial A}{\partial z} \tag{1.13}$$

The axial flux $(d\Psi)_z$ through the surface dcef is given by,

$$(d\Psi)_z = B_z .rd\theta.dr = (\Psi)_{r+dr} - (\Psi)_r$$

$$= (A.rd\theta)_{r+dr} - (A.rd\theta)_r \tag{1.14}$$

and hence for B_z we have,

$$B_z = \frac{1}{r}\frac{\partial(rA)}{\partial r} \tag{1.15}$$

Knowing the vector potential at each node, the flux density over each element and the flux values can be calculated using equations 1.13 and 1.15 as shown in Appendix 4. In particular, the axial flux density can be calculated from the values of the potentials near the axis. At a point P on the axis (Figure 1.7), the axial flux density $B_z(z)$ is given by,

$$B_z(z) = \frac{2(A_1 r_2^3 - A_2 r_1^3)}{r_1 r_2 (r_2^2 - r_1^2)} \tag{1.16}$$

The differential finite element method of calculating magnetic fields began to be applied in the 1970's. Thus the method was applied to the solution of saturable magnetic field problems (Silvester and Chari, 1970). In electron optics the method was applied to the design of magnetic electron lenses by Munro (1971). A set of computer programs (Munro, 1975) stemming from this work is already widely in use.

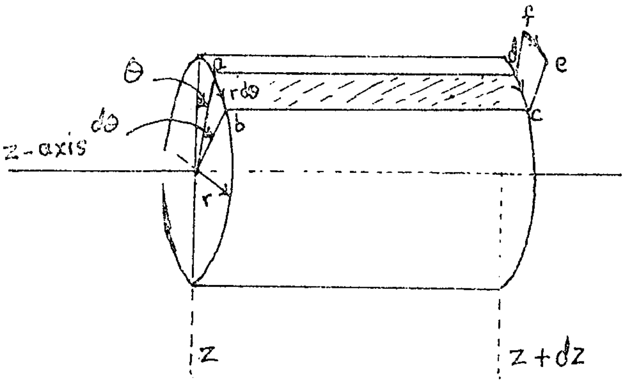

Figure 1.6: Definition of the magnetic flux density components B_r and B_z. The figure represents a cylindrical element of radius r and length dz around the axis of symmetry.

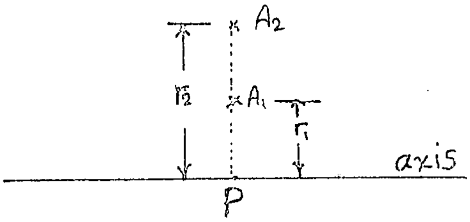

Figure 1.7: Point P at which axial flux density $B_z(z)$ is to be calculated from near axis vector potential values.

Up to this point, we have assumed that the values of the vector potential at the outer boundary are known. In general these are known only at the axis where A=0, because of axial symmetry, or at infinity where A is also zero (see equation 1.8). Unfortunately an infinite boundary cannot be represented in a computer. Even with a distant boundary, the resulting increase in computer core requirements may be difficult to achieve in presently available computers.

At a finite boundary, the vector potential cannot in general be specified in advance, especially for magnetic lenses, whose fields may extend well beyond the lens structure. The best that can be done is to choose an arbitrary boundary in a region where the magnetic flux crossing it is a negligible fraction of the total flux produced by the lens. The vector potential is set to zero along this boundary. From this it is clear that an exact solution for a magnetic lens in free space is in principle impossible, within a finite boundary. In order to illustrate the above points, consider a magnetic lens (Figure 1.8) that consists of a simple iron-free coil of rectangular cross-section having an excitation of 500 A-t. The axial field distribution can readily be calculated analytically from the Biot-Savart law as shown in Figure 1.8. The field from this lens obeys Ampere's circuital law, namely that the line integral of the field strength $\overset{*}{H}(=B/\mu_o\mu_r)$ over any closed path is equal to the net current across the area bounded by the path. Therefore for a path ℓ that encloses the coil windings,

$$\frac{1}{\mu_o}\oint\frac{B}{\mu_r}\cdot d\underline{\ell} = NI \tag{1.17}$$

where NI is the A-t of the lens. Since this line integral is independent of the path chosen and depends only on the relevant

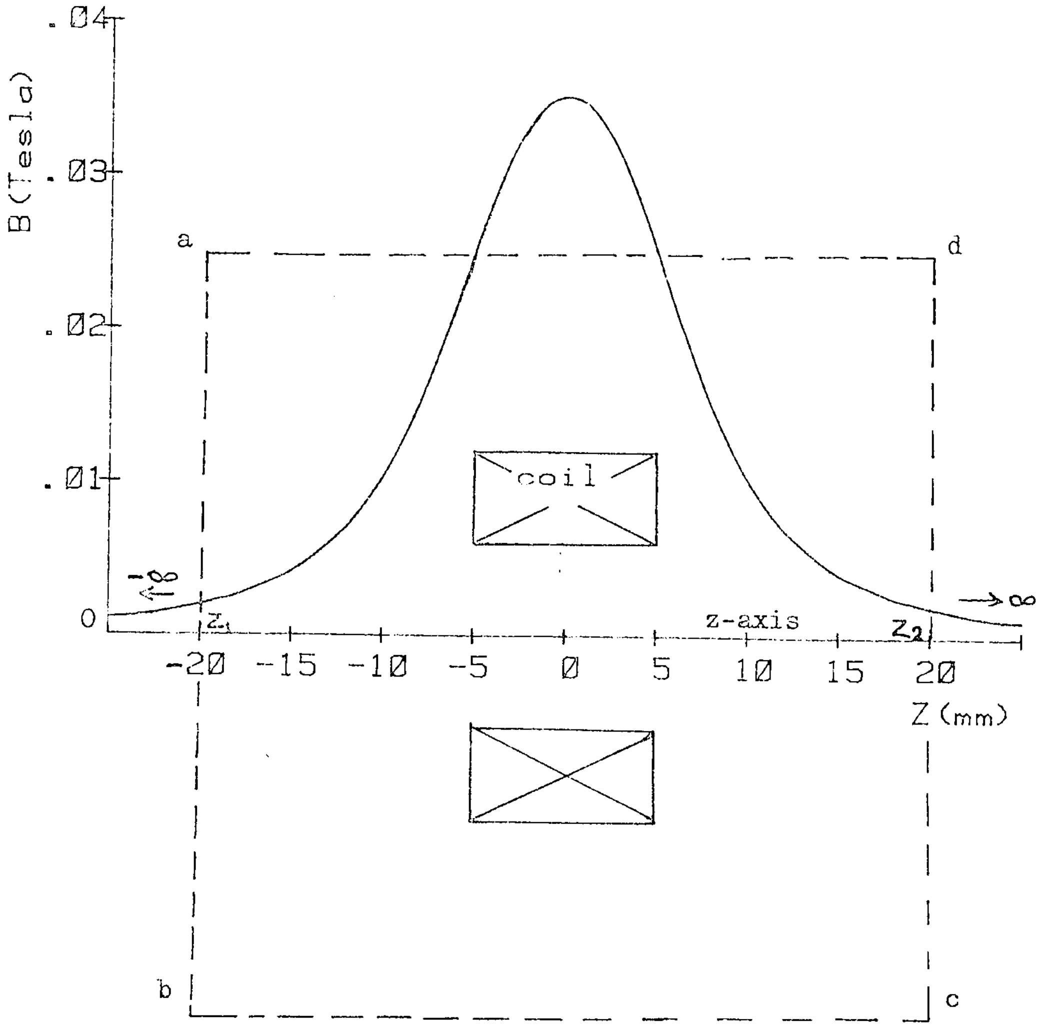

Figure 1.8: Calculated axial field distribution using the Biot-Savart law, for a magnetic lens consisting of a simple iron-free coil of rectangular cross-section. The field extends to infinity from both directions on the z-axis.

current NI, it may be used as a check on the accuracy of any mathematical method used to calculate the field distribution. In particular it can be used to check the axial field distribution. In this case equation 1.17 can be expressed as,

$$\frac{1}{\mu_0}\int_{-\infty}^{\infty}\frac{B_z(z)}{\mu_r}\,dz = NI \qquad (1.18)$$

where the path is chosen over the z-axis and it extends to infinity from both directions, $-\infty \leqslant z \leqslant \infty$.

In order to calculate the field distribution of the lens of Figure 1.8 by the differential finite element method we have to specify a finite boundary where we can put A=0 without introducing appreciable error. This condition can be realised physically in only two situations. Firstly, if the boundary abcd is a surface of a superconducting sheet surrounding the lens. It should be noted however that the presence of such a superconducting boundary may alter the magnetic field distribution of the lens compared with that in free-space. As an illustration of this, the axial field distribution of the lens shown in Figure 1.8, but surrounded by a superconducting sheet, was calculated by the differential finite element method. Here A was set to zero on a finite boundary placed just outside the superconducting sheet as shown in Figure 1.9. The thickness of the sheet was 5mm. The relative permeability μ_r of the superconducting material was taken to be 10^{-9}, a value sufficiently close to zero for computational purposes. The calculated axial field is indicated by the crosses in Figure 1.9. The field strength $\overset{*}{H}(=B_z(z)/\mu_0\mu_r)$ distribution is indicated as a solid line in Figure 1.9; the excitation calculated from this distribution yields the supplied excitation to the lens (NI). This distribution is correct but it does not correspond to the distribution in free space. However the excitation in the superconducting sheet accounts for more than 25 % of the lens excitation.

Secondly, the lens may be surrounded by magnetic material of infinitely high permeability. For conventional lenses this condition is more or less satisfied in practice by the iron shell. It should perhaps be noted that all the magnetic lenses initially calculated by Munro (1971) were of this character. The axial field distribution of the lens shown in Figure 1.8, but surrounded by an iron sheet of high relative permeability (μ_r=10^9), was then recalculated by the differential finite element method. Here A was set to zero on a finite boundary just outside the iron sheet as shown in Figure 1.10. As before, the thickness of the iron sheet was 5mm. The calculated axial flux density distribution $B_z(z)$ is indicated by the crosses in Figure 1.10. The field strength $\overset{*}{H}(=B_z(z)/\mu_o\mu_r)$ distribution is shown as a solid line in Figure 1.10; the excitation calculated from this distribution agrees with the excitation supplied to the lens (NI). It should be noted that no ampere turns are lost in the iron circuit. However, if the iron circuit is removed the flux density distribution will change.

Ideally, one should carry out the field calculation using the actual iron or superconducting boundary that will be encountered in practice. However, it is more usual and convenient to calculate the field distribution of the lens in free space, at least in the initial calculations. In this case one should be aware of the dangers of setting A=0 on a finite boundary. It should also be noted that, in general, the field distribution will be <u>different</u> depending on whether the boundary is composed of iron or a superconducting material.

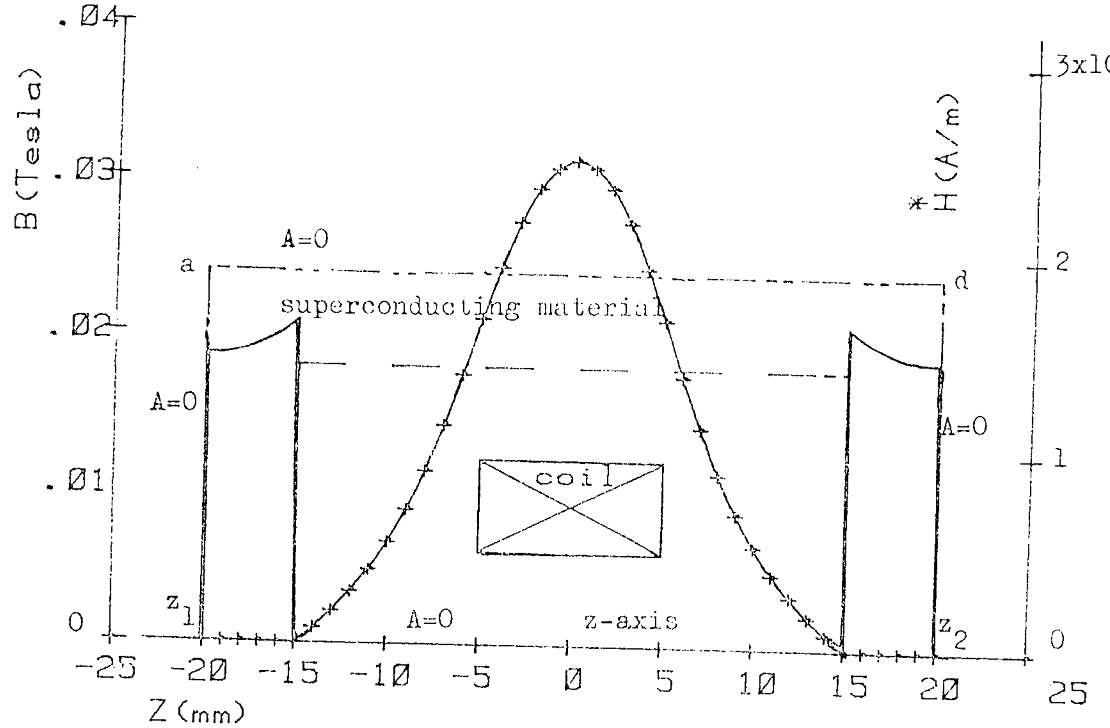

Figure 1.9: Axial flux density distribution (+++) for the lens shown in Figure 1.8 (excitation 500 A-t), but surrounded by a superconducting sheet and field strength $\overset{*}{H}(=B_z^{(z)}/\mu_o\mu_r)$ distribution (——). Excitation in superconductor = 153 A-t and excitation in free-space = 347 A-t.

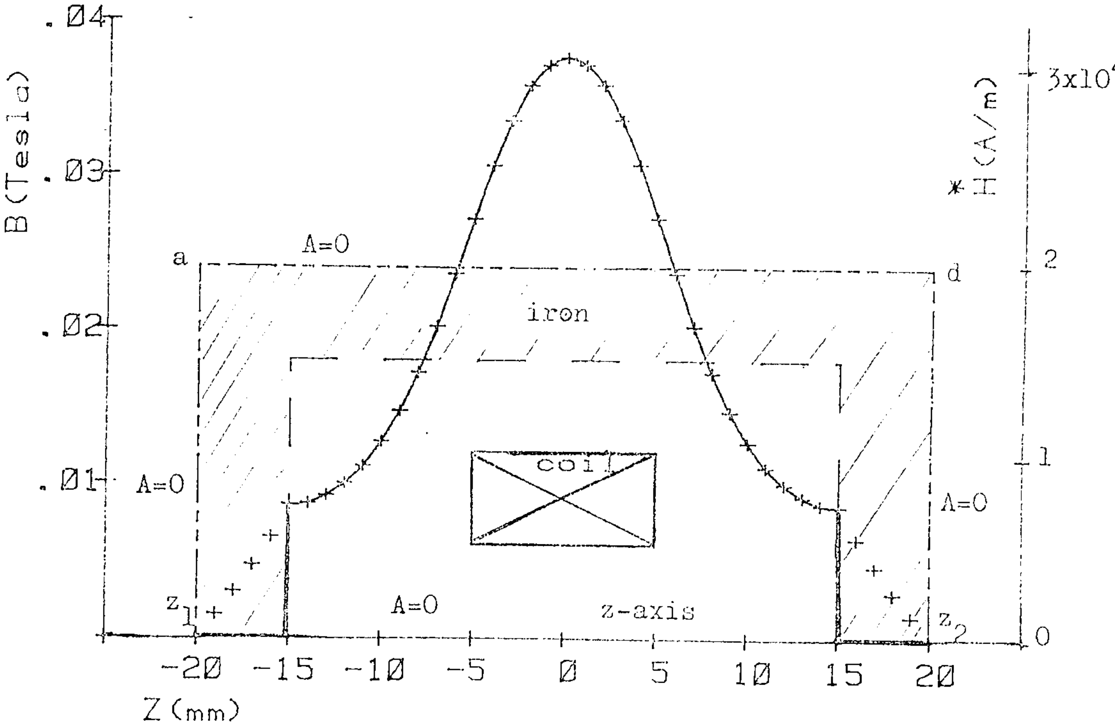

Figure 1.10: Axial flux density distribution (+++) for the lens shown in Figure 1.8 (excitation 500 A-t), but surrounded by an iron sheet of infinite permeability and field strength $\overset{*}{H}(=B_z^{(z)}/\mu_o\mu_r)$ distribution (——). Note. No ampere-turns are lost in the iron circuit. Excitation in free-space = 500 A-t.

It should be noted that the field on the axis obtained by averaging these two results gives a better accuracy than either of them taken alone as can be seen in Figure 1.11.

In order to illustrate the effect of a finite boundary with A=0, consider the lens shown in Figure 1.12; this is identical with that shown previously in Figure 1.8 but now the boundary is set at 20mm from the lens centre. The axial field distribution calculated from the differential finite element method is shown as a dotted line in Figure 1.12. One may be tempted to calculate the excitation of the lens from this distribution as,

$$\frac{1}{\mu_o}\int_{z_1}^{z_2}\frac{B_z(z)}{\mu_r}dz = (NI)_{calc.} \qquad (1.19)$$

where z_1=-20mm and z_2=20mm.

An inspection of Figure 1.12 shows that $(NI)_{calc.}$ as given by equation 1.19 is less than NI calculated from the Biot-Savart distribution (solid line). The difference in excitation $\delta(NI)_{calc.}$ is given by,

$$\delta\,(NI)_{calc.} = NI - (NI)_{calc.} \qquad (1.20)$$

and is represented by the shaded area in Figure 1.12. This indicates that some excitation has been lost from the axial field distribution. In the past this has been ascribed to computing error or to some unknown cause. The present investigation has shown, however, that this 'loss' of ampere turns arises from the presence of low permeability boundary. This can be illustrated by reference to Figure 1.9 in which the field strength H across the boundary is included in the figure; the excitation 'lost' in the superconducting boundary in this

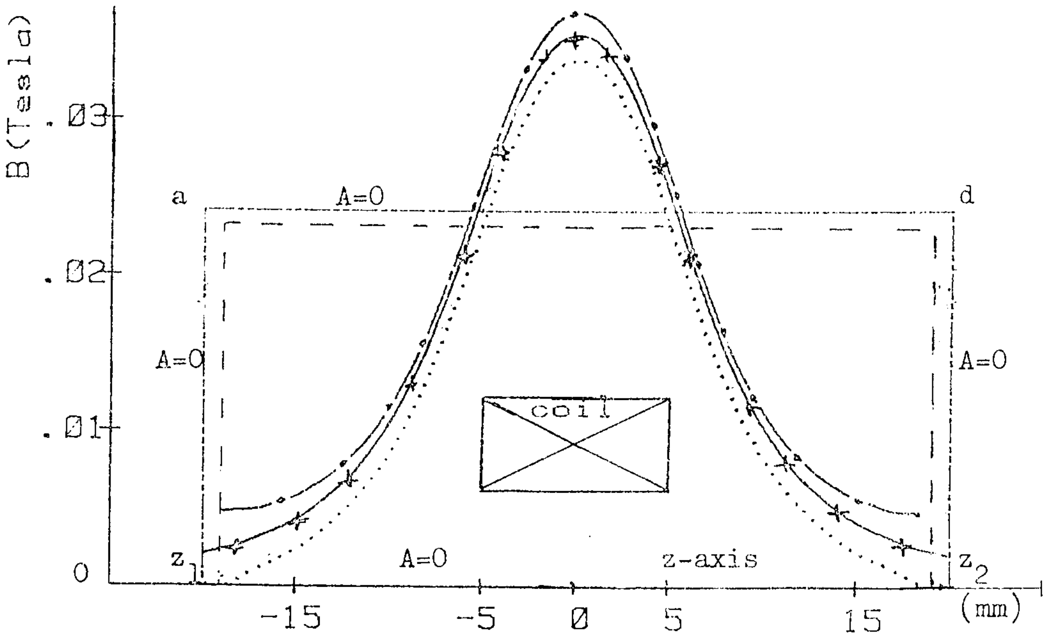

Figure 1.11: Axial flux density distribution of the lens of Figure 1.8, calculated by (a) the Biot-Savart law (——), (b) the differential finite element method (—.—) with a sheet of infinitely high permeability surrounding the lens, (c) the differential finite element method (...) with a superconducting sheet surrounding the lens. The crosses (+++) denote the average of the (...) and (—.—) distributions.

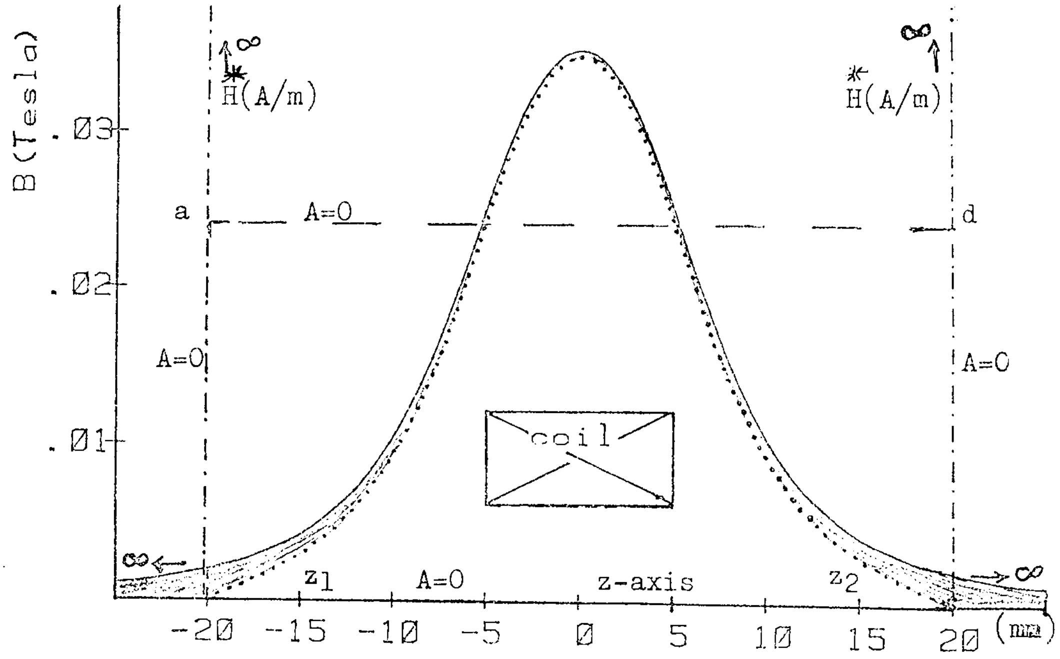

Figure 1.12: Effect of a finite boundary with A=0 on the axial field distribution of the lens of Figure 1.8; (excitation 500 A-t) calculated by (a) the differential finite element method (...), (b) the Biot-Savart law (——). The vertical (—.—) lines at z=-20mm and z=20mm represent the field strength H at the boundary. The shaded area represents the excitation 'lost' to the axial field distribution and transferred to the boundary.

case was 153 A-t. As the superconducting sheet gets thinner, for a fixed inner boundary, the excitation in the superconductor remains essentially the same, although the field strength $\overset{*}{H}$ distribution increases to large values. The flux density $B_z(z)$ on the other hand is essentially zero. The axial flux density distribution in free space remains unchanged as the boundary decreases in thickness, the excitation stays constant at 347 A-t. In the limit, as the superconducting sheet gets infinitely thin, the $\overset{*}{H}$ field becomes infinitely high. The integral $\int \overset{*}{H}\, dz$ taken across the superconducting boundary still yield a finite excitation of 153 A-t.

$$\int\limits_{\substack{\text{across the}\\ \text{superconducting}\\ \text{boundary}}} \overset{*}{H}\, dz = 153 \text{ A-t} \tag{1.21}$$

The finite boundary used in the differential finite element method can thus be assumed to be an infinitely thin superconducting boundary with an infinite axial field strength H. Hence the 'lost' ampere-turns can be found in this boundary. Care must therefore be taken in interpreting the calculated axial field distribution in the absence of such a boundary. Here we shall call these 'lost' ampere turns, the 'boundary loss' in excitation. This 'boundary loss' in excitation can be expressed as a percentage of $\delta(NI)_{calc.}$ with respect to NI, i.e.,

$$\text{'boundary loss'} = 100 \cdot \frac{\delta(NI)_{calc.}}{NI} \% \tag{1.22}$$

As can be seen from Figure 1.12 the axial flux density distribution, calculated by the differential finite element method, cannot be put right by multiplying the whole distribution by the 'boundary loss' factor. The errors in the calculated field are high near the boundary and infinite at the boundary. However even with this finite boundary, the axial field distribution in the central region of the structure and remote from the finite boundary has good accuracy. This can be made use of later in chapters 2 and 3 to provide more accurate field distributions.

1.2 Desirable features of a numerical method for magnetic field calculations:

When applying a numerical method such as the finite element method for calculating the fields of magnetic electron lenses we expect the following requirements to be satisfied.

The magnetic field distribution and in particular the axial distribution should be known to an accuracy of 1 % . However, where the axial field falls below 1 % of the peak value larger errors may be tolerated without affecting the calculations of the optical properties. Moreover, the axial field distribution should be a smooth curve which guarantees the accuracy of the derivatives $dB_z(z)/dz$ and $d^2B_z(z)/dz^2$ from this curve in order to calculate the aberration coefficients. The 'boundary loss' in excitation should be better than 10% in order not to face practical difficulties in power supplies especially for very high energy electron lenses.

For single-polepiece lenses, setting the boundary condition becomes important since parts of the magnetic circuit are open and may lead to errors already discussed in connection with Figure 1.8. In practice, a compromise has to be made between accuracy of the field and available core store. An improved differential finite element method will be presented in Chapter 2, which can achieve a required accuracy for single-polepiece lenses but with a reduced core requirement.

1.3 Advantages of the Munro program (1971):

When applied to conventional magnetic electron lenses (Munro, 1973), the finite element method in the differential form can calculate the flux density in all parts of the lens; including parts where it would be difficult to measure the flux density experimentally. The field calculation of a magnetic electron lens requires the knowledge of the lens geometry, excitation of the coil (ampere turns) and the magnetic properties of the magnetic material. Hence the construction and experimental testing of trial lenses is dramatically reduced. The shape of the polepieces and other parts of the magnetic circuit can be changed easily in the computer in order to reach a satisfactory design for the specified application of the lens. The permeability of the magnetic material is specified at all parts of the structure and hence no special arrangements are needed at the boundaries of elements of different permeabilities. This is not the case in the other numerical finite difference method where it is often difficult to satisfy the boundary conditions, eg. between coil or free space and magnetic circuit. This also makes the finite element method more convenient for dealing with saturation conditions where μ_r has to be calculated for each element in each iteration process.

A critical and objective comparison between the differential finite element and finite difference methods has not been published in the literature. Kasper and Lenz (1980), have suggested that, in principle, better accuracies can be achieved using the finite difference method especially for axial field distributions than that are possible with the differential finite element method, for a given number of nodes. But since the two methods are different in mathematical formulation, a fair comparison is difficult to achieve. For example, a comparison based on the same mesh distribution may in fact tend to favour one method unduly. The chief difficulty in comparing these two methods in practice is the lack of a suitable general program for calculating magnetic and electric fields by the finite difference method. If one became available it would be a straightforward matter to calculate the axial field distribution of a number of lenses and compare these directly. A step in the right direction has been taken by Denegri et al (1976) who developed a finite difference method that employs a similar mesh distribution to that of the differential finite element method. Some initial results have been obtained but the method has not yet been fully implemented to the point where conclusive results can be obtained.

It should also be mentioned that the field distribution in superconducting lenses also can be calculated readily by the differential finite element method; the superconducting material is simply characterised by a relative permeability $\mu_r = 0$.

1.4 Limitations of the Munro program (1971):

In the above program, the magnetic structure including the surrounding free space within the finite boundary has to be divided into finite elements. These should be sufficiently small in order to achieve adequate accuracies. The vector potential values along the finite boundary have to be set to zero. As can be seen from equation 1.8, this can be true at an infinite radius or when $\Psi = 0$, as explained previously.

The program works well and high accuracies can be obtained for conventional magnetic electron lenses. For open structures or for other type of magnetic lenses, such as the single-polepiece lens, putting A=0 on a finite boundary that does not consist of a superconducting material or a material of infinite permeability will be considered by the program as surrounded by a superconducting boundary. In other words the program will work correctly but it will solve a different problem from the one that the user has in mind. In particular, there will be 'boundary loss' in the excitation calculated from the axial flux density distribution. In addition the shape of the field distribution will be incorrect. This fact that one is forced to put A=0 on a finite boundary constitutes a serious limitation of the above program (Mulvey and Nasr, 1980a. cf. Appendix 8) and may mislead the unwary. For example, in a calculation of a single-polepiece lens (Hill and Smith, 1980) using 25X50 mesh points, the 'boundary loss' was about 26 % . Increasing the number of meshes to 60X120 reduced the 'boundary loss' to 8 % , but increased the store requirement by a factor of thirteen indicating that the boundary problem has not been completely solved. In chapter 2, we present an improved differential finite element method program that reduces the effect of the limitations stated above and greatly improves the accuracy of the vector potential calculations. Some application of the method have already been published (Mulvey and Nasr, 1980b, 1981. cf. Appendices 9 and 10).

1.5 The integral finite element method:

The finite element method expressed in integral form (Newman et al, 1972) can equally be applied to the calculation of magnetic fields. Here only the magnetic material is divided into finite elements; the magnetisation is assumed constant over each element. The field strength $\overset{*}{H}_c$ due to the currents in the coil windings and the field strength $\overset{*}{H}_m$ due to the magnetisation in the iron elements are each found directly and added to give the total field strength $\overset{*}{H}$ at any point,

$$\overset{*}{H} = \overset{*}{H}_c + \overset{*}{H}_m \tag{1.23}$$

The field $\overset{*}{H}_c$ can be found easily by the Biot-Savart law,

$$\overset{*}{H}_c = \frac{1}{4\pi} \int \frac{\underline{J} \ X \ \underline{r}}{r^3} \ dV \tag{1.24}$$

where $\underline{J}$ is the current density in the coil windings and the integral is carried out over the volume of the coil windings.

The field $\overset{*}{H}_m$ can be expressed analytically as,

$$\overset{*}{H}_m = - \frac{1}{4\pi} \ \mathrm{grad} \int \frac{\underline{\overset{*}{M}} \cdot \underline{r}}{r^3} \ dV \ . \tag{1.25}$$

The integral is carried out over the whole of the iron region. The magnetisation $\overset{*}{M}$ at each element is related to the field strength $\overset{*}{H}$ by,

$$\overset{*}{M} = (\mu_r - 1) \ \overset{*}{H} = \chi \ \overset{*}{H} \tag{1.26}$$

where χ is the susceptibility of the magnetic material. In terms of the flux density $B(=\mu_o \mu_r \overset{*}{H})$, the magnetisation $\overset{*}{M}$ is given by,

$$\overset{*}{M} = \frac{B}{\mu_o} \ (1 - \frac{1}{\mu_r}) \tag{1.27}$$

From equations 1.23 and 1.25 we have,

$$\overset{*}{H} = \overset{*}{H}_c - \frac{1}{4\pi} \ \mathrm{grad} \int \frac{\underline{\overset{*}{M}} \cdot \underline{r}}{r^3} \ dV \tag{1.28}$$

If the magnetic material is divided into N finite elements, we get N similar equations which can be written in the general form

$$\overset{*}{H}_i = \overset{*}{H}_{ci} + \sum_{j=1}^{N} K_{ij} \chi_j \overset{*}{H}_j \qquad (1.29)$$

where i=1,2,..., N; and K_{ij} are factors that depend on the geometry of the field points. For example, with two iron elements 1 and 2, as shown in Figure 1.13 we obtain the two equations,

$$\begin{aligned} \overset{*}{H}_1 &= \overset{*}{H}_{c1} + K_{11} \chi_1 \overset{*}{H}_1 + K_{12} \chi_2 \overset{*}{H}_2 \\ \overset{*}{H}_2 &= \overset{*}{H}_{c2} + K_{21} \chi_1 \overset{*}{H}_1 + K_{22} \chi_2 \overset{*}{H}_2 \end{aligned} \qquad (1.30)$$

In two dimensional Cartesian coordinates, each element of K_{ij} will have two components. Hence for N finite elements a set of 2N simultaneous equations are generated. If the susceptibility χ_j at the j^{th} element were known the 2N equations could be solved directly for the $\overset{*}{H}_{ix}$ and $\overset{*}{H}_{iy}$ components of $\overset{*}{H}$. If the χ_j values are not known then an iterative process must be used in which initial values of χ_j are assumed. The equations are then solved for $\overset{*}{H}_{ix}$ and $\overset{*}{H}_{iy}$ and the values of χ_j are subsequently adjusted using a table of $\chi/\overset{*}{H}$ values. The process is repeated until a prescribed degree of convergence is achieved. Depending on the number of iron elements involved and the degree of saturation, a convergence to about 1 % of the maximum value of the field requires twenty to one-hundred iterations. The components $\overset{*}{M}_x$ and $\overset{*}{M}_y$ of the magnetisation are then calculated from the resulting values $\overset{*}{H}_{ix}$ and $\overset{*}{H}_{iy}$. Hence the field $\overset{*}{H}_m$ due to the iron at any point can be calculated from equation 1.25 and added to to the field $\overset{*}{H}_c$ from the coil windings to give the total field $\overset{*}{H}$.

The axial flux density distribution $B_z(z)$ of a magnetic lens is of particular interest because it is the one that is usually used for the calculation of optical properties of the lens. Hence it may be instructive to show how the total axial field $B_z(z)$ on the axis can be calculated at any point, P, from both the current in the coil windings and the known magnetisation values $\overset{*}{M}_z$ and $\overset{*}{M}_r$ in the iron elements. $B_z(z)$ at any point on the axis is given by,

$$B_z(z) = B_c(z) + B_m(z) \tag{1.31}$$

where $B_c(z)$ is the axial flux density at the point P due to the current in coil windings and $B_m(z)$ is the axial flux density due to the magnetisation in iron elements.

<u>Axial flux density distribution</u> $B_c(z)$ <u>due to the current in coil windings</u>:

The axial flux density $B_c(z)$ due to the current in coil windings can be derived from the axial flux density of a current loop of radius r and carrying a current I_c, Figure 1.14. The axial flux density at a point P on the axis of a circular loop is given by the Biot-Savart law as,

$$\left[B_c(z)\right]_{loop} = \mu_0\mu_r \frac{I_c\, r^2}{2(r^2+z^2)^{3/2}} \tag{1.32}$$

where z is the axial distance of the point P from the centre of the loop. For a coil with rectangular cross-section and excitation NI A-t, and after some mathematical manipulation, we have

$$B_c(z) = \frac{\mu_0\mu_r NI}{4h(r_2-r_1)}\left[(z+h)\ \ln\frac{\tan(\frac{\pi}{4}+\frac{\alpha_1}{2})}{\tan(\frac{\pi}{4}+\frac{\alpha_0}{2})} - (z-h)\ \ln\frac{\tan(\frac{\pi}{4}+\frac{\beta_1}{2})}{\tan(\frac{\pi}{4}+\frac{\beta_0}{2})}\right] \tag{1.33}$$

where h, r_1, r_2, α_0, α_1, β_0, and β_1 are as shown in Figure 1.15.

For a coil of arbitrary shape, Figure 1.16, the field at point P on the axis is calculated as the contribution of several current loops. The coil is divided into a number of circular elements,

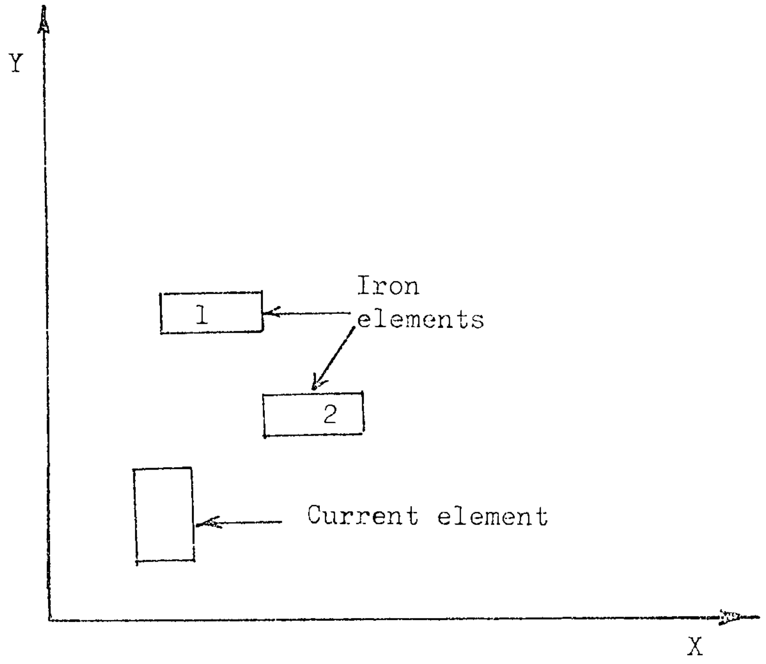

Figure 1.13: Geometry of a magnetic structure with two iron elements and one current element.

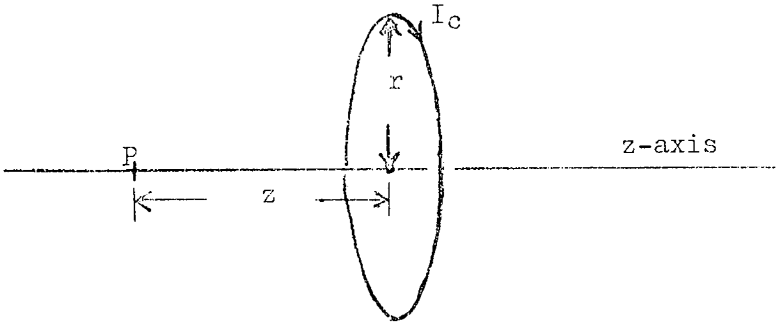

Figure 1.14: Axial flux density at a point P on the axis of a circular loop of radius r and carrying a current I_c.

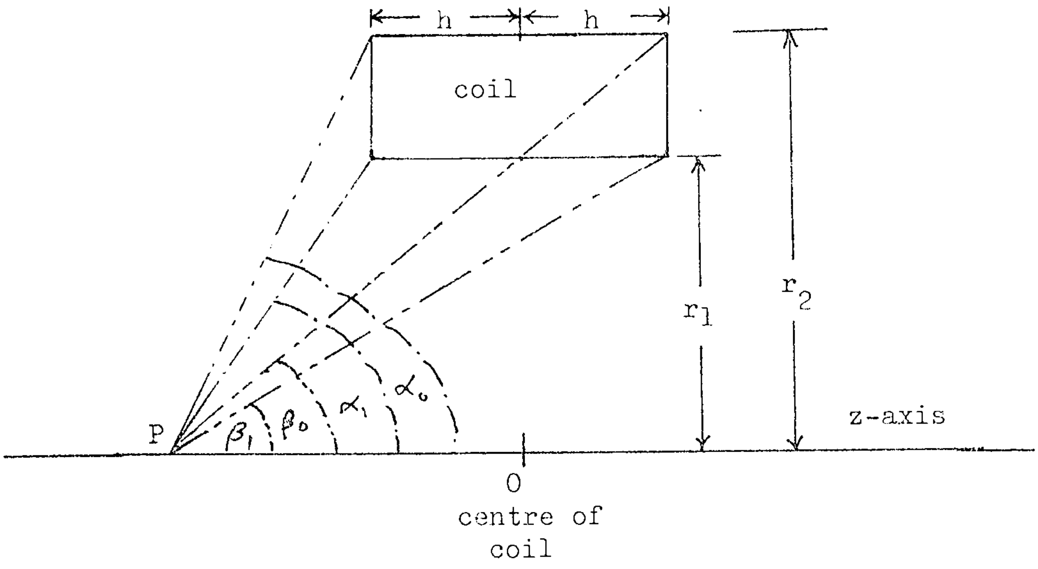

Figure 1.15: Axial flux density $B_c(z)$ from a coil of rectangular cross-section at a point P on the axis.

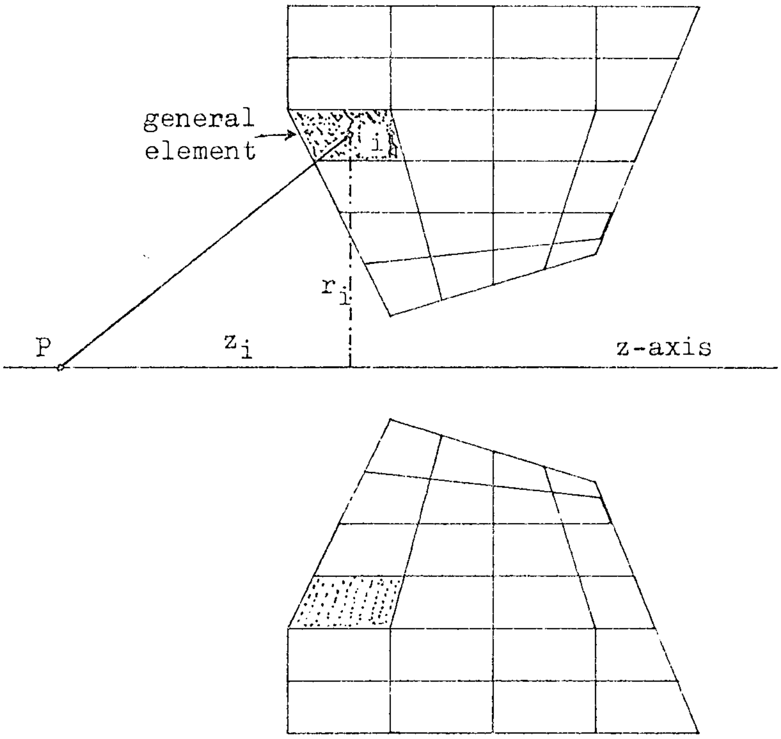

Figure 1.16: Axial flux density $B_c(z)$, due to a coil of arbitrary shape and currying an electric current, at a point P on the axis.

whose cross-section form a grid of quadrilateral elements. For a general element i, the current is given by,

$$(I_c)_i = (J)_i . (\text{area})_i \qquad (1.34)$$

where $(J)_i$ is the current density of the i^{th} element whose area is $(\text{area})_i$. The radius of this element is r_i and the axial distance of its centre from the point P is z_i. The axial flux density $\left[B_c(z)\right]_i$ at the point P from the i^{th} element is given by,

$$\left[B_c(z)\right]_i = \mu_0 \mu_r \frac{(I_c)_i \, r_i^2}{2(r_i^2 + z_i^2)^{3/2}} \qquad (1.35)$$

The total contribution from the coil to the flux density at any axial point P is given by:

$$B_c(z) = \sum_i \left[B_c(z)\right]_i \qquad (1.36)$$

Equation 1.36 forms the basis for calculating the field from the coil in the 'differential-integral' method described in chapter 3.

Axial flux density distribution $B_m(z)$ due to the magnetisation of the iron:

In the course of the differential finite element method program, the axial and radial components of the magnetic flux density B_z and B_r respectively are calculated at each quadrilateral of the magnetic material. The corresponding components of the magnetisation $\overset{*}{M}_z$ and $\overset{*}{M}_r$ can readily be calculated (cf. equation 1.27) as,

$$\overset{*}{M}_z = \frac{B_z}{\mu_0}\left(1 - \frac{1}{\mu_r}\right)$$

$$\overset{*}{M}_r = \frac{B_r}{\mu_0}\left(1 - \frac{1}{\mu_r}\right) \qquad (1.37)$$

These values are equivalent to $\overset{*}{M}_x$ and $\overset{*}{M}_y$ calculated in the integral finite element method. The flux density at any point due to magnetisation is calculated as the contribution of the $\overset{*}{M}_z$ and $\overset{*}{M}_r$ values at each iron element. The axial flux density $B_m(z)_i$ from the i^{th} magnetic element, at point P, is calculated as a contribution of $B_{mz}(z)_i$, due to the axial magnetisation $(\overset{*}{M}_z)_i$, and $B_{mr}(z)_i$, due to the radial magnetisation $(\overset{*}{M}_r)_i$, hence,

$$\left[B_m(z)\right]_i = \left[B_{mz}(z)\right]_i + \left[B_{mr}(z)\right]_i \qquad (1.38)$$

where $\left[B_{mz}(z)\right]_i$, (see Pugh and Pugh, 1970), can be worked out from the field of a uniformly magnetised cylinder as,

$$\left[B_{mz}(z)\right]_i = \frac{(\overset{*}{M}_z)_i}{2}\left[(\cos\beta_0 - \cos\beta_1) - (\cos\alpha_0 - \cos\alpha_1)\right] \qquad (1.39)$$

and,

$$\left[B_{mr}(z)\right]_i = \frac{(\overset{*}{M}_r)_i}{2}\left[(\sin\alpha_0 - \sin\alpha_1) - (\sin\beta_0 - \sin\beta_1)\right] \qquad (1.40)$$

where the angles α_0, α_1, β_0 and β_1 are shown in Figure 1.17. This figure represents a magnetic element of quadrilateral cross-section abcd. The total axial flux density from the magnetic material is given by,

$$B_m(z) = \sum_i \left[B_m(z)\right]_i \qquad (1.41)$$

Equation 1.41 is also used in Chapter 3 in the calculation of the axial field due to the iron.

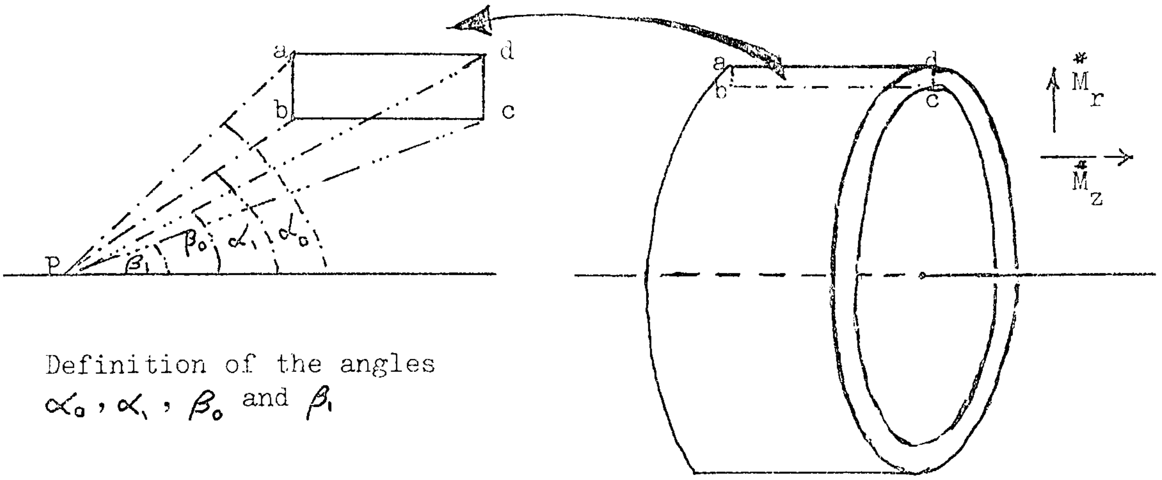

Definition of the angles α_0 , α_1 , β_0 and β_1

Magnetic element of magnetisation components $\overset{*}{M}_z$ and $\overset{*}{M}_r$.

Figure 1.17: A general magnetic element of quadrilateral cross-section abcd with magnetisation components $\overset{*}{M}_z$ and $\overset{*}{M}_r$. Definition of the angles α_0, α_1 , β_0 and β_1 . P is the point at which the flux density is calculated.

1.6 Comparison of the differential and the integral finite element methods:

Table 1.1 shows in tabular form the chief characteristics of each method. An inspection of table 1.1 shows:

The integral method is favourable for iron-free magnetic lenses and lenses of open structure such as single-polepiece lenses. This is because only the iron is divided into finite elements and since it avoids the finite boundary.

For conventional lenses, where a small part of free space is used outside the iron, the differential method is favourable because it needs smaller core (sparse matrix). The finite boundary with $A=0$ around the lens is physically acceptable as discussed earlier.

The integral method provides an exact distribution due to the currents in the coil windings.

Both the differential and the integral finite element methods provide the magnetisation values in iron elements.

It should be noted, however, that a critical and objective comparison between the differential and integral finite element methods has not been published in the literature.

The differential finite element method can be combined with some of the advantageous feature of the integral finite element method in a new method which may be called the '<u>differential-integral</u>' finite element method. In this method, the magnetisation in the iron circuit is found by the differential finite element method. The field distribution due to the coil and the magnetisation can then be calculated using integral formulae with a view to removing some of the boundary errors mentioned previously. This 'differential - integral' finite element method is presented in more detail in chapter 3.

Table 1.1: Comparison of the differential and integral finite element methods.

Characteristic	Differential	Integral
Need for outer boundary	Yes	No
Input to problem	Geometry of coil and iron. Magnetic properties of iron. Arbitrary boundary.	Geometry of coil and iron. Magnetic properties of iron.
Division into finite elements	Iron, coil and free space.	In principle, only the iron.
Variables	vector potentials	The field strength $\overset{*}{H}_r$ and $\overset{*}{H}_z$ components in the iron elements.
Assumption over each element	Vector potential varies linearly.	Constant magnetisation components $\overset{*}{M}_r$ and $\overset{*}{M}_z$.
Number of equations	Equals the number of inner nodes of the finite element grid.	Equals twice the number of iron elements.
Matrix of coefficients	Sparse, since the equation at each node is expressed in terms of the vector potential at the node and the eight vector potential values at the other corners of the triangles in contact with the node.	Dense, since each equation is expressed in terms of $\overset{*}{H}_r$ and $\overset{*}{H}_z$ in all the iron elements.
Field components in iron circuit	B_r and B_z are calculated from vector potentials at the nodes.	$\overset{*}{H}_r$ and $\overset{*}{H}_z$ result from solving the equations.
Magnitisation components	Calculated from the field components B_r and B_z.	Calculated from the field components $\overset{*}{H}_r$ and $\overset{*}{H}_z$.
Axial field distribution	Calculated directly from the vector potential values near the axis.	Calculated as a contribution $B_c^{(z)}$ from the coil windings and $B_m^{(z)}$ due to the magnetisation in iron elements.

In chapter 4, a set of computer programs are presented for the calculation of aberrations in magnetic lenses. The third order aberration coefficients to be found in Glaser (1952 and 1954) have been adopted. The programs can be applied to both objective and projector magnetic lenses. Furthermore the combined aberrations of two magnetic projector lenses can be calculated directly. The programs can be extended to deal with systems of more than two lenses if necessary.

In chapter 5, an account of the use of mini-computers in electron optics is to be given.

The aim of the present investigation therefore is to re-formulate the differential finite element method so as to incorporate boundary conditions that are both mathematically correct and clearly interpretable physically. In addition it was hoped that a comparison of the differential and integral finite element methods could make it possible to asses the accuracy of the calculated axial field distribution. It was also hoped that a suitable combination of both methods could be found that would lead to an appreciable increase in accuracy of the calculated axial field distributions, for a given computing effort.

As this necessarily entails a considerable amount of re-programming, the opportunity was taken, in re-writing the program, to bear in mind the possibilities that now exist, in the form of dedicated mini-computers, for computer aided design. Such computers do not have as large a store as a main frame computer but provide a convenient and rapid way of designing complex lens systems.

It is also clearly desirable to have a set of ray tracing programs that are relevant to present day electron optical calculations. The development of a set of such programs was also one of the objects of the present investigation.

CHAPTER 2

IMPROVED DIFFERENTIAL FINITE ELEMENT PROGRAM FOR THE CALCULATION OF MAGNETIC FIELDS

The original vector potential program of Munro (1971), was organised in a way that did not permit one to insert known values of the vector potential A at an arbitrary boundary. It was therefore necessary to re-write and re-arrange this program in order to make this option available. The improved program (Mulvey and Nasr, 1980b and 1981.cf. Appendices 9 and 10), was simplified to make it available on personal minicomputers. The program was re-written in BASIC and in FORTRAN, starting from the solution of Poisson's Equation 1.1. The first part of the improved program gives similar results to those of Munro's program, and so can be used for conventional magnetic electron lenses when adequate computing power is available. For single-polepiece lenses or when the limit of computer memory is reached before the size of finite elements is adequately small over the given area, an improvement was needed so as to overcome this obstacle as explained below. The new program can deal with magnetic electron lenses under linear conditions (where the magnetic material has constant permeability), and under non-linear conditions (where the magnetic material has a permeability that varies with the flux density).

2.1 Improved vector potential program for magnetic structures under linear condition (VPLIN):

The improved vector potential program under linear condition (VPLIN), is based on the minimisation of the energy functional 1.9 with the magnetic material characterised by equation 1.11. As a consequence of this minimisation, a set of linear equations at each node of the finite element mesh is generated. (The nodal equations are derived in detail in Appendix 3). The boundary conditions are then inserted and the equations are solved by Gaussian elimination; a subroutine for this solution is given in Appendix 4. A block-diagram for the program VPLIN is shown in Figure 2.1.

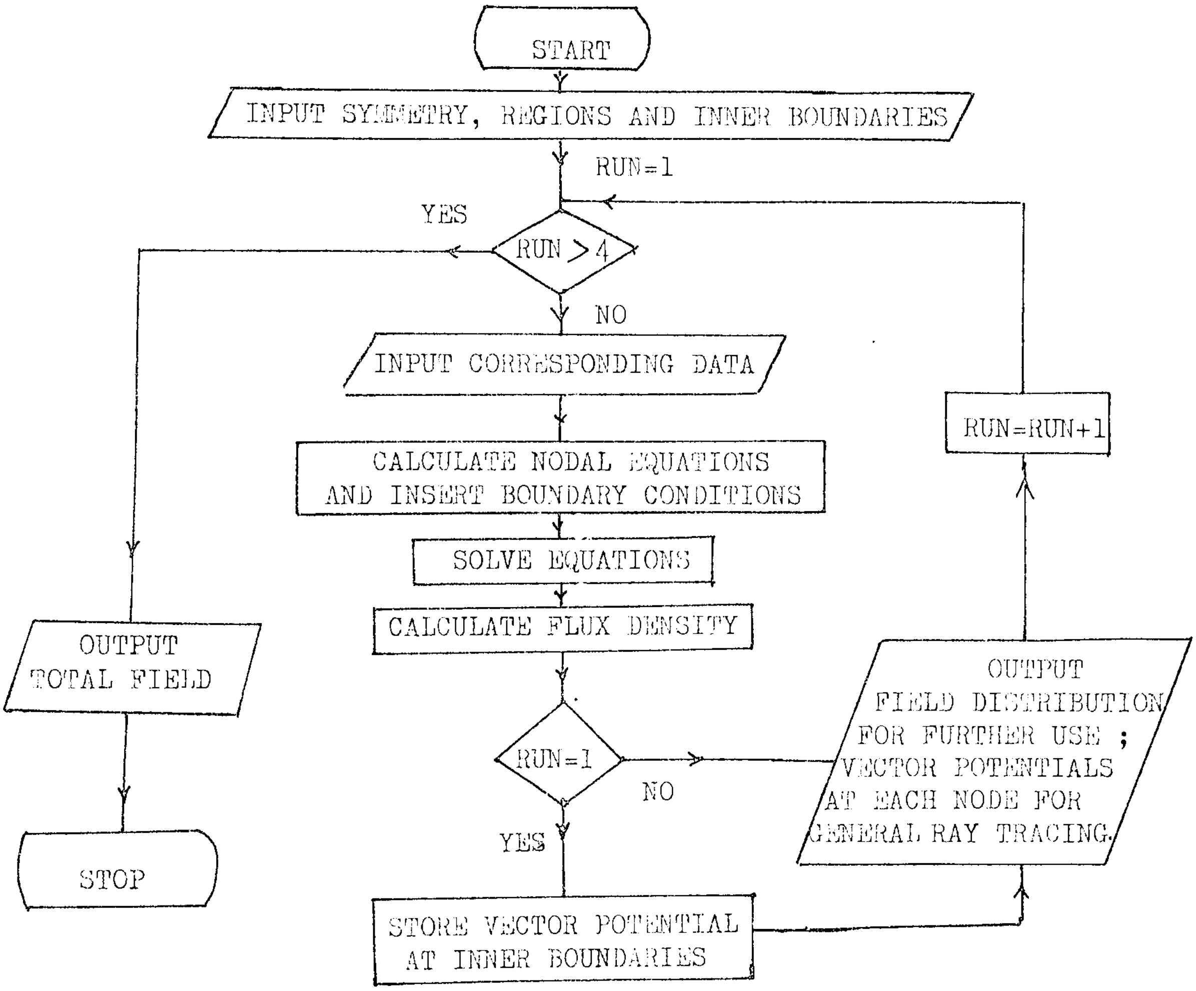

Figure 2.1: Block-diagram for the improved vector potential program (VPLIN) under linear condition.

The method of applying the VPLIN program is as follows:

2.1.1 Specifying the boundaries, major mesh lines and regions of the structure:

Figure 2.2 shows an experimental single-polepiece magnetic electron lens (Christofides, 1980) which was designed in connection with the production of X-ray sources. The boundary CDEF for the finite element method is established as shown in Figure 2.2. The lefthand side, the righthand side , the upper and lower boundaries are CD, EF, CF and DE respectively. The position of the three boundaries CD, EF and CF are estimated on the light of the vector potential distribution of the iron free coil. For open structures, a boundary at a distance of five times the mean diameter of the coil may be adequate for accuracies better than 2 % . However the presence of magnetic materials may have the effect of reducing this distance and better accuracies may be achieved.

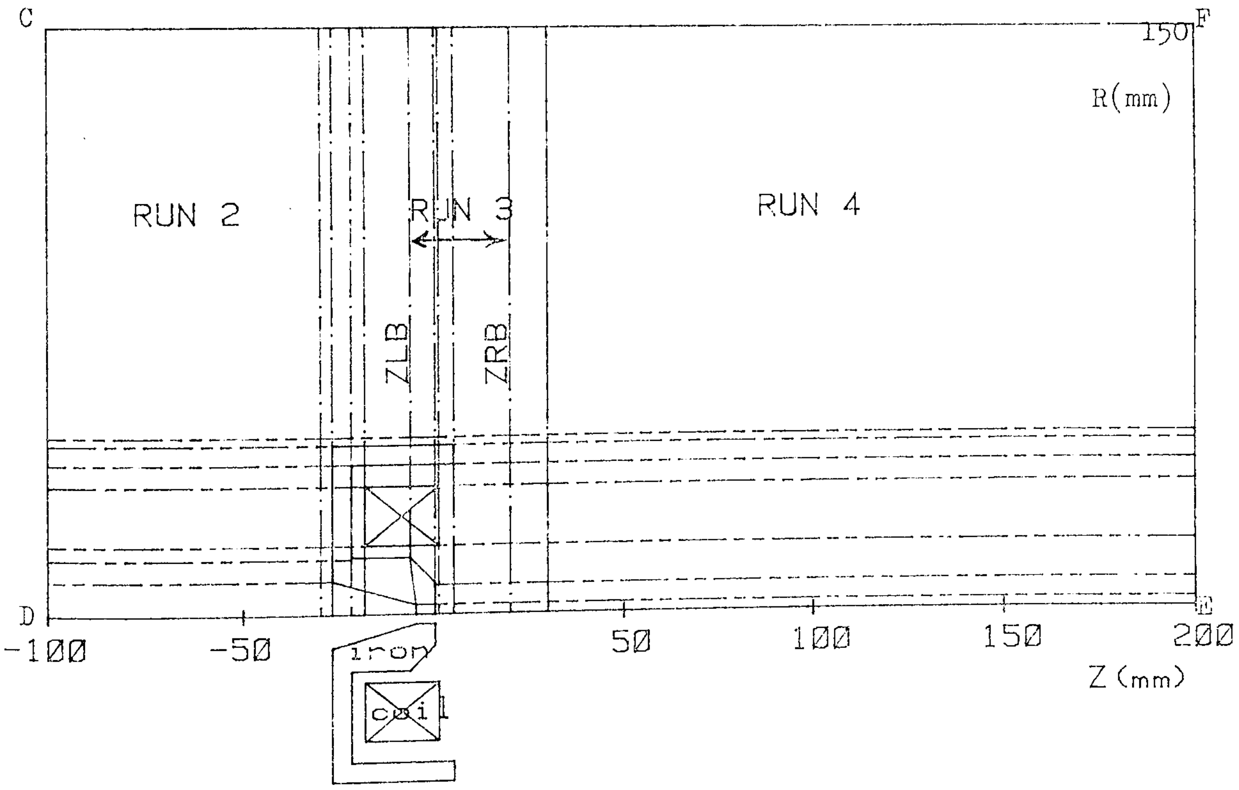

Figure 2.2: An experimental single-polepiece lens as part of the magnetic structure. Specifying the boundaries for the finite element method, major mesh lines and regions of the structure.

The structure, including the magnetic material, coil and the free space within the finite boundary, is divided into a grid of quadrilaterals; the lines that define the geometry of the structure or the lines that are needed to change the size of the meshes are called major mesh lines. Each quadrilateral is subsequently divided into two triangles as finite elements. Two inner boundaries ZLB and ZRB are selected remote from the boundaries CD and EF and where a comparatively fine mesh size can be attained. The whole structure is used in the first calculation (RUN 1), as is shown in Figure 2.3a where the structure within the finite boundary is shown. The two inner boundaries ZLB and ZRB divide the structure into three regions marked RUN 2, RUN 3 and RUN 4. When solving for RUN 1, the vector potential values along the boundaries ZLB and ZRB are saved for use in subsequent runs. The vector potential values at the boundary CDEF are set to zero for RUN 1.

RUN 2, Figure 2.3b, has the boundaries CD, DE and CF with the vector potential values along them are set to zero; the righthand side boundary is ZLB with the vector potential values that were saved in RUN 1. RUN 3, Figure 2.3c, has the boundaries CF and DE with vector potential values that are set to zero. ZLB and ZRB are the lefthand side and the righthand side boundaries respectively with the vector potential values that were saved from RUN 1. Finally RUN 4, Figure 2.3d, has the boundaries CF, DE and EF with vector potential values equal zero; ZRB is the lefthand side boundary with the vector potential values that were saved in RUN 1. The three runs RUN 2, RUN 3 and RUN 4 yield the final distribution of the vector potential throughout the magnetic lens.

2.1.2 Preparation of data for the VPLIN program:

The data for the VPLIN program is organised as follows; an example of the data preparation is shown in Figure 2.4.

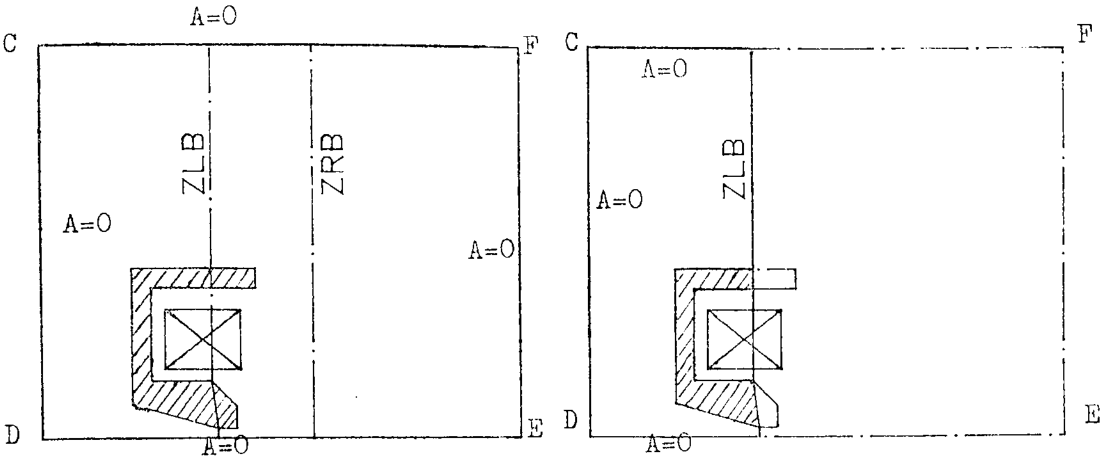

2.3a: RUN 1
A=0 on the boundary CDEF. A values at ZLB and ZRB after RUN 1, are saved to be used for susequent runs.

2.3b: RUN 2
A=0 on CD, DE and CF. The right handside boundary is ZLB with A values that are saved from RUN 1.

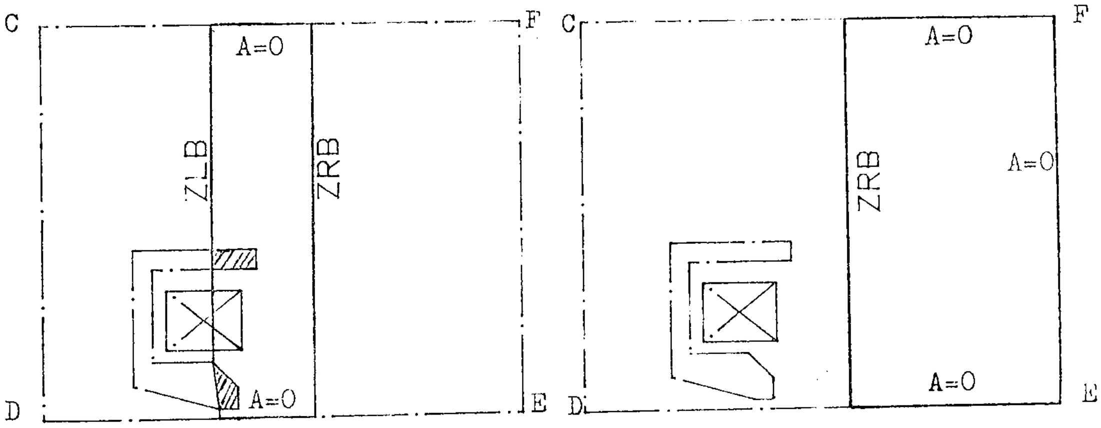

2.3c: RUN 3
A=0 on CF and DE. The left handside boundary is ZLB and the right handside boundary is ZRB with A values that are saved from RUN 1.

2.3d: RUN 4
A=0 on CF, DE and EF. The left handside boundary is ZRB with A values that are saved from RUN 1.

Figure 2.3: Specifying the boundaries for the different runs to be used by the VPLIN program.

1.a) symmetry condition for the structure; 1 for symmetrical structure and 0 for asymmetrical structures.

1.b) runs to be performed. 1.c) the two inner boundaries ZLB and ZRB.

2.a) title. 2.b) output of flux density and flux values, 0=no, 1=yes.

2.c) the axial coordinates of the nodes of the major mesh lines, RUN 1.

2.d) the radial coordinates of the nodes of the major mesh lines, RUN 1.

2.e) magnetic circuit specifications, RUN 1.

2.f) electric current coils specifications, RUN 1.

3) corresponding data for other runs prepared as in 2.a to 2.f above.

```
1.a      0
1.b      1    2    3    4

1.c     24   40

2.a  RUN 1: 29X59 MESH  Z=-100MM TO 200MM
2.b      0    0

             1    6    8   12   14   24   27   29   32   40   50   59
         1-100. -30. -27. -22.-18.5 -6.5   0.   1.   5.  10.  20. 200.
2.c      5-100. -30. -27. -22.-18.5 -6.5   0.   1.   5.  10.  20. 200.
         ...
        29-100. -30. -27. -22.-18.5  -5.   0.   1.   5.  10.  20. 200.

             1    6    8   12   14   24   27   29   32   40   50   59
         1 150. 150. 150. 150. 150. 150. 150. 150. 150. 150. 150. 150.
2.d      5  45.  45.  45.  45.  45.  45.  45.  45.  45.  45.  45.  45.
         ...
        29   0.   0.   0.   0.   0.   0.   0.   0.   0.   0.   0.   0.

         8   32    7   10      2500.
2.e      8   12   10   19      2500.
         8   27   19   23      2500.

2.f     14   29   12   17   504.275

3    RUN 2: 29X48 MESH  Z=-100MM TO -5MM
         0    0

             1   12   16   24   28   48
         1-100. -30. -27. -22.-18.5 -6.5
         ...
         ...
```

Figure 2.4: Preparation of data for the VPLIN program for the single-polepiece lens of Figure 2.2.

2.1.3 Application of the improved VPLIN program to the calculation of magnetic field distribution of a single-polepiece lens.

The VPLIN program was applied to the calculation of magnetic fields for a single-polepiece lens (Mulvey and Nasr, 1980b, 1981). Another example on the application of the VPLIN program to the calculation of the magnetic field distribution of a single-polepiece lens is given for the lens in Figure 2.2.

The computed axial flux density values from RUN 1 are shown in Figure 2.5; the crosses indicate the computed values and the solid line is a cubic spline fit to the computed points. The computed axial flux density values are plotted for the region between $-5\text{mm} \leqslant z \leqslant 100\text{mm}$ since the values outside this range are very small. The results of RUN 2 for the region $z \leqslant -5\text{mm}$ are also very small and are therefore not shown. The improved axial flux density distribution for RUN 3 is shown in Figure 2.6, for the region between $-5\text{mm} \leqslant z \leqslant 20\text{mm}$. The improved axial flux density distribution for RUN 4, is shown in Figure 2.7 for the region $z > 20\text{mm}$. The total axial field distribution for the single-polepiece lens of Figure 2.2 is the sum of the above distributions and is shown in Figure 2.8 with improved accuracy and smoothness.

2.1.4 Test of accuracy of the VPLIN program using Hall probe experimental measurements.

The axial flux density distribution of the single-polepiece lens of Figure 2.2 was measured experimentally with an excitation of 1475 A-t. The measurement was carried out using a BELL Model 120 Hall probe Gaussmeter. The measured values are indicated by the crosses in Figure 2.9, where the results of the improved VPLIN are shown as a solid line

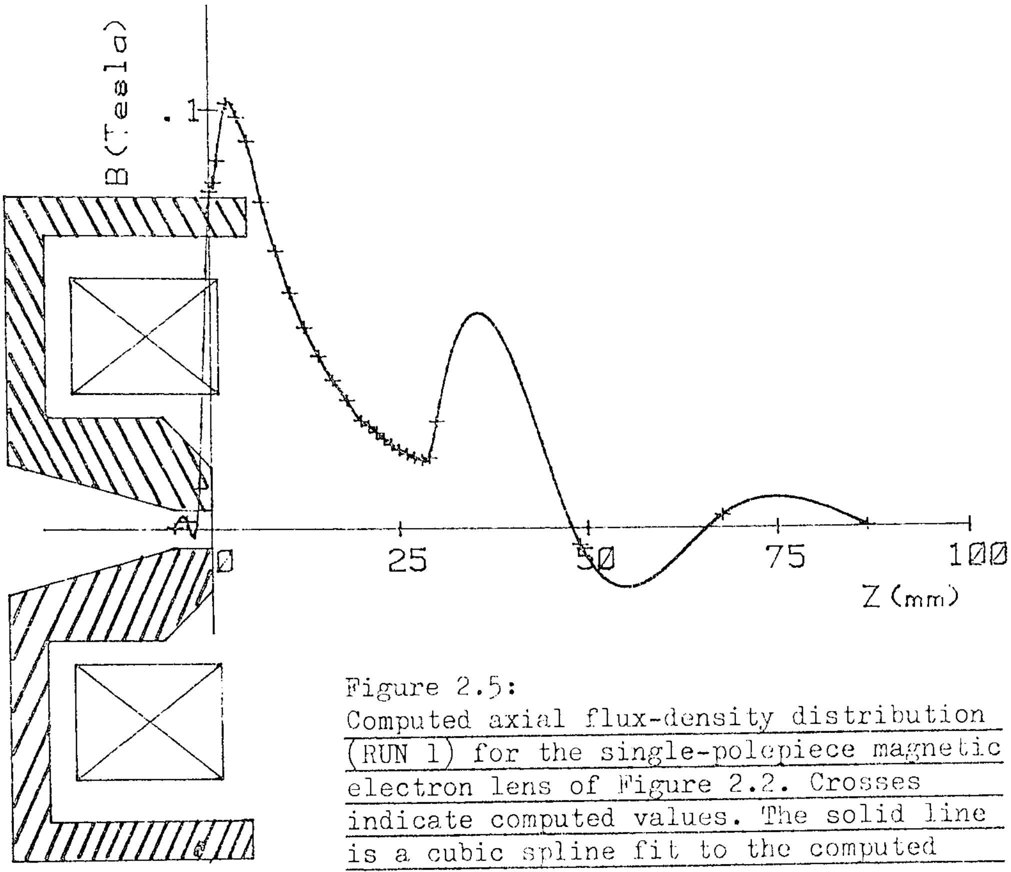

Figure 2.5:
Computed axial flux-density distribution (RUN 1) for the single-polepiece magnetic electron lens of Figure 2.2. Crosses indicate computed values. The solid line is a cubic spline fit to the computed points. Excitation 1475 A turns.

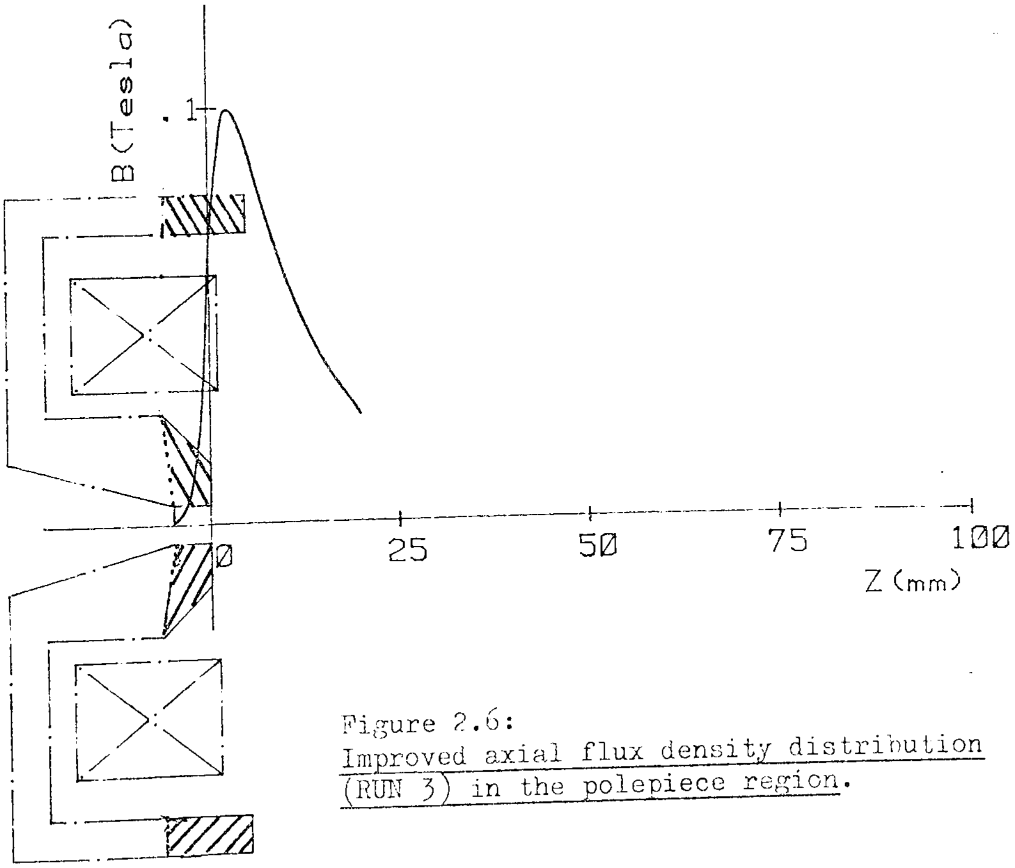

Figure 2.6:
Improved axial flux density distribution (RUN 3) in the polepiece region.

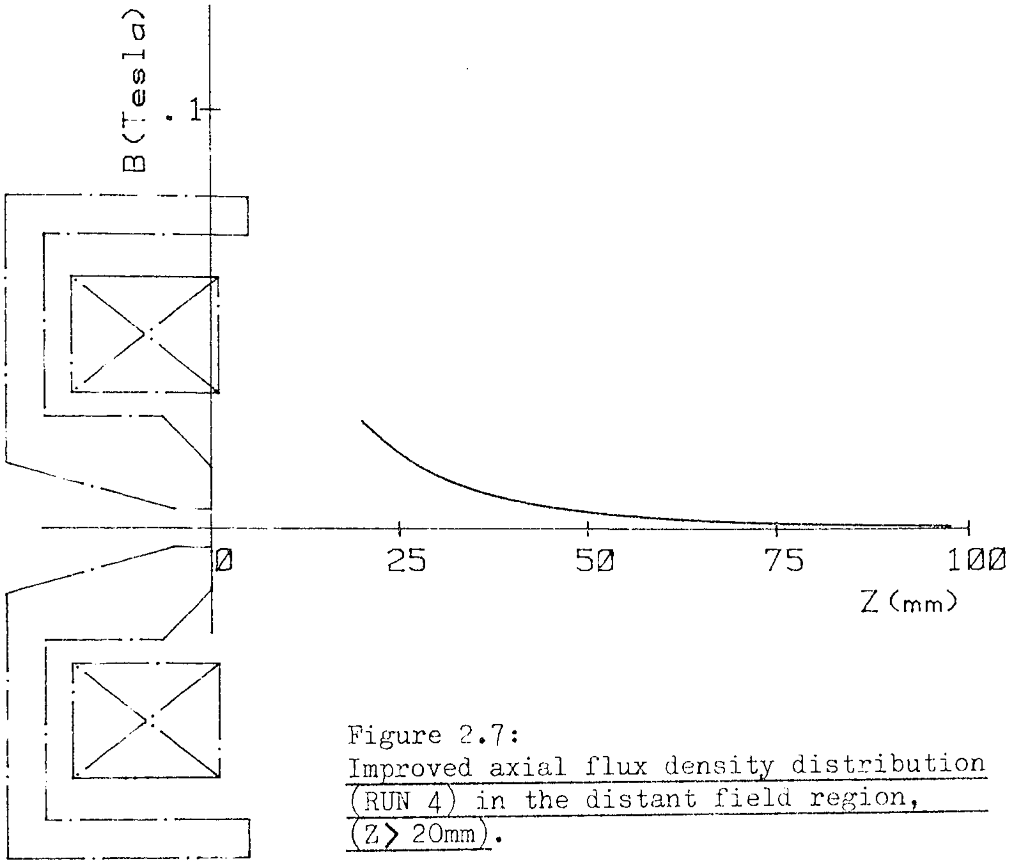

Figure 2.7:
Improved axial flux density distribution (RUN 4) in the distant field region, (Z > 20mm).

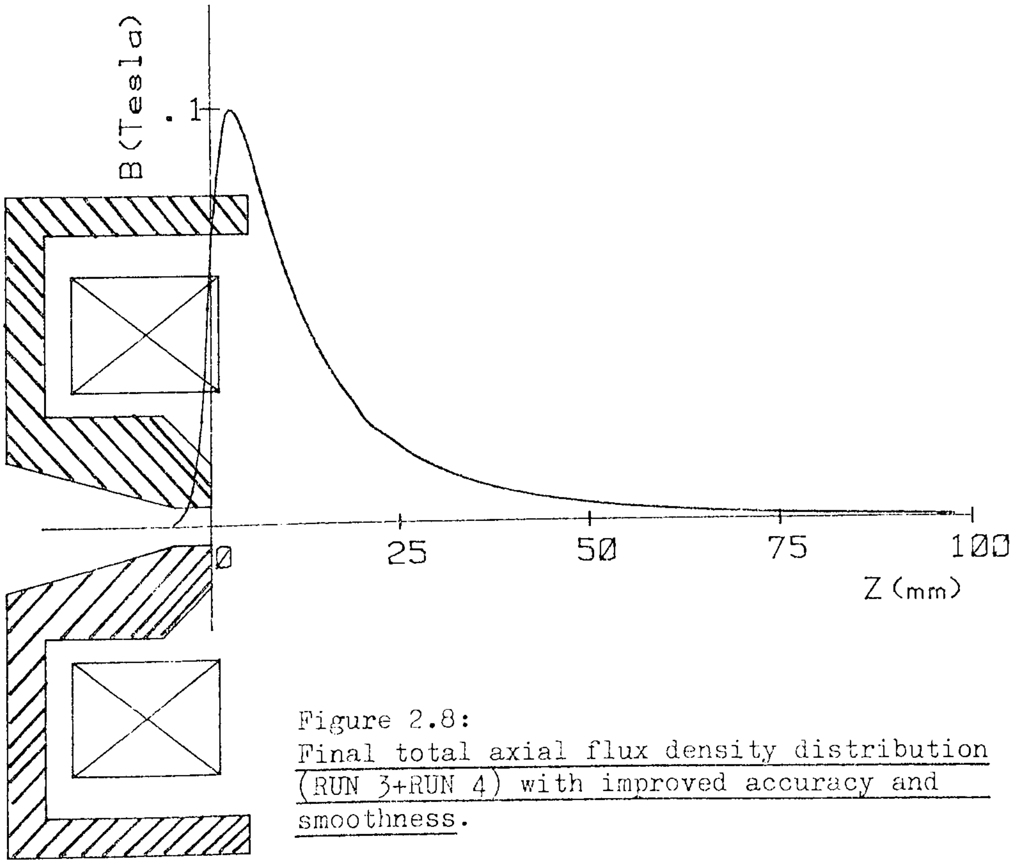

Figure 2.8:
Final total axial flux density distribution (RUN 3+RUN 4) with improved accuracy and smoothness.

for comparison purposes. The agreement between the calculated and the measured values is within the experimental accuracy of 3 % .

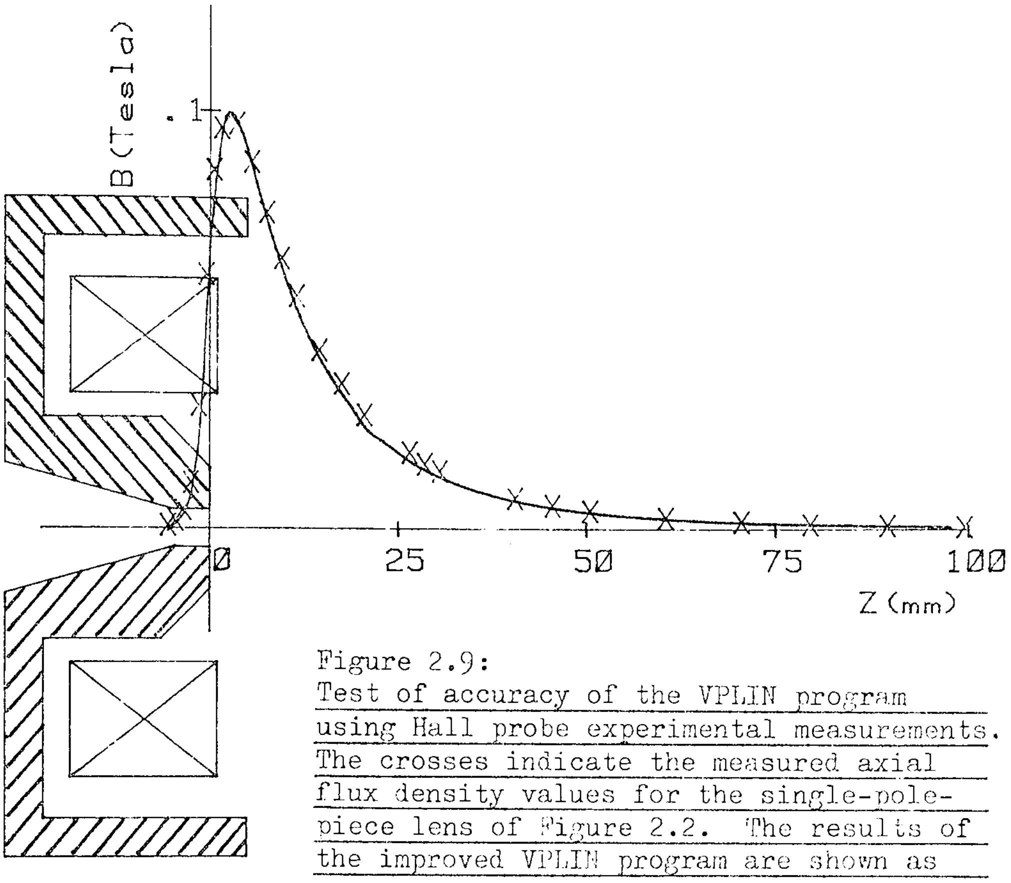

Figure 2.9:
Test of accuracy of the VPLIN program using Hall probe experimental measurements. The crosses indicate the measured axial flux density values for the single-pole-piece lens of Figure 2.2. The results of the improved VPLIN program are shown as a solid line.

2.2 Improved vector potential program for magnetic structures under non-linear condition (VPSAT):

The improved vector potential program under non-linear condition (VPSAT), is based on the minimisation of the energy functional 1.9 with the magnetic material characterised by equation 1.10. As a consequence of this minimisation, a set of non-linear equations at each node of the finite element mesh is generated. (The nodal equations are derived in Appendix 5). The boundary conditions are inserted and the equations are solved by the Newton-Raphson iteration method (Appendix 6). A block diagram for the VPSAT program is shown in Figure 2.10.

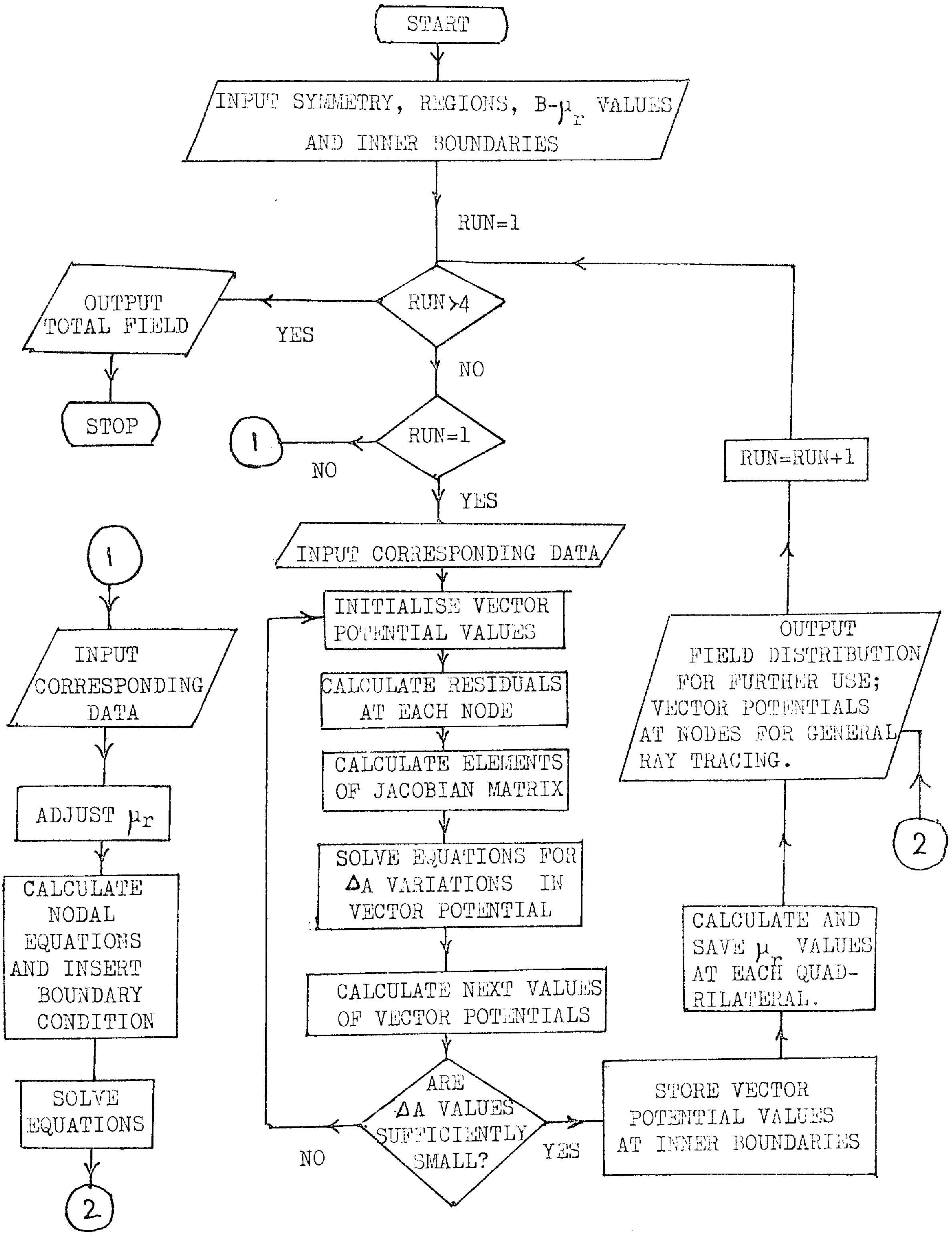

Figure 2.10: Block-diagram for the improved vector potential program (VPSAT) under non-linear condition.

2.2.1 Specifying the boundaries, major mesh lines and regions of the structure:

The boundaries, major mesh lines and the regions of the structure for the VPSAT program are specified as in section 2.1.1.

2.2.2 Preparation of data for the VPSAT program:

The data for the geometry of the structure are prepared for the VPSAT program in the same way as the VPLIN program. But for the VPSAT program a table of the relative permeability μ_r as a function of the magnetic flux density B is introduced to perform the iteration process. A typical relation between μ_r and B for a magnetic material is shown in table 2.1 and the relation is plotted in Figure 2.11. The number of regions to be analysed are chosen as for the VPLIN program, but the region including the coil is excluded from the final runs.

Table 2.1 A typical relation between the relative permeability μ_r and flux density B of a magnetic material.

B (Tesla)	μ_r
0.000	6366.2
0.400	6366.2
0.680	5411.3
0.880	4668.5
1.020	4058.0
1.224	2831.4
1.325	1735.0
1.351	1033.6
1.377	815.3
1.442	521.9
1.500	253.1
1.589	142.4
1.623	116.1
1.679	85.6
1.840	33.2
1.898	19.5
2.000	10.1
2.300	4.6
2.900	2.6
3.100	2.4

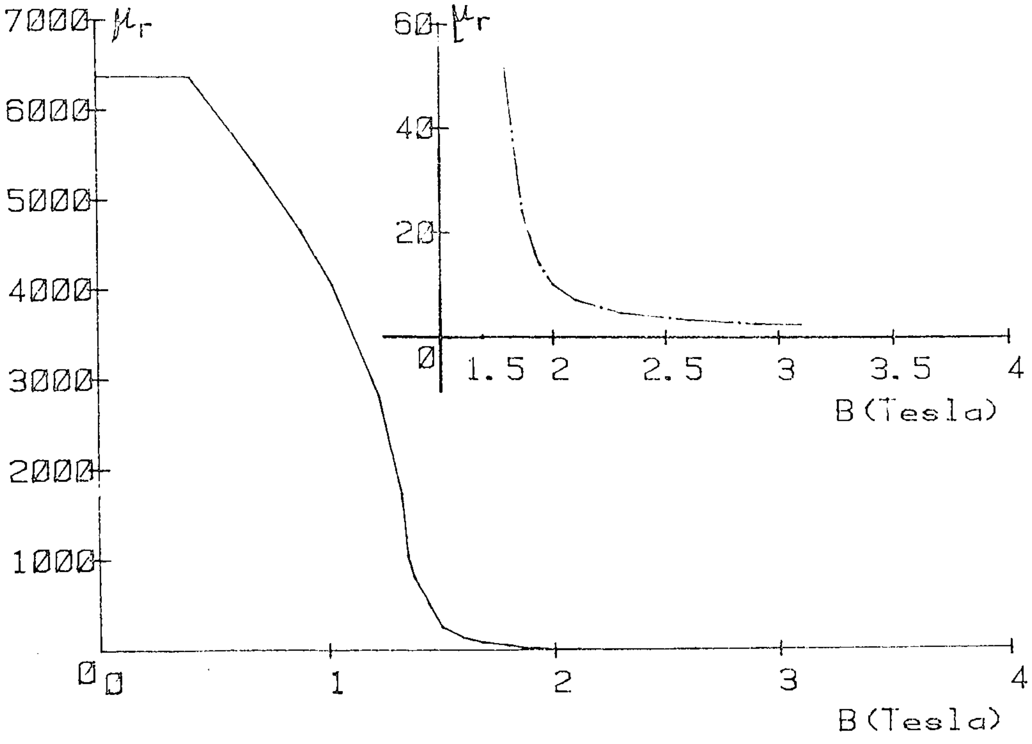

Figure 2.11: Relation between the relative permeability μ_r of a magnetic material and the flux density B.

2.2.3 Application of the improved VPSAT program to the calculation of magnetic field distribution of a single-polepiece lens under saturation condition:

Figure 2.12 represents a design (Mulvey and Christofides, 1980) for a single-polepiece lens to be used as micro-X-ray source ; it can also be used as the objective for a 200 kV electron microscope. The improved VPSAT program was used to calculate the magnetic field distribution for the above lens under saturation conditions, i.e. when a linear variation in the applied ampere turns does not produce a corresponding linear variation in the flux density. The lens was driven to saturation conditions by applying an excitation of 10800 A-turns. The axial field distribution of RUN 1, is indicated by the crosses in Figure 2.13; the solid line is a cubic spline fit for the computed values. The final result of the VPSAT is shown in Figure 2.14 with improved accuracy and smoothness. The agreement between the calculated ampereturns and those actually applied was better than 2 % .

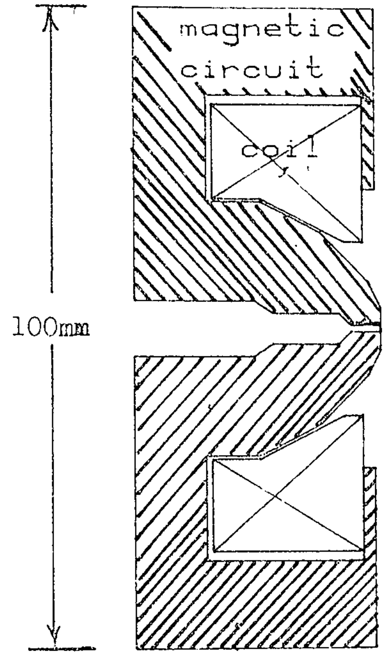

Figure 2.12 A single-polepiece magnetic electron lens under saturation condition. Lens excitation 10800 A turns.

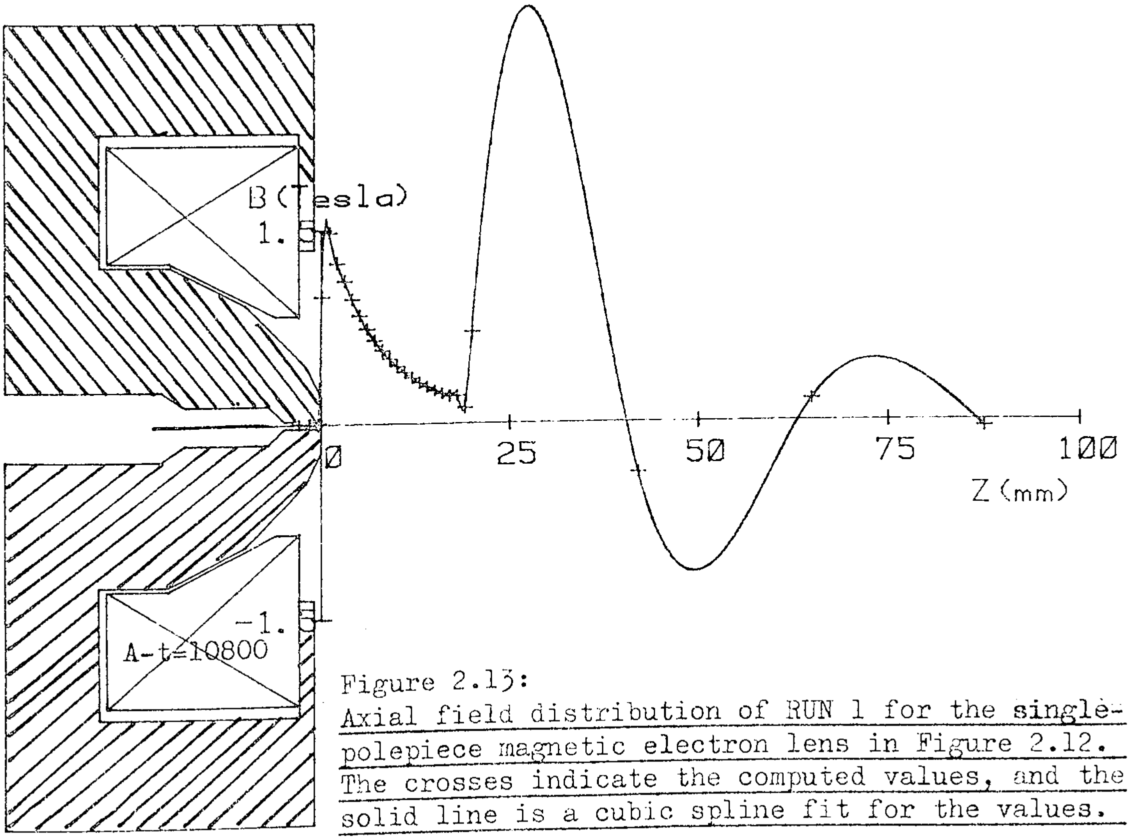

Figure 2.13:
Axial field distribution of RUN 1 for the single-polepiece magnetic electron lens in Figure 2.12. The crosses indicate the computed values, and the solid line is a cubic spline fit for the values.

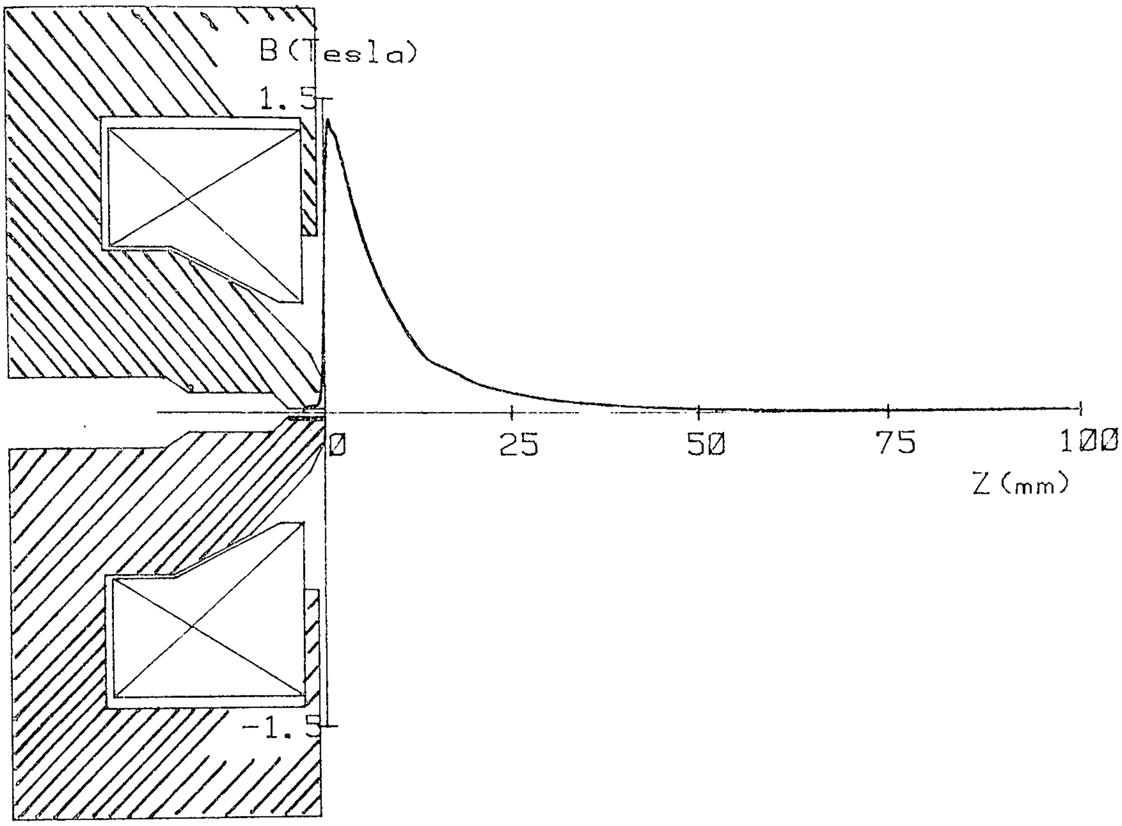

Figure 2.14 Final axial field distribution for the single-polepiece magnetic electron lens of Figure 2.12 using the VPSAT program with improved accuracy and smoothness. The agreement between the calculated ampereturns and those actually applied was better than 2 %. (A-t = 10800)

2.2.4 Test of accuracy of the VPSAT program using Hall probe experimental measurements.

The axial flux density distribution of the single-polepiece magnetic electron lens of Figure 2.12 was measured experimentally under saturation condition with an excitation of 10800 A-turns. The measurement was carried out using a BELL Model 120 Hall probe Gaussmeter. Because of the small bore of the lens, the axial flux density measurement was restricted to the region facing the polepiece and up to 0.9mm from its surface. The measured values are indicated by the crosses in Figure 2.15 and the solid line represents the computed values using the improved VPSAT. Good agreement was obtained between the calculated and the

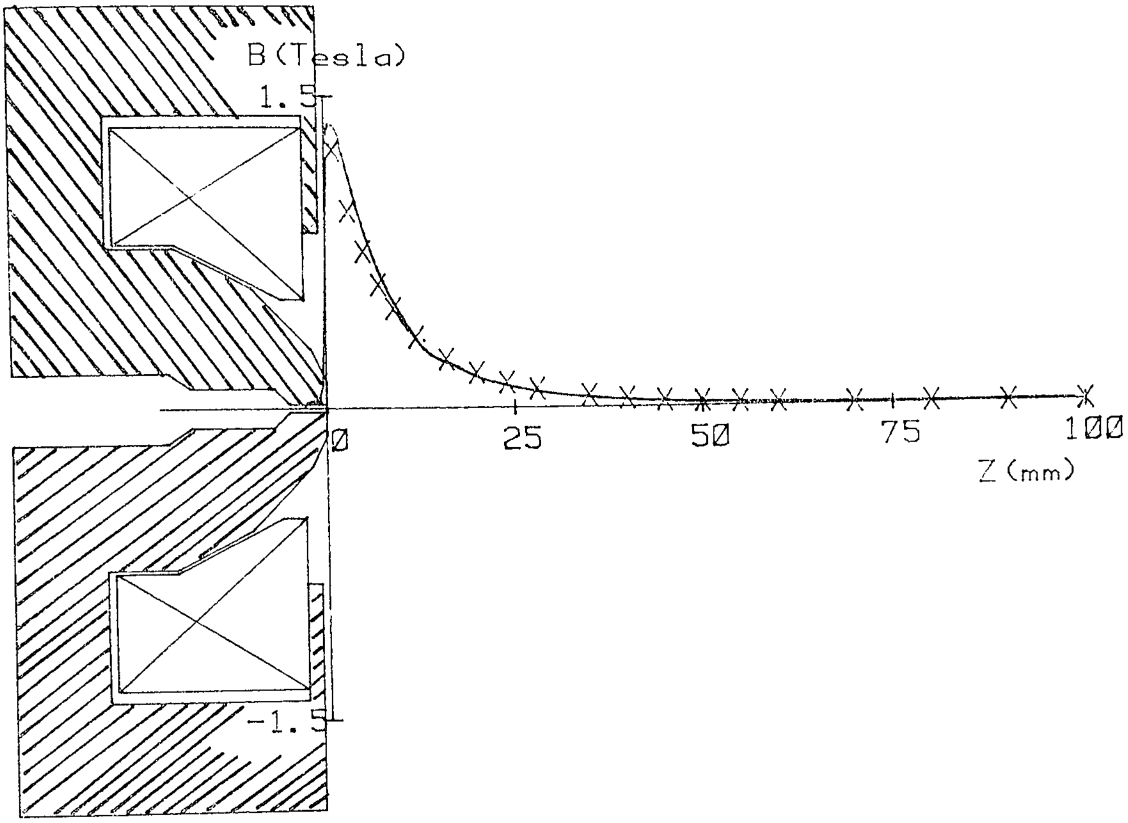

Figure 2.15 Test of accuracy of the improved VPSAT program using Hall probe experimental measurements. The crosses indicate the measured axial flux density values for the single-polepiece magnetic electron lens of Figure 2.12. The solid line is a cubic spline fit for the computed values using the improved VPSAT program. (A-t = 10800)

experimental results except for the region very near to the polepiece where the error may be due to differences between the actual B/H* characteristics of the polepiece material and the data supplied to the computer by the B/μ_r relation. It is also likely that the finite size of the Hall-effect detector caused some error in the region of the peak field where the axial field distribution is changing rapidly with axial position.

CHAPTER 3

THE 'DIFFERENTIAL-INTEGRAL' FINITE ELEMENT METHOD

The accuracy of axial field distribution provided by the differential finite element method can be checked and improved with very little extra computing effort by incorporating some of the advantages of the integral finite element method. A new method is now presented which may be called the 'differential-integral' finite element method (Mulvey and Nasr, 1981. cf. Appendix 10). In this method the magnetic field due to the coil is calculated independently by the Biot-Savart law (cf. chapter 1); use is also made of the magnetisation of the iron, which is already available, to calculate the magnetic field due to the iron. It should be noted that in previous differential programs no use has been made of this valuable information although it is readily available from the computed axial and radial field components in the iron.

Since the magnetic flux density at any point is the sum of that due to the coil B_c and that due to the iron B_m, on the axis in particular we may write,

$$B_z(z) = B_c(z) + B_m(z) \tag{3.1}$$

The contribution $B_c(z)$ from the coil windings can be calculated easily and quickly from the Biot-Savart law as shown in Chapter 1. The field $B_m(z)$ can then be obtained by subtracting $B_c(z)$ which is analytically exact from the total field $B_z(z)$ as calculated in the differential finite element method. The field due to the iron is easier to smooth than is the total field $B_z(z)$. Since the total contribution to the lens excitation from the iron is zero, the area under the $B_m(z)$ curve should also be zero, taking into account the sign of $B_m(z)$. In general the values of $B_m(z)$ near the boundary will be smaller than the correct value. A direct way of determining $B_m(z)$ makes use of the magnetisation values in the iron elements; these values are directly available in the differential finite element method.

The application of the 'differential-integral' finite element method is perhaps best illustrated by a calculation of the field distribution of the lens shown in Figure 3.1. This lens although deceptively simple in structure, is extremely difficult to solve by the differential finite element method because of the open boundaries on all sides of the coil. The field $B_c(z)$ from the coil windings, of this lens, calculated by the Biot-Savart law, is shown by the chain-dotted line in Figure 3.2. The total field $B_z(z)$ as calculated by the improved differential finite element method program VPLIN, is shown as a solid line in Figure 3.2. The excitation calculated from the area under this distribution curve showed a boundary loss in excitation of 4 %. Subtracting $B_c(z)$ from $B_z(z)$ yields the contribution $B_m(z)$ from the iron circuit. The contribution $B_m(z)$ is shown as a broken line in Figure 3.2. The positive part of this distribution was about 5 % smaller in area than the negative part. As a first approximation, the field in the upper part was therefore corrected by this difference and the improved $B_m(z)$ was obtained. The improved $B_z(z)$ was then calculated by adding the improved $B_m(z)$ to $B_c(z)$ as shown by a dotted line in Figure 3.2. This process is used as a check on the accuracy of the calculated axial flux density distribution and provides a means of improving this distribution. However, the $B_m(z)$ distribution was

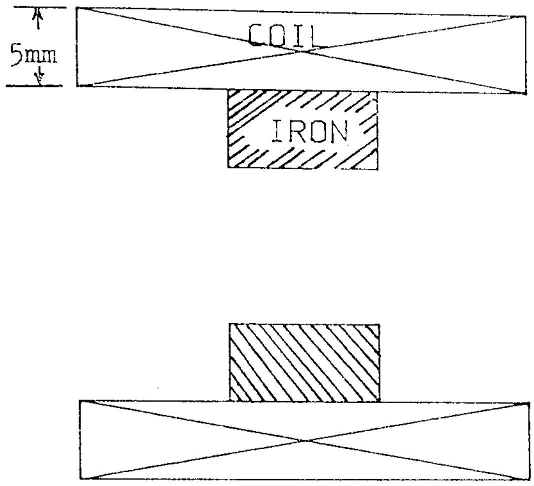

Figure 3.1: A magnetic electron lens for the application of the 'differential-integral' finite element method.

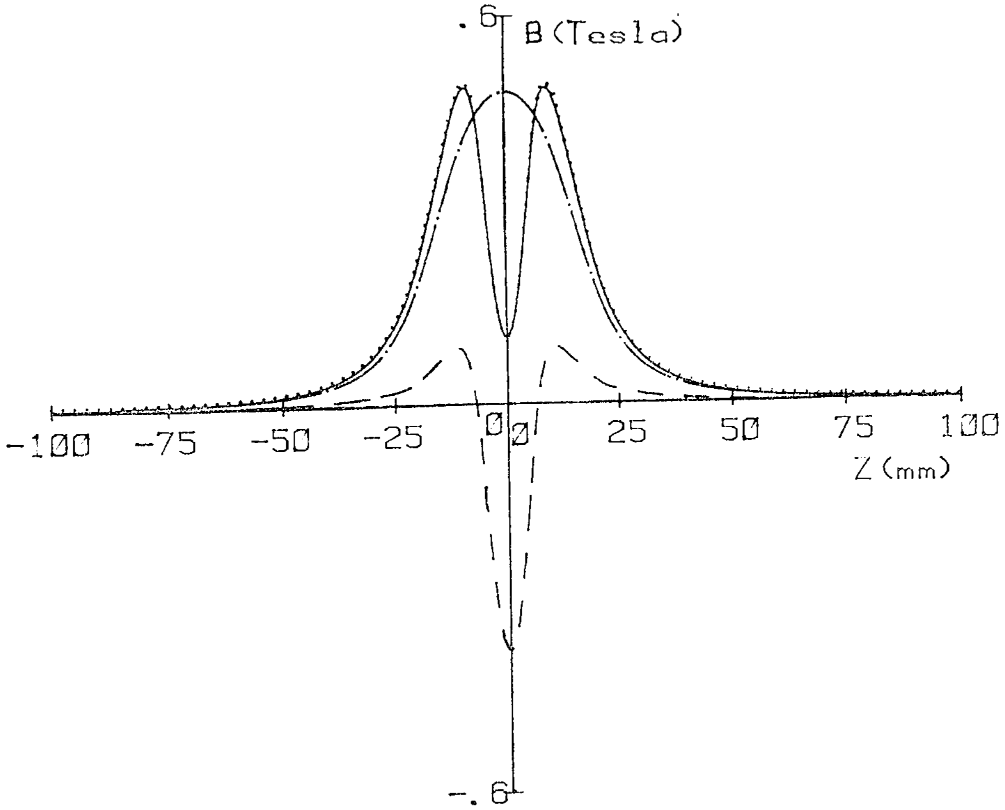

Figure 3.2:
Axial flux density distribution for the lens of Figure 3.1, (a) calculated by the improved differential finite element method program VPLIN (——) using 20X24 mesh points, (b) calculated due to the coil (-.-) by the Biot-Savart law, (c) calculated due to the iron (---) by subtracting b from a, (d) as the final (...) calculated by adding b to the improved distribution of c.

smoothed manually which necessitates familiarity in magnetic field distributions of the particular lens involved in the calculations.

A direct method that does not need such manual smoothing makes use of the magnetisation values of the iron elements. These magnetisation values are directly available in the differential finite element method; this forms the first part of the 'differential-integral' finite element method program (DIFINT). The second part of this program uses a direct method to calculate, at any point, the axial field $B_c(z)$ due to the current in coil windings and $B_m(z)$ due to the magnetisation in iron elements. The total axial field $B_z(z)$ of the magnetic lens is then calculated by adding the field due to the coil to that due to the magnetisation in the iron circuit.

3.1 Application of the DIFINT program to the calculation of magnetic fields:

The VPLIN program is applied to the calculation of the field of the lens of Figure 3.1 for RUN 1 only. The axial flux density due to RUN 1 is shown in Figure 3.3, where the crosses indicate the computed values and the solid line is a cubic spline fit to the computed values. The magnetisation of the iron elements are saved from RUN 1 for use in the integral part of the DIFINT program. A block-diagram of the integral part of the DIFINT program is shown in Figure 3.4. The axial flux density due to the coil is shown in Figure 3.5 and the axial flux density distribution, calculated directly, due to the magnetisation of the magnetic material is shown in Figure 3.6. The final axial flux density distribution from this lens, using the DIFINT program, is shown as a solid line in Figure 3.7; the results of RUN 1 of the VPLIN program are indicated by the crosses for comparison. This distribution shows an improved smoothness and good agreement between the calculated ampere turns and those actually applied.

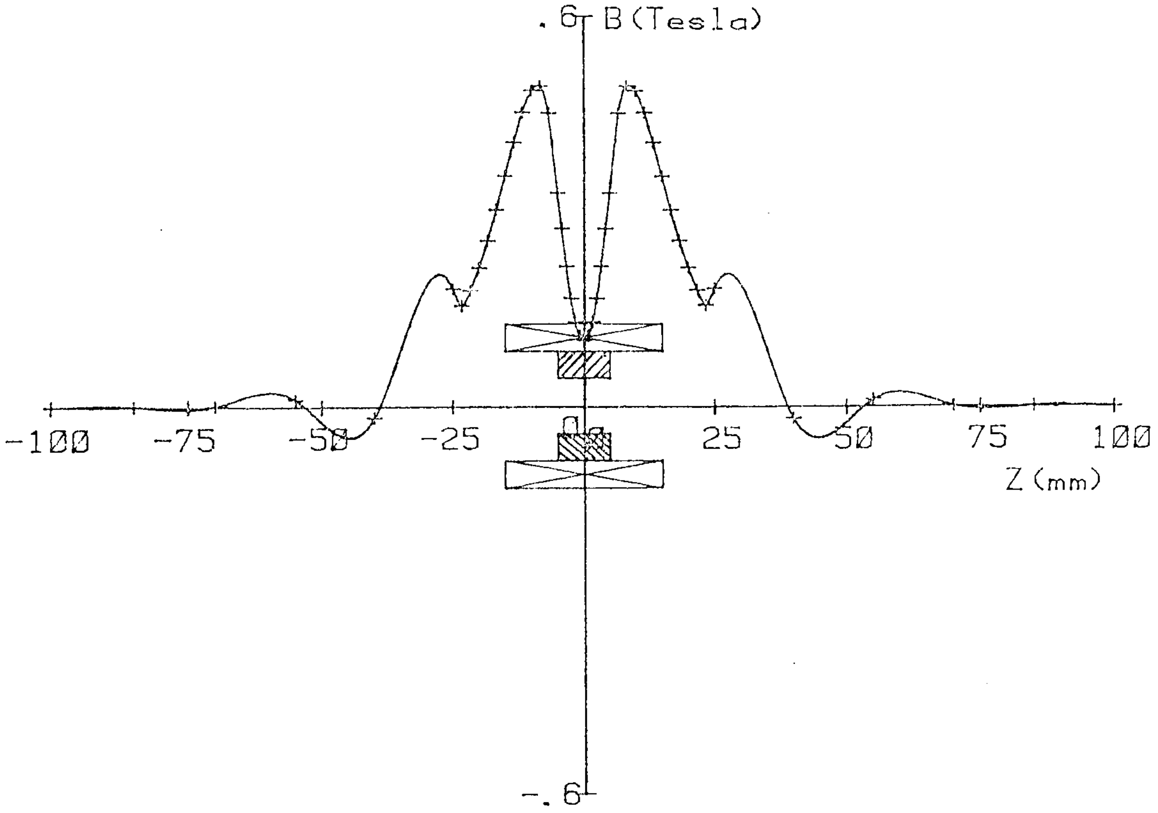

Figure 3.3: Axial flux density distribution for the lens of Figure 3.1, using RUN 1 of VPLIN program. Crosses indicate computed values, (20X24 mesh points), and the solid line is a cubic spline fit to the computed values.

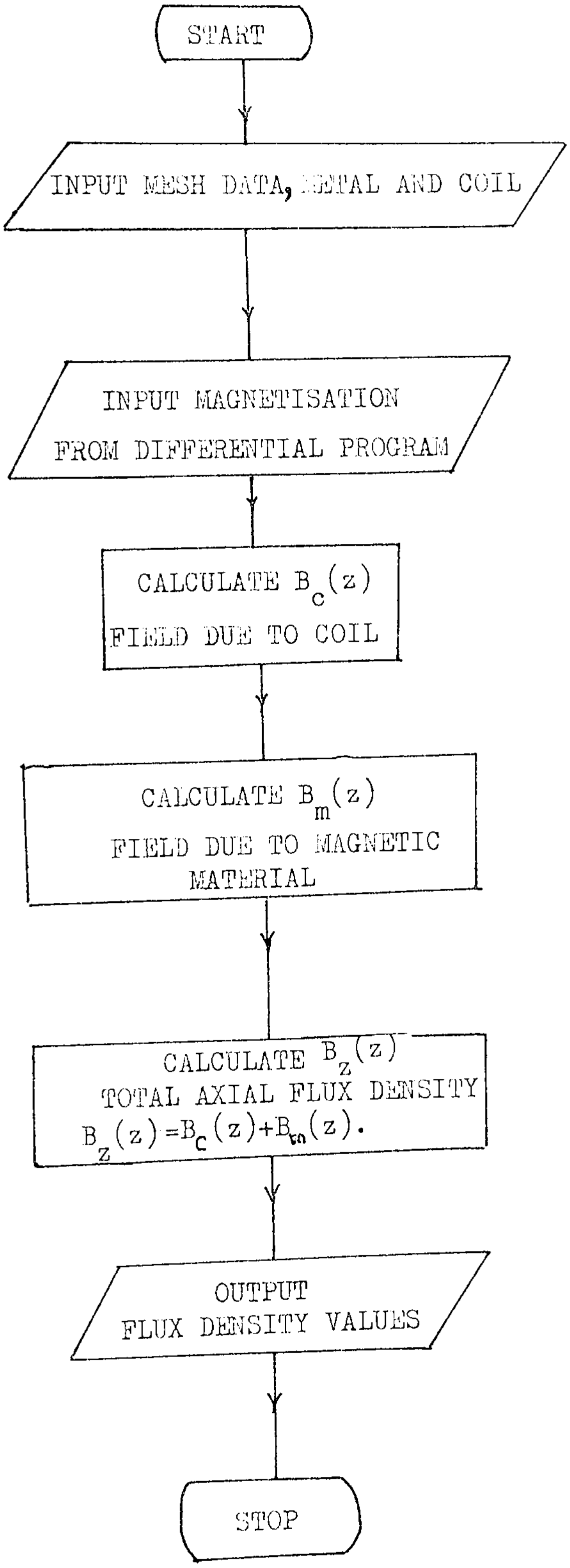

Figure 3.4: A block-diagram of the integral part of the DIFINT program.

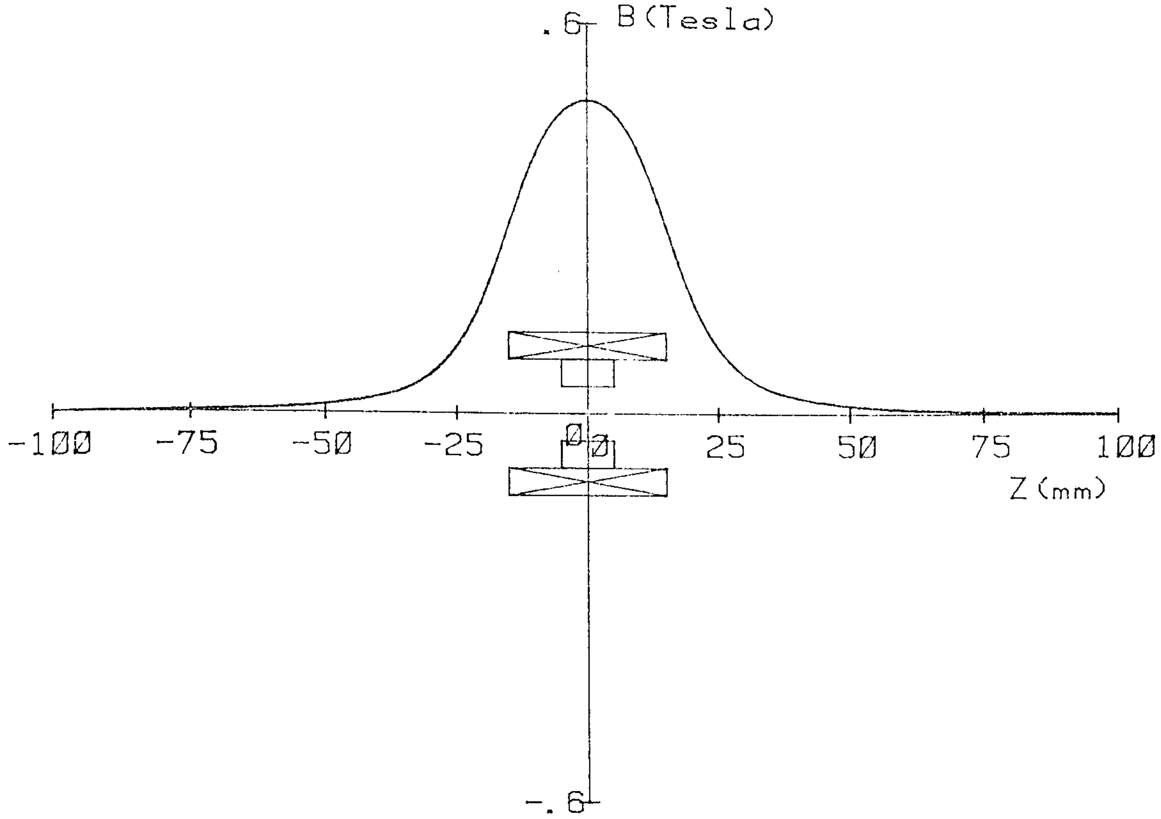

Figure 3.5: Axial flux density distribution $B_c(z)$ due to the current carrying coil of the lens of Figure 3.1. (Biot-Savart law).

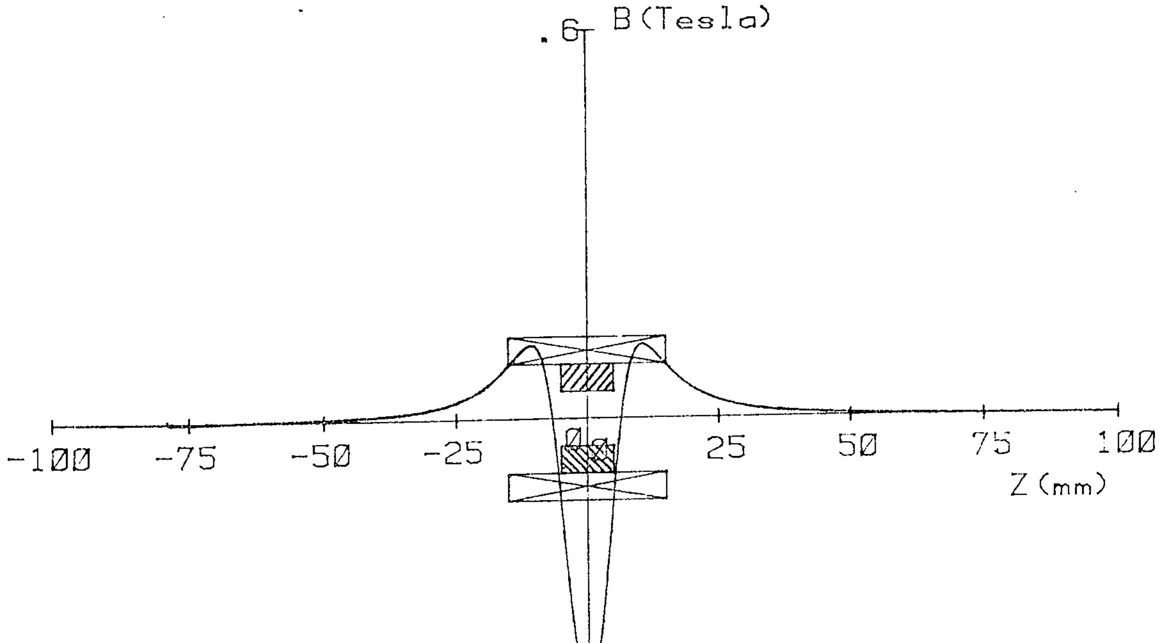

Figure 3.6: Axial flux density distribution $B_m(z)$ due to magnetisation in magnetic material of the lens of Figure 3.1, calculated directly as explained in chapter 1.

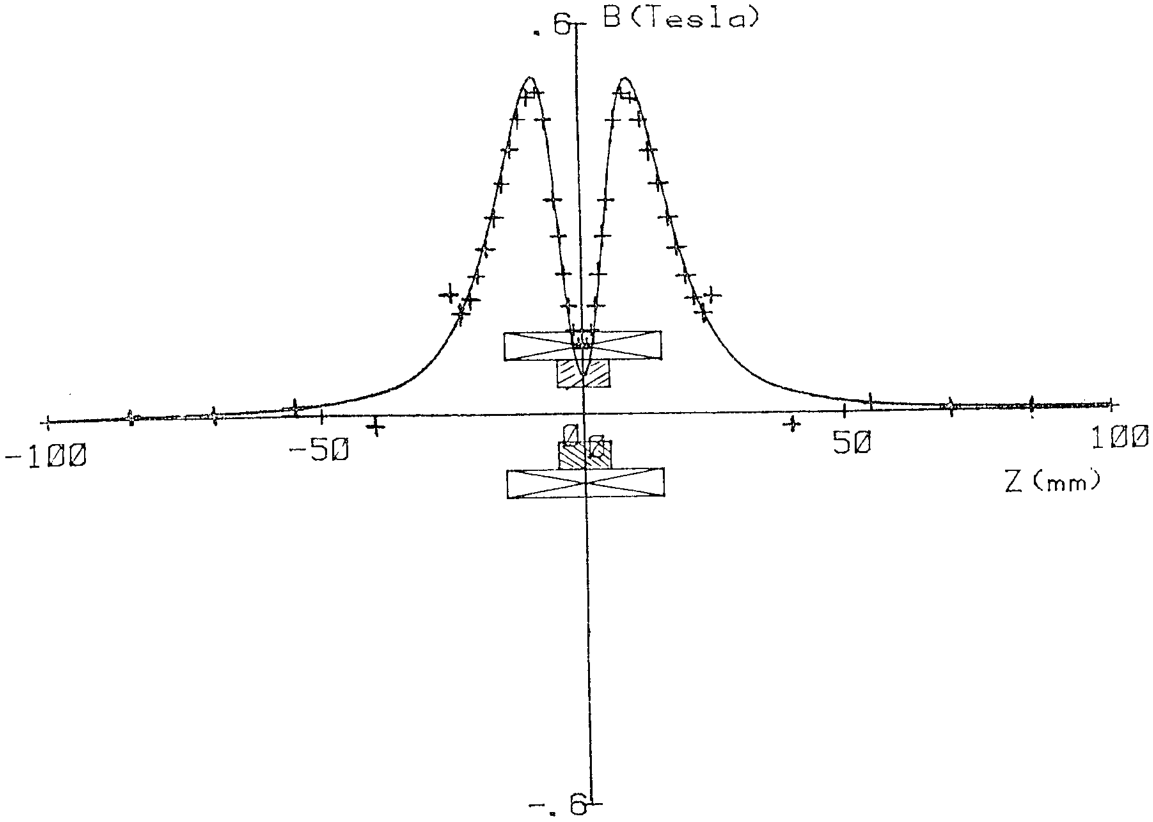

Figure 3.7: The final axial flux density distribution $B_z(z)$ of the lens of Figure 3.1 using the DIFINT program (——). Crosses (+++) indicate RUN 1 computed values that are plotted for comparison purposes.

CHAPTER 4

CALCULATION OF ABERRATIONS IN MAGNETIC ELECTRON LENS SYSTEMS

4.1 Aberration in magnetic electron lenses:

The design of an electron lens does not end with the determination of its field distribution. Further analysis is needed to calculate its aberrations; these should be within tolerable limits for the application in mind.

Magnetic electron lenses are used to form electron images. A perfect image is called a Gaussian image and the electrons that form this image follow paths that are called Gaussian rays or trajectories. Gaussian trajectories satisfy the paraxial equation,

$$\frac{d^2r}{dz^2} + \frac{\eta}{8V_r} B^2 r = 0 \qquad (4.1)$$

where V_r is the relativistic accelerating voltage , B is the axial flux density and η is the charge to mass ratio of the electron,

$$\eta = \left| e/m \right| \qquad (4.2)$$

In general electrons do not follow gaussian trajectories but arrive at the image at some distance from the corresponding Gaussian image point. This departure from a perfect image point in a magnetic lens is called the aberration. The image aberration may be expressed in terms of coefficients. These coefficients are of two types, real coefficients and asymptotic coefficients. They are expressed in the form of integral relations as functions of the field and the Gaussian electron trajectories. A general Gaussian trajectory can be determined as a linear combination of two particular Gaussian rays;

their choice is arbitrary but they must be linearly independent. Here we adopt the particular rays introduced by Glaser (1952).

4.1.1 Particular Gaussian rays for a system with an aperture:

The two particular rays referred to as g and h are shown in Figure 4.1. They are defined by their heights in the object and aperture planes; they have the values,

$$\begin{aligned} g(z_o) &= 1, \quad g(z_a) = 0 \\ h(z_o) &= 0, \quad h(z_a) = 1 \end{aligned} \tag{4.3}$$

where z_o is the position of the object plane and z_a is the position of the aperture plane.

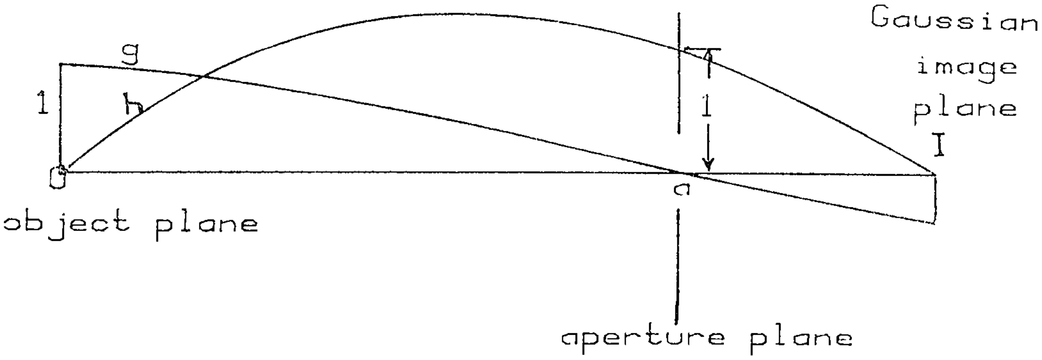

Figure 4.1: Particular rays, g and h, for a system with aperture

4.1.2 Particular rays for aperture-free system:

For an aperture-free system, the two particular rays are referred to as s and t. They are defined by their heights and slopes in the object plane; they are shown in Figure 4.2 and given by,

$$\begin{aligned} s(z_o) &= 1, \quad s'(z_o) = 0 \\ t(z_o) &= 0, \quad t'(z_o) = 1 \end{aligned} \tag{4.4}$$

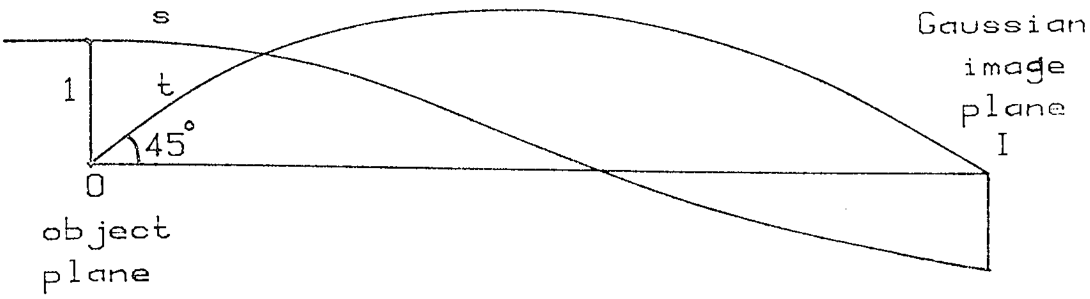

Figure 4.2: Particular rays, s and t, for an aperture-free system.

4.1.3 Particular asymptotic Gaussian rays:

The asymptotic Gaussian rays referred to as G and X are defined in terms of the position and slope of the asymptotes of the rays in the virtual object plane, (Figure 4.3), and are given for the condition of finite conjugates by,

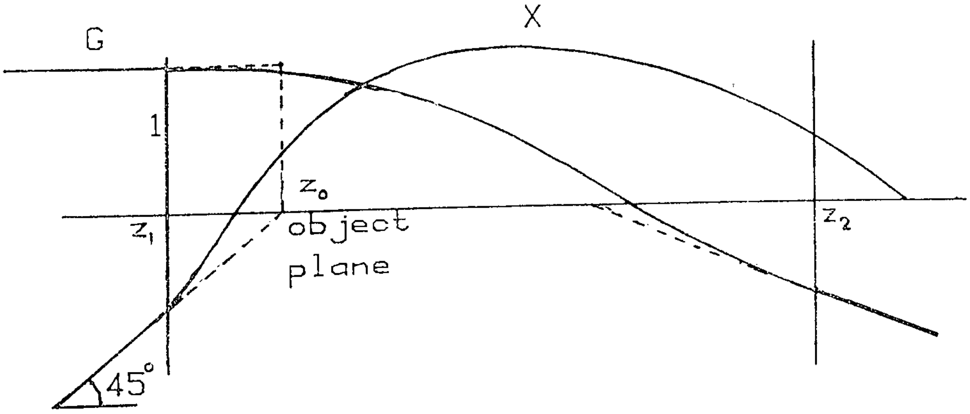

Figure 4.3: Particular asymptotic Gaussian rays, G and X, for the condition of finite conjugates.

$$G(z_o) = 1, \quad G'(z_o) = 0$$
$$X(z_o) = 0, \quad X'(z_o) = 1 \tag{4.5}$$

But since the contribution to the aberration starts from the start of the magnetic field at z_1, hence the two particular rays are defined at z_1 by,

$$G(z_1) = 1 \quad , \quad G'(z_1) = 0$$
$$X(z_1) = z_1 - z_o, \quad X'(z_1) = 1 \tag{4.6}$$

For the condition of infinite magnification, the two particular asymptotic Gaussian rays are called G and H, as shown in Figure 4.4. The ray G is the same as before and H is a special case of the ray X where z_o coincides with the projector focal point F_{proj}. This ray leaves the lens field parallel to the axis with a height equal to

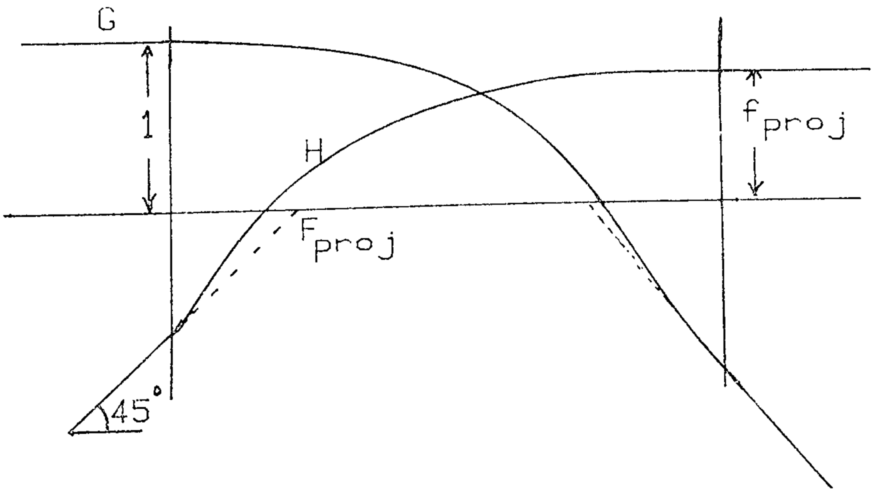

Figure 4.4: Particular asymptotic Gaussian rays, G and H, for infinite magnification condition.

the projector focal length f_{proj}. For computational purposes the ray H can be calculated with the help of another ray $\overline{H}$ as shown in Figure 4.5. The ray $\overline{H}$ is defined at the end of the field at distance z_2 by,

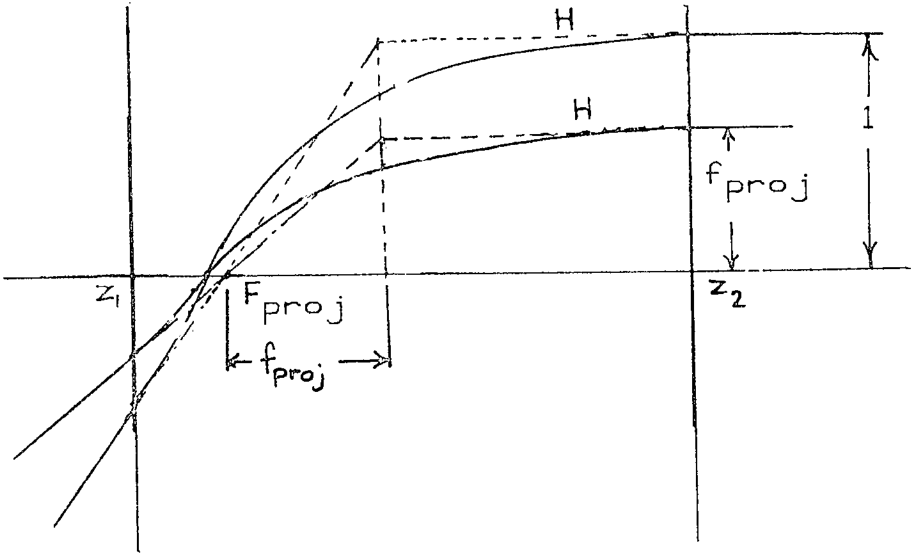

Figure 4.5: Tracing of ray H with the help of ray $\overline{H}$.

$$\overline{H}(z_2) = 1, \quad \overline{H}'(z_2) = 0 \tag{4.7}$$

Multiplying the values of $\overline{H}$ and $\overline{H}'$ at any point by the projector focal length f_{proj} yields the ray H.

4.2 Real aberrations:

These aberrations are important in objective electron lenses, where the object is very small. Two aberrations are to be discussed, namely the spherical aberration and the chromatic aberration.

4.2.1 Spherical aberration:

The spherical aberration produces a blurred image, in the Gaussian image plane, for a point in the object plane. This is due to the difference in focussing action of the lens field on rays leaving the object point with different angles, Figure 4.6. The spherical aberration is expressed in terms of the coefficient C_{si}, given by,

$$C_{si} = \Delta r_i / \gamma_i^3 \tag{4.8}$$

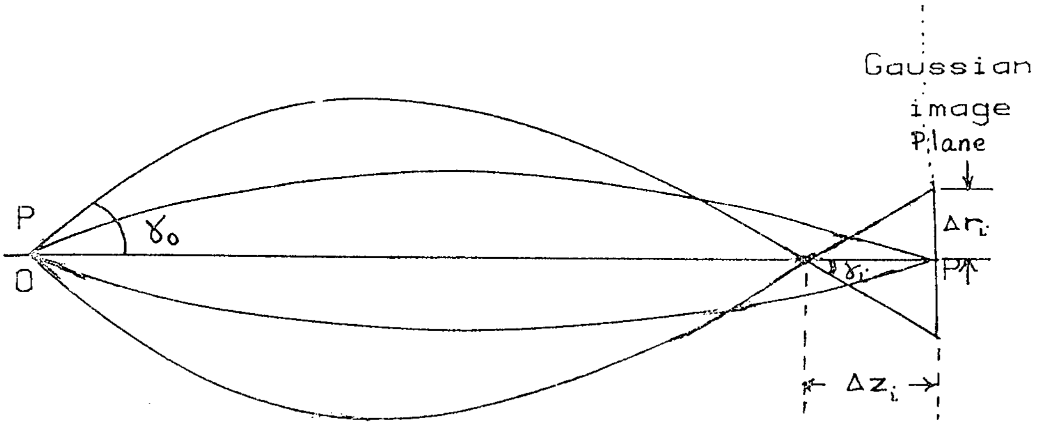

Figure 4.6: Effect of spherical aberration on the image of a point object.

where Δr_i is the radius of disk of confusion at the Gaussian image plane and γ_i is the angle made by the aberrated ray and the axis in the image side. This ray leaves the object with an angle γ_o. The coefficient C_{si} is called the spherical aberration coefficient with respect to the image plane. The spherical aberration coefficient with respect to object plane, C_{so}, is defined by,

$$C_{so} = \Delta r_o / \gamma_o^3 \tag{4.9}$$

where Δr_o is the radius of disk of confusion in object plane if the ray leaves the image plane with angle γ_i. The relation between the two coefficients is given by,

$$C_{si} = M^4\, C_{so} \tag{4.10}$$

where M is the magnification of the lens.

The spherical aberration C_{so} is given by Glaser (1954),

$$\begin{aligned} C_{so} &= \frac{1}{h_a'^4\sqrt{V_r}} \int_{z_0}^{z_i} \left[L h^4 + 2N h^2 h'^2 + \frac{\sqrt{V_r}}{2} h'^4 \right] dz \\ C_{so} &= \frac{1}{\sqrt{V_r}} \int_{z_0}^{z_i} \left[L t^4 + 2N t^2 t'^2 + \frac{\sqrt{V_r}}{2} t'^4 \right] dz \end{aligned} \tag{4.11}$$

where, $L = \frac{1}{32\sqrt{V_r}}\left[\frac{\eta^2 B^4}{4V_r} - 2\eta B B''\right]$ and $N = \frac{\eta}{16\sqrt{V_r}} B^2$, and B'' is the second derivative of the field B with respect to z.

4.2.2 Chromatic aberration:

This aberration causes a shift of the image point axially due to change in accelerating voltage ΔV, as shown in Figure 4.7. For an

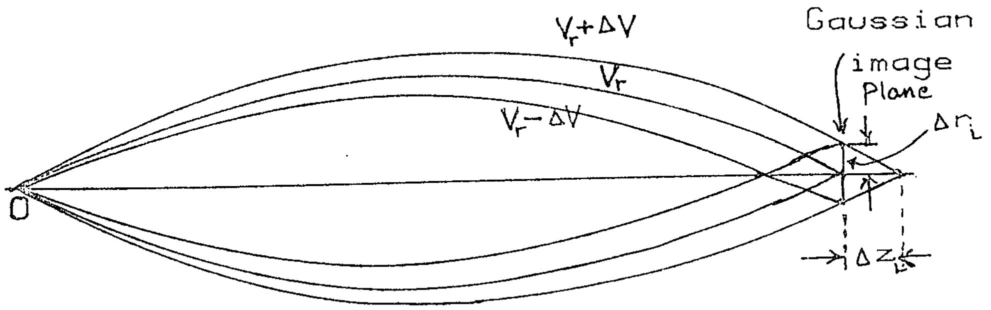

Figure 4.7: Effect of chromatic aberration on the image of a point object.

electron beam of voltage $V_r \pm \Delta V$, this will produce a blurred image of axial extent $2\Delta z_i$. The aberration is expressed in terms of a coefficient C_{co} when referred to the object plane and C_{ci} when referred to the image plane.

$$C_{ci} = \Delta z_i \,/\, \left(\frac{\Delta V}{V_r}\right) \qquad (4.12)$$

and,

$$C_{ci} = M^2\, C_{co} \qquad (4.13)$$

The disk of confusion in the Gaussian image plane is given by,

$$\Delta r_i = M\, C_{co}\, \gamma_o \left(\frac{\Delta V}{V_r}\right) \qquad (4.14)$$

and C_{co} is given (Hawkes, 1972) by,

$$C_{co} = \frac{\eta}{8V_r}\int_{z_o}^{z_i} B^2 t^2\, dz \qquad (4.15)$$

4.2.3 Outline of the real aberration program (REALAB):

Figure 4.8 represents a block diagram for the real aberration computer program (REALAB). The magnetic field of the lens is divided into equal intervals using a cubic spline technique (Shampine and Allen, 1973). The particular ray t or h are calculated by solving the paraxial ray equation 4.1, using fourth order Runge-Kutta method and the aberration integrals are evaluated using Simpson's rule (James et al,1967).

To illustrate the use of the above program we apply it to the calculation of the real aberrations of the field distribution of the magnetic lens of Figure 2.2. The spherical aberration C_s and the chromatic aberration coefficient C_c are shown in Figure 4.9 as a funcion of the excitation parameter $NI/V_r^{\frac{1}{2}}$.

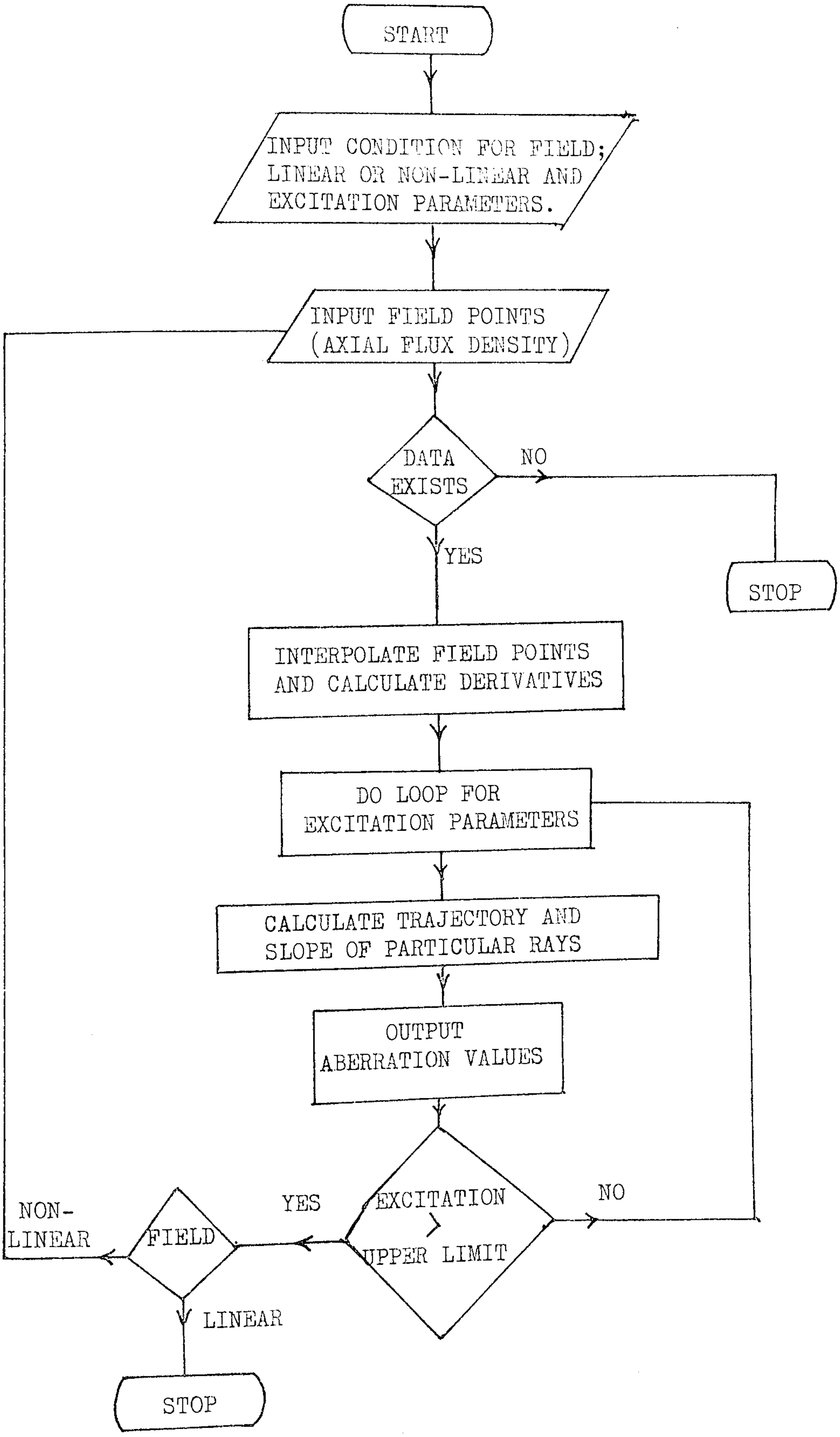

Figure 4.8: Block diagram of the REALAB program.

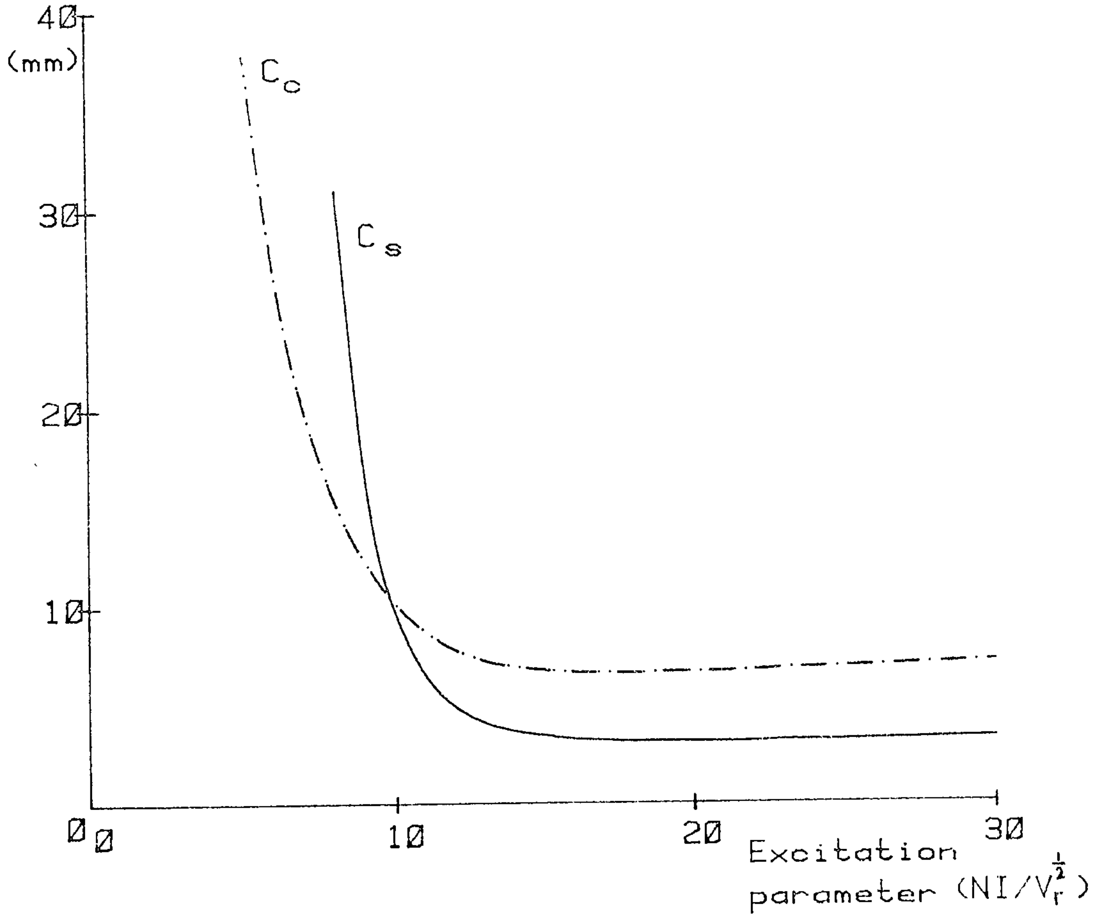

Figure 4.9: The spherical aberration coefficient C_s and the chromatic aberration coefficient C_c as a function of the excitation parameter $NI/V_r^{\frac{1}{2}}$. C_s is indicated by the solid line and C_c is indicated by the broken line.

4.3 Asymptotic aberrations:

The asymptotic aberrations are those that mostly affect the projector system in the electron microscope. They affect the images of off-axis object points since their values depend on the height of the object point from the lens axis. The aberrations to be considered are the chromatic change in magnification, chromatic change in image rotation, radial distortion and spiral distortion.

4.3.1 Chromatic change in magnification:

This aberration causes a shift in the image point radially due to change in accelerating voltage ΔV, as shown in Figure 4.10. For an electron beam leaving the object point P_o with voltage $V_r \pm \Delta V$, the image of P_o will be blurred and of radial spread of distance $2\Delta r_i$.

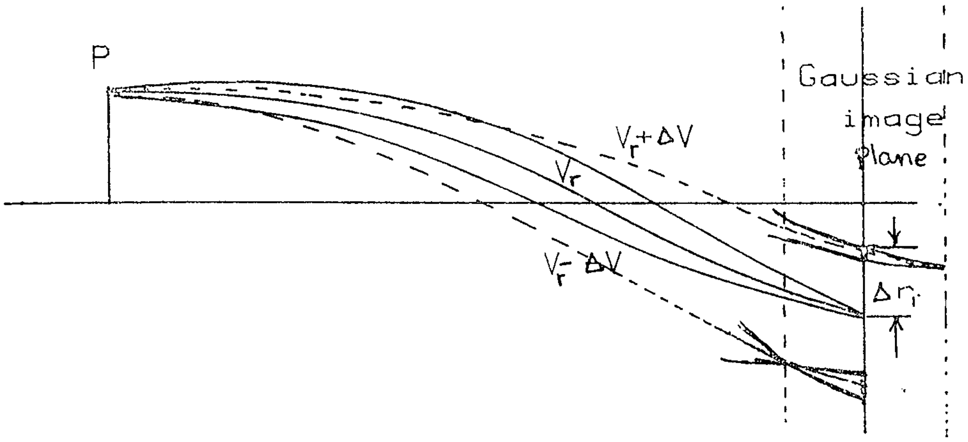

Figure 4.10: Effect of chromatic change in magnification on the image of an off axis object point P_o.

The coefficient of chromatic change in magnification, C_M is given (Hawkes, 1972), when referred to object plane by,

$$C_{Mo} = \frac{\eta}{8V_r}\int_{-\infty}^{\infty} B^2 G X \, dz \tag{4.16}$$

For rays incident parallel to the axis, Δr_i is given by,

$$\Delta r_i = M \, C_{Mo} \, r_o \left(\frac{\Delta V}{V_r}\right) \tag{4.17}$$

where r_o is the height of the object point P_o from the axis. The coefficient of chromatic change of magnification when referred to the image plane (C_{Mo}) is given by,

$$C_{Mi} = C_{Mo} M^2 \tag{4.18}$$

For infinite magnification condition,

$$C_{Mo} = \frac{\eta}{8V_r}\int_{-\infty}^{\infty} B^2 GH \, dz \tag{4.19}$$

4.3.2 Chromatic change in image rotation:

This aberration will cause a blurred image in an arc of distance $2\Delta\rho$, where $\Delta\rho$ is given by,

$$\Delta\rho = M \, C_{\theta o} \, r_o^2 \left(\frac{\Delta V}{V_r}\right) \tag{4.20}$$

where $C_{\theta o}$ is the coefficient of chromatic change in image rotation and is given by,

$$C_{\theta o} = \frac{\eta}{8V_r}\int_{-\infty}^{\infty} B \, dz \tag{4.21}$$

for rays incident parallel to the axis. When referred to the image plane,

$$C_{\theta i} = M^2 C_{\theta o} \tag{4.22}$$

This aberration occurs in magnetic fields due to the change in rotation of electrons of different energies where they have to spend different times in the magnetic fields.

4.3.3 Radial distortion:

Radial distortion is due to the change in refractive power of the magnetic field as the incident electron beam enters it at increasing distances from the axis. It causes a radial shift in the image point as shown in Figure 4.11, but it does not affect the sharpness of the image because the imaging pencils are of small angles. The image point of distance ρ from the centre of the Gaussian image will be shifted radially by an amount $\Delta\rho$ which is given by,

$$\Delta\rho = M\,D_{rd}\,r_o^3 \tag{4.23}$$

where r_o is the height of the object point from the axis and D_{rd} is the radial distortion coefficient given by Glaser (1952), with change of notation,

$$D_{rd} = D_o - D_1/\ell + D_2/\ell^2 - D_3/\ell^3 \tag{4.24}$$

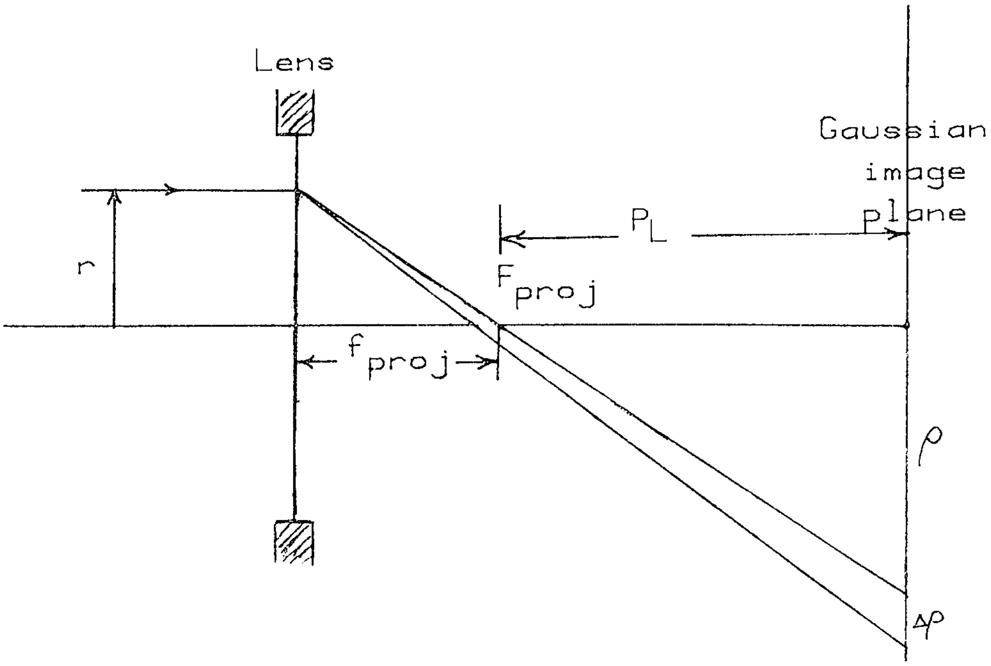

Figure 4.11: Effect of radial distortion on the image of a point. f_{proj}, F_{proj} and P_L are the projector focal length, projector focus and projection length respectively.

with,

$$D_o = \frac{1}{X_o'\sqrt{V_r}}\int_{-\infty}^{\infty}\left[LG^3X + NGG'(GX' + G'X) + \frac{\sqrt{V_r}}{2}G'^3X\right]dz \tag{4.25}$$

$$D_1 = \frac{1}{\sqrt{V_r}} \int_{-\infty}^{\infty} \left\{ L(2G^2X^2+G^3X)+N\left[2G^2X'^2+2G'^2X^2+GG'(XG)'\right] + \frac{\sqrt{V_r}}{2}(2G'^2X'^2+G'^3X') \right\} dz \qquad (4.26)$$

$$D_2 = \frac{1}{\sqrt{V_r}} \int_{-\infty}^{\infty} \left[LGX^3+NXX'(XG)'+\frac{\sqrt{V_r}}{2}G'X'^3 \right] dz \qquad (4.27)$$

$$D_3 = \frac{1}{\sqrt{V_r}} \int_{-\infty}^{\infty} \left[LX^4+2NX^2X'^2+\frac{\sqrt{V_r}}{2}X'^4 \right] dz \qquad (4.28)$$

and ℓ is the distance from the object position where the tangent to the actual trajectory in the object plane crosses the axis as shown in Figure 4.12.

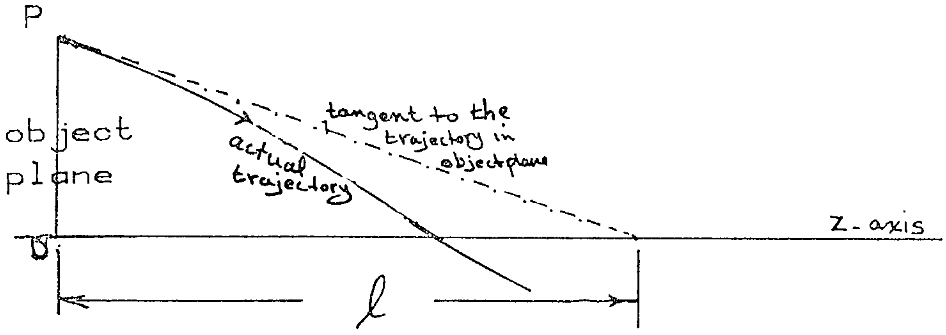

Figure 4.12: Definition of ℓ, the distance from the object plane to where the tangent to the actual ray in object plane crosses the axis.

For rays that enter the lens parallel to the axis, $\ell \longrightarrow \infty$ and hence,

$$D_{rd} = D_o \qquad (4.29)$$

The effect of radial distortion on the appearence of the image of a square mesh is shown in Figure 4.13. A barrel distortion occurs for negative $\Delta\rho$ and a pincushion distortion for positive $\Delta\rho$.

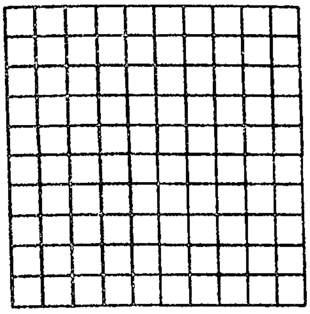

Gaussian image

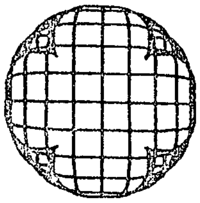

image with
barrel distortion

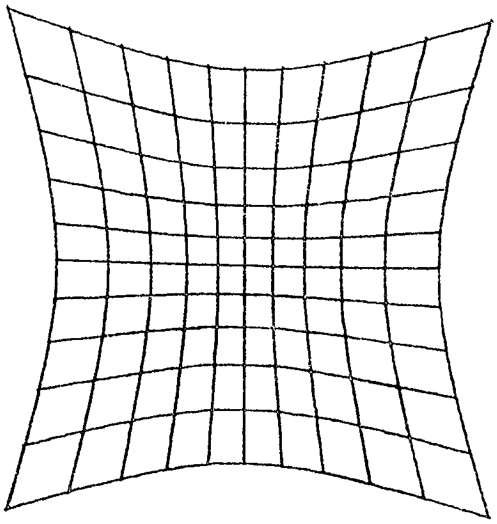

image with
pincushion distrotion

Figure 4.13: Effect of radial distortion on the appearence of the image of a square mesh.

4.3.4 Spiral distortion:

The magnetic field affects the rotation of the image differently at different radial heights. This has the effect of shifting the image of a point in the object plane of height r_o by an arc of length $\Delta\rho$ in the image plane which is given by,

$$\Delta\rho = M\, D_{sp}\, r_o^3 \tag{4.30}$$

where D_{sp} is called the spiral distortion coefficient. It was given by Glaser (1952), with change of notation, by

$$D_{sp} = d_o - d_1/\ell + d_2/\ell^2 \tag{4.31}$$

with,

$$d_o = \int_{-\infty}^{\infty} (PG^2 + QG'^2)\, dz \tag{4.32a}$$

$$d_1 = 2\int_{-\infty}^{\infty} (PGX + QG'X')\, dz \tag{4.32b}$$

$$\text{and, } d_2 = \int_{-\infty}^{\infty} (PX^2 + QX'^2)\, dz \qquad (4.32c)$$

$$P = \frac{1}{16}\sqrt{\frac{\eta}{2V_r}}\left[\frac{\eta B^3}{2V_r} - B^3\right] \qquad (4.33)$$

$$Q = \frac{1}{4}\sqrt{\frac{\eta}{2}}\,\frac{B}{V_r} \qquad (4.34)$$

For rays incident parallel to the axis, $\ell \longrightarrow \infty$, and hence

$$D_{sp} = d_o \qquad (4.35)$$

The effect of spiral distortion on the image of a square grid is shown in Figure 4.14.

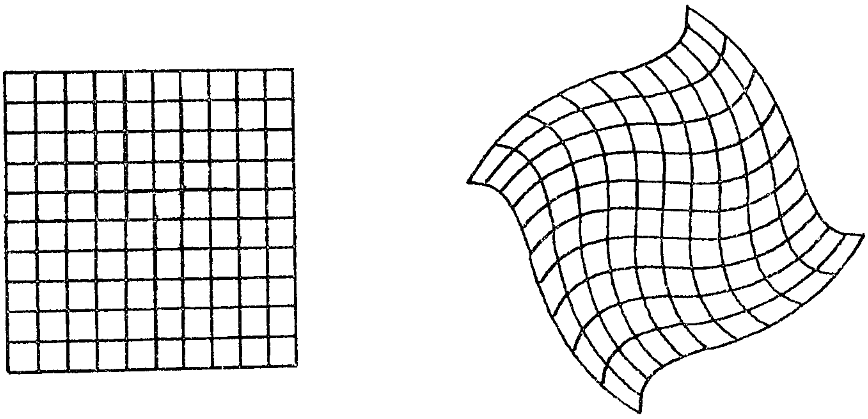

Gaussian image

image with spiral distortion

Figure 4.14: Effect of spiral distortion on the image of a square grid.

4.3.5 The distortion factor (F):

From the geometry of Figure 4.11, we have

$$\frac{P_L}{f_{proj}} = \frac{\rho}{r_o} \qquad (4.36)$$

where P_L is the distance of the projected image from the focal point F_{proj}.

$$r_o = f_{proj} \cdot \frac{\rho}{P_L} \qquad (4.37)$$

Substituting for r_o (equation 4.37) in equation 4.23, with the magnification $M = \rho/r_o$, we get,

$$\frac{\Delta\rho}{\rho} = D_{rd}\, f_{proj}^{2}\, \frac{\rho^{2}}{P_L^{2}} \tag{4.38}$$

$$\frac{\Delta\rho}{\rho} = F_{rd}\, \frac{\rho^{2}}{P_L^{2}} \tag{4.39}$$

where,

$$F_{rd} = D_{rd} \cdot f_{proj}^{2} \tag{4.40}$$

where we call F_{rd}, the radial distortion factor. Similarly the spiral distortion factor,

$$F_{sp} = D_{sp} \cdot f_{proj}^{2} \tag{4.41}$$

4.3.6 Expression of asymptotic aberration coefficients for finite conjugates in terms of rays for infinite magnification:

The ray X for finite conjugate condition can be expressed as the linear combination of the ray H and the ray G for infinite magnification condition as,

$$X = f_{proj}(H - G/M) \tag{4.42}$$

and,

$$X' = f_{proj}(H' - G'/M) \tag{4.43}$$

Substituting for X and X', from equations 4.42 and 4.43, equations 4.16, 4.25-28 and 4.32-34 can be expressed in terms of the rays H and G for the infinite magnification condition and the magnification M. The aberration coefficients for finite conjugates were derived by Hawkes (1970) in the form of polynomials in terms of the magnification and the rays for infinite magnification condition. However the asymptotic programs discussed below are used to calculate the asymptotic aberration coefficients directly without the need for such polynomials.

4.4 Programs for the calculation of asymptotic aberrations:

Presently available programs are often severely restricted in scope. For example the asymptotic aberration calculations in the Munro program (1975) is restricted to the calculation of spherical aberration and chromatic aberration which are of less importance for projector electron lenses than are radial and spiral distortion. Marai (1977) developed an asymptotic program for the calculation of distortion coefficients but this was restricted to parallel incoming rays. Neither of the above programs calculate the aberration coefficients for more than one lens field distribution at a time. This is clearly inconvenient when calculating multi-lens systems.

The author's programs can deal with both linear and non-linear magnetic field distributions consisting either of one lens or a system of two lenses. However they can be readily extended if necessary. A block-diagram for the linear program (SYSLIN) is shown in Figure 4.15, and a block-diagram for the non-linear program (SYSSAT) is shown in Figure 4.16. The aberration coefficients are calculated either in terms of the actual excitation applied to the lens or in terms of the relative excitation which is the effective excitation after the cancellation effect of the magnetic field when excitations oppose each other, i.e. the current in one coil flows in opposite direction to the current flowing in the other coil.

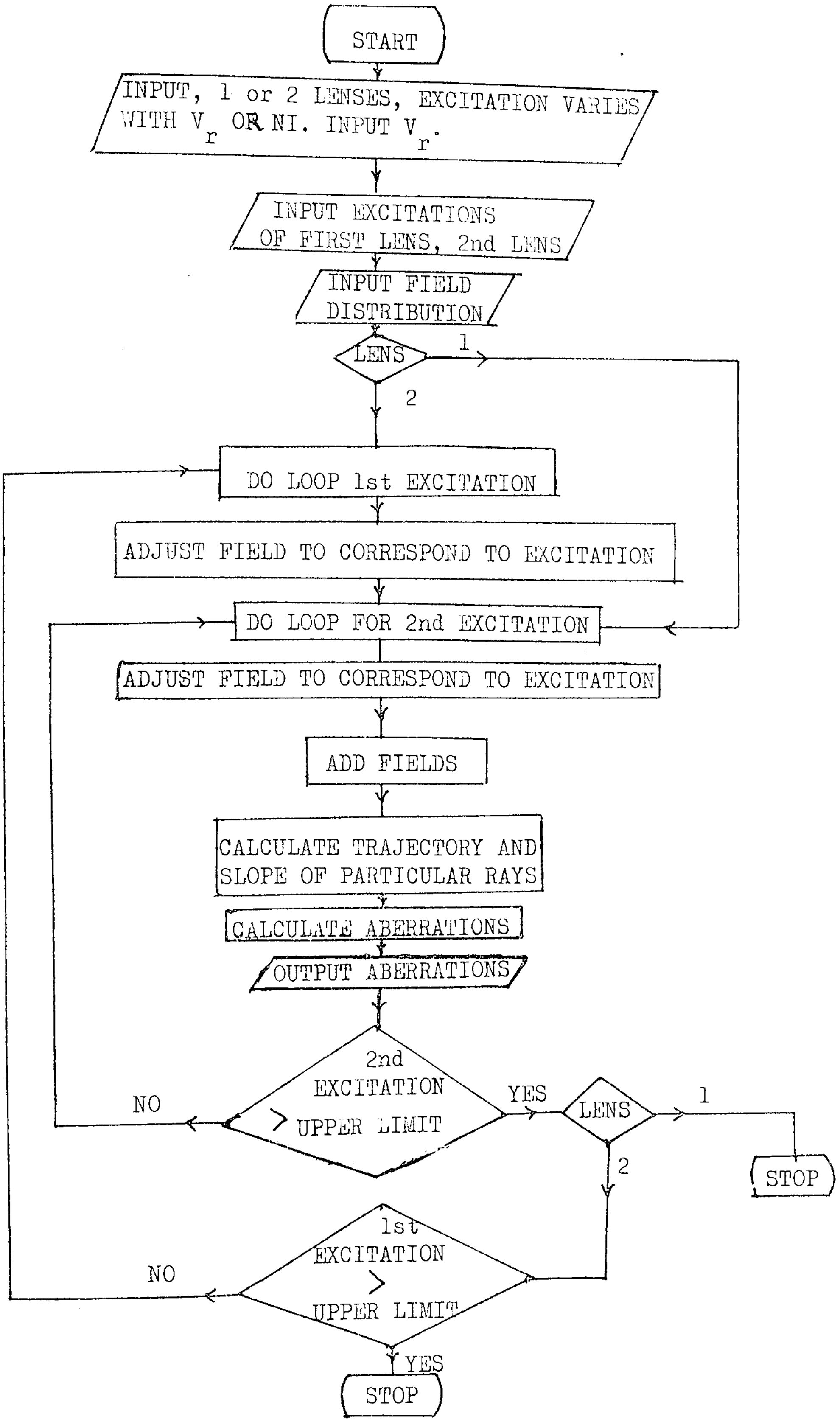

Figure 4.15: Block-diagram for the SYSLIN program.

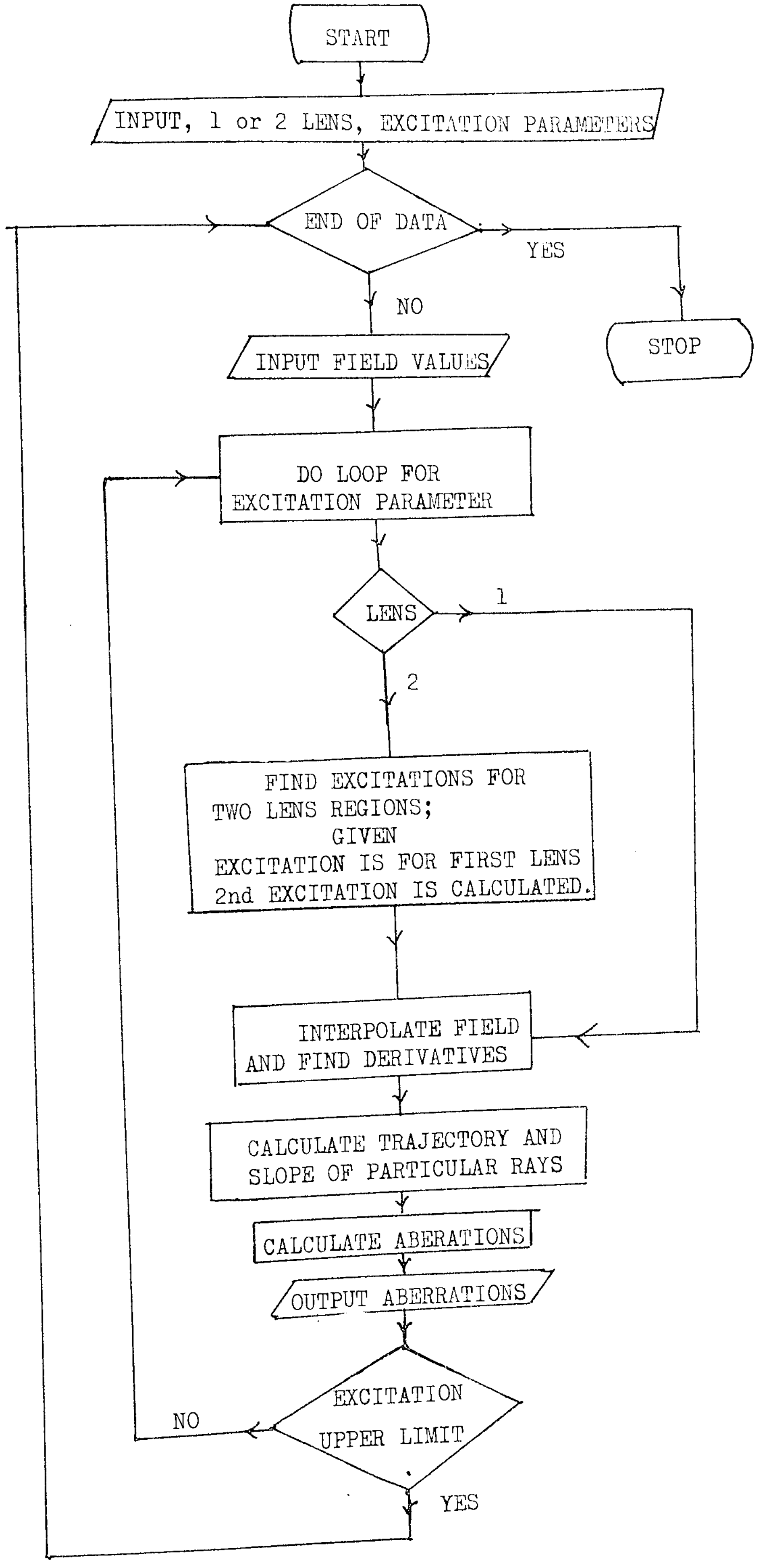

Figure 4.16: Block-diagram for the SYSSAT program.

4.5 Application of the asymptotic program to the design of a wide-angle projection system:

The projection angle, i.e. the angle subtended by the image diameter at the projector focus, is limited by the amount of distortion tolerable in the image. A projection system that corrects for distortion can achieve a wide projection angle. The SYSLIN program was applied to check the design of an existing wide-angle projection system (Al-Hilly, 1980) shown in Figure 4.17. The system consists of two parts, one acts as a projector lens and the other as a corrector lens in which the current flows in the opposite direction to that of the current in the projector lens. The axial flux density distribution for the projector lens with the corrector coil switched off is shown in Figure 4.18a. Radial and spiral distortion factors of the projector field are shown in Figure 4.18b. The projector lens is operated at the excitation that gives minimum distortion. The axial field distribution of the system field, with corrector and projector energised is shown in Figure 4.19a. Radial and spiral distortion factors of the system field as a function of the corrector excitation are shown in Figure 4.19b. Experimental measurements for this system

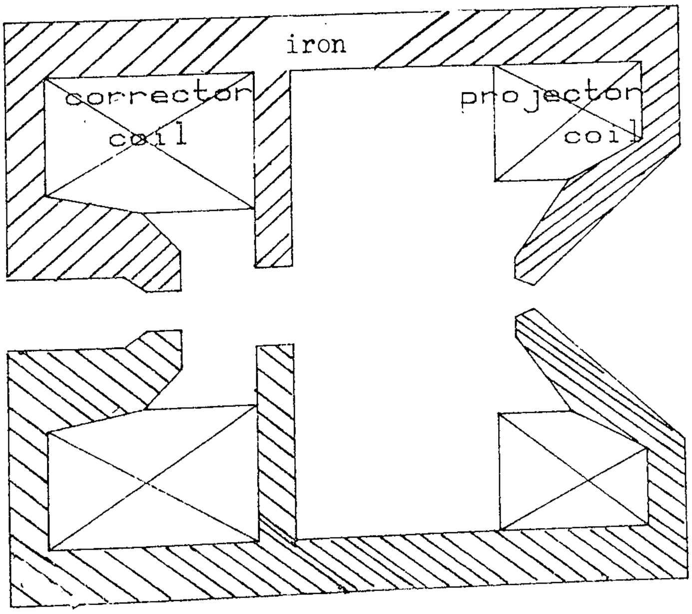

Figure 4.17: Design of a wide-angle projection system.

showed a corrected image with a projection angle of more than 55°. Good agreement was obtained between the calculated and experimental results.

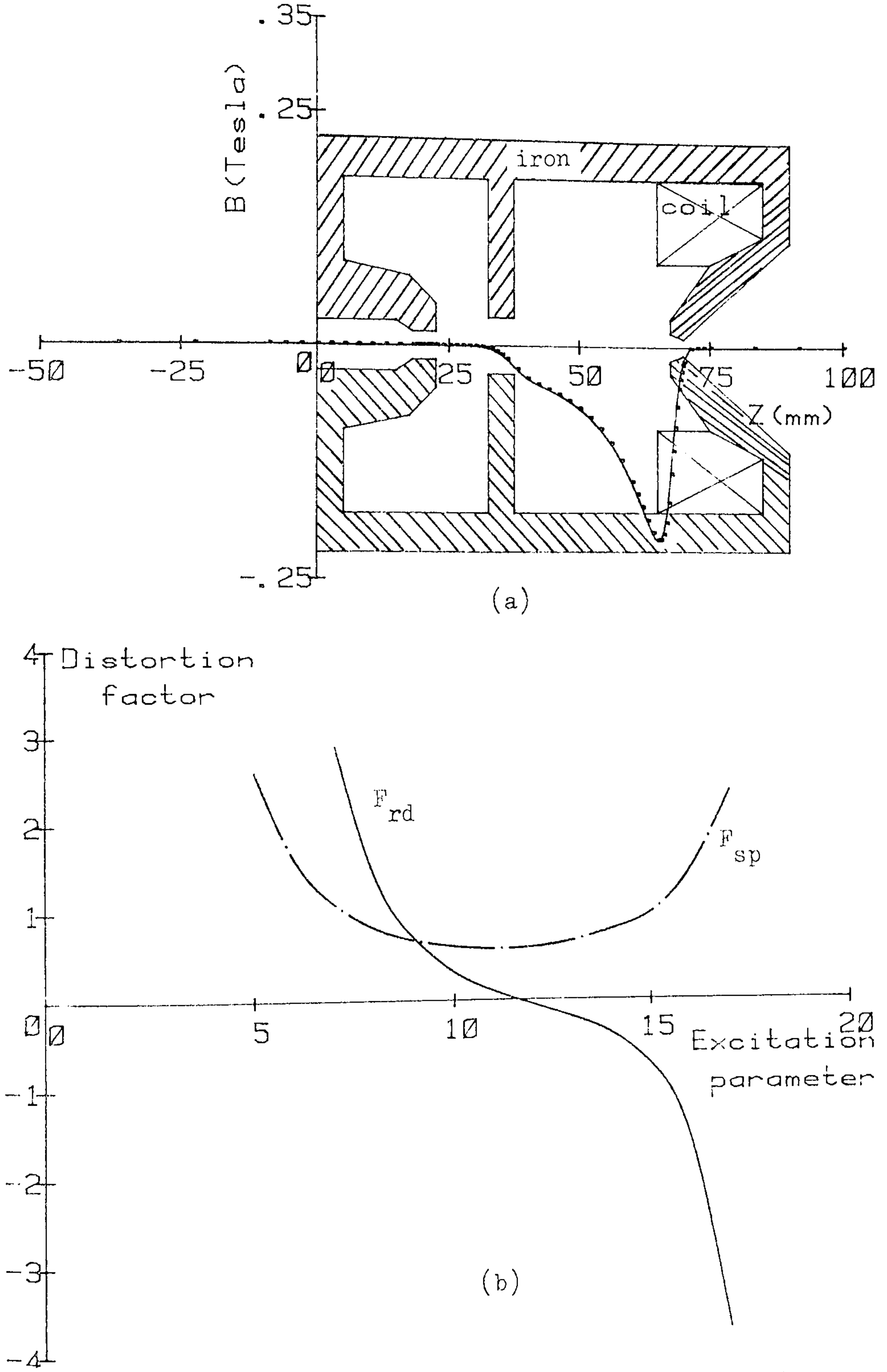

Figure 4.18: Wide angle projection system with corrector switched off. a) axial flux density distribution b) radial and spiral distortion factors as function of projector excitation parameter.

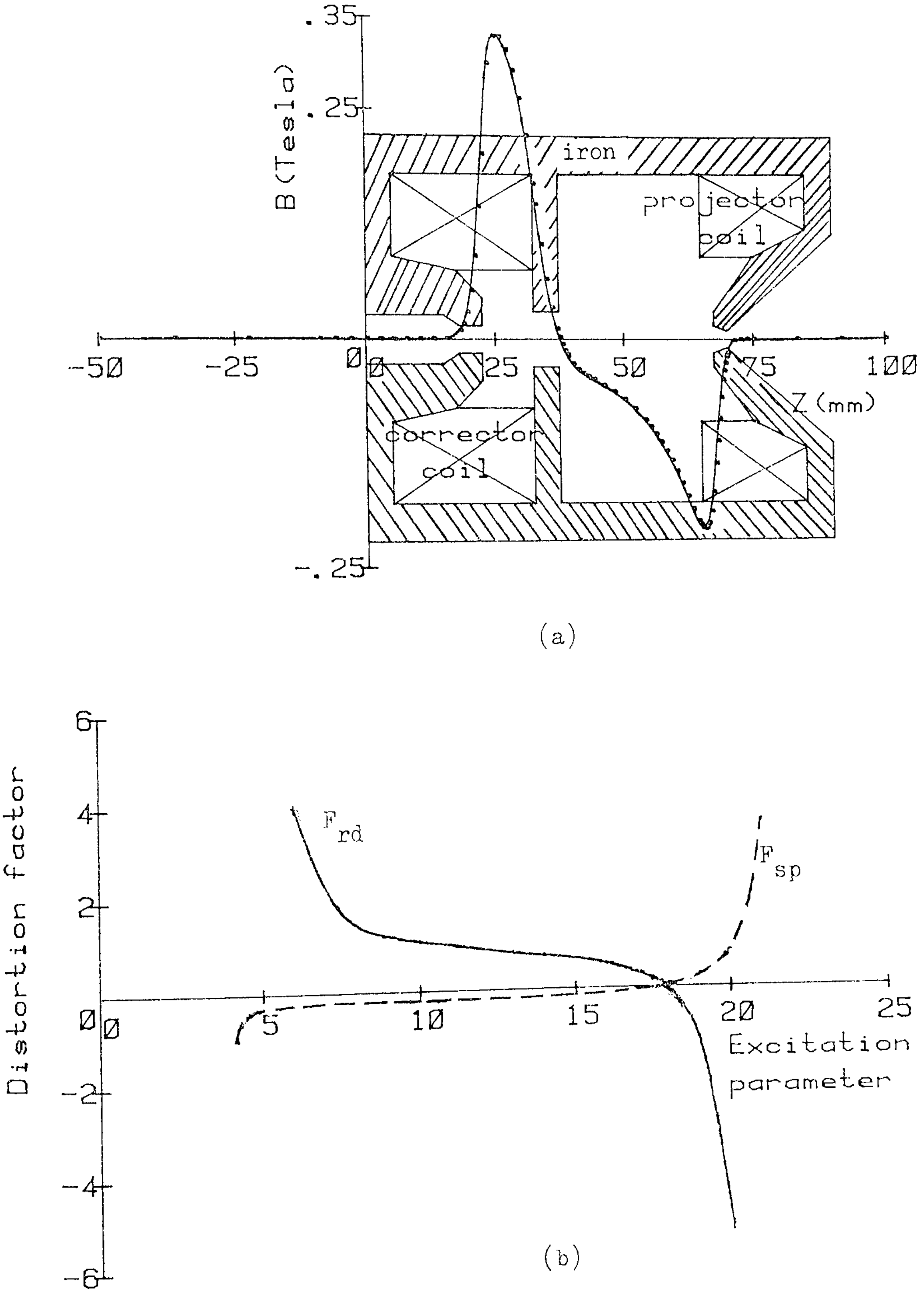

Figure 4.19: Wide angle projection system with corrector and projector energised. a) axial flux density distribution b) radial and spiral distortion factors as function of corrector excitation parameter.

4.6 Computer simulation of images in electron microscopes:

Even when the distortion coefficients of a lens system are known it is often difficult to visualize the appearance of the actual image. The projected image in the electron microscope can however be simulated on a computer once the corresponding distortion factors are known (Nasr, 1978). These factors are calculated by the asymptotic SYSLIN and SYSSAT programs presented earlier. Figure 4.20 shows simulated images for selected values of F_{rd} and F_{sp} (radial and spiral distortion factors) and total projection angles, 2α.

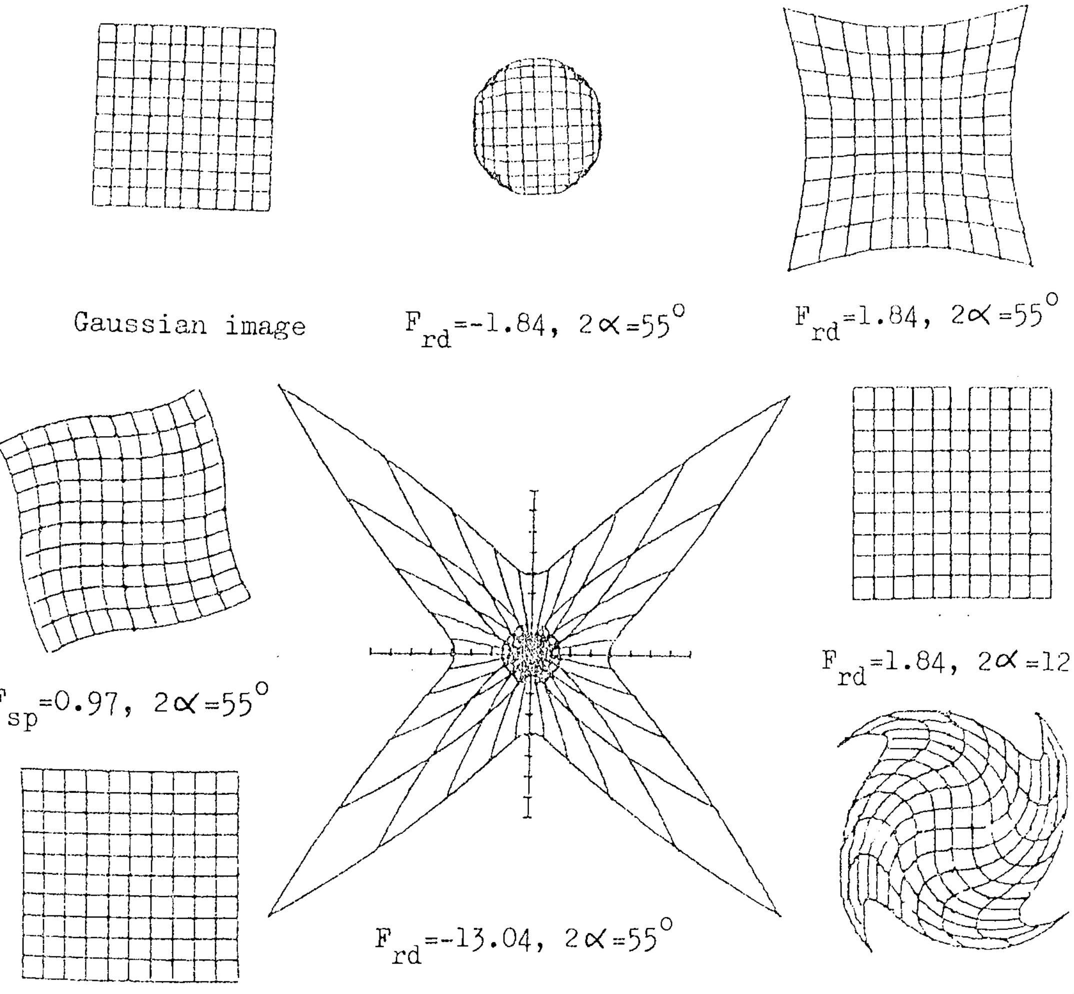

Gaussian image

$F_{rd}=-1.84$, $2\alpha=55^{\circ}$

$F_{rd}=1.84$, $2\alpha=55^{\circ}$

$_{sp}=0.97$, $2\alpha=55^{\circ}$

$F_{rd}=1.84$, $2\alpha=12^{\circ}$

$F_{rd}=-13.04$, $2\alpha=55^{\circ}$

$F_{sp}=6.47$, $2\alpha=55^{\circ}$

$_{sp}=0.97$, $2\alpha=16^{\circ}$

Figure 4.20: Computer simulated images for selected radial and spiral distortion factors (F_{rd} and F_{sp}) and total projection angles (2α).

CHAPTER 5

USE OF MINI-COMPUTERS IN ELECTRON OPTICAL CALCULATIONS

Recent developments in electronics and the introduction of micro circuits have had the effect of reducing the size and cost of electronic devices. This has made it possible for research groups to have their own interactive computing facilities. In electron optics this is not easy to achieve with generally available mini-computers because of the large computer memory required at present to calculate, for example, the field distribution in magnetic lenses. However with improved programs for magnetic field calculation this is now possible due to considerable saving of core store (Mulvey and Nasr, 1980b, 1981). For single-polepiece lenses especially, the store requirement with standard programs is many times that required for the analysis of a conventional lens to a comparable accuracy. The field calculation programs presented in chapters 2 and 3 have the effect of reducing the required store for single-polepiece lenses to that needed when using standard programs for conventional lenses. Thus the design of magnetic lenses becomes more effective since time and effort can be saved by using interactive programming. For example, the calculations can be interrupted at any stage to make small changes in the design of the energizing coil or magnetic circuit in the light of preliminary calculations. Sometimes it may also be desirable to change the mesh size or adjust the boundary conditions.

Even a small personal computer such as the Commodore PET can be useful in the development of programs, especially   programs for determining magnetic field distributions. For example, the development of the programs presented in chapters 2, 3 and 4 were carried out on such a mini-computer system. Figure 5.1 represents the parts of the system used in the developments of the above programs. It consists of the Commodore PET 2001 mini-computer with 32 kbytes of active store; BASIC language is used with BASIC interpreter. A dual drive floppy disk CBM 2040, supplies 340 kbytes of disk store on two floppy disks. More disk store can be achieved if necessary by manual replacement of disks. The PET is of course a slow computer. A problem that needed 1.5 minutes on an ICL 1904S main computer needed 180 minutes on the PET; half of this time was spent on transferring data between the active store and the disk store. But time is not a major concern at the program development stage. The hard copy display system was an Anadex DP-8000 printer. Output was plotted using a Hewlett-Packard 7225A Graphic's plotter with digitising facility enabling data to be input from the plotter to the mini-computer store.

Figure 5.1: Mini-computer system used in developing field calculation, aberration and plotting programs; a) Anadex printer, b) PET mini-computer, c) c) Disk unit and d) HP plotter.

The calculation of the magnetic field distribution of a single-polepiece lens would normally be carried out on a main computer, and certainly not on a small computer such as the PET. However it may be instructive to see how such a complex calculation can be carried out on a PET. The procedure for calculating the magnetic field from a single-polepiece lens using the PET mini-computer can be described as follows:

1) The lens to be analysed is drawn and the data are prepared and fed to the computer. Assume the mesh size is I_1XJ_1 as shown in Figure 5.2. The number of nodal equations will be IJ, where

$$\begin{aligned} I &= I_1 - 2 \\ J &= J_1 - 2 \end{aligned} \qquad (5.1)$$

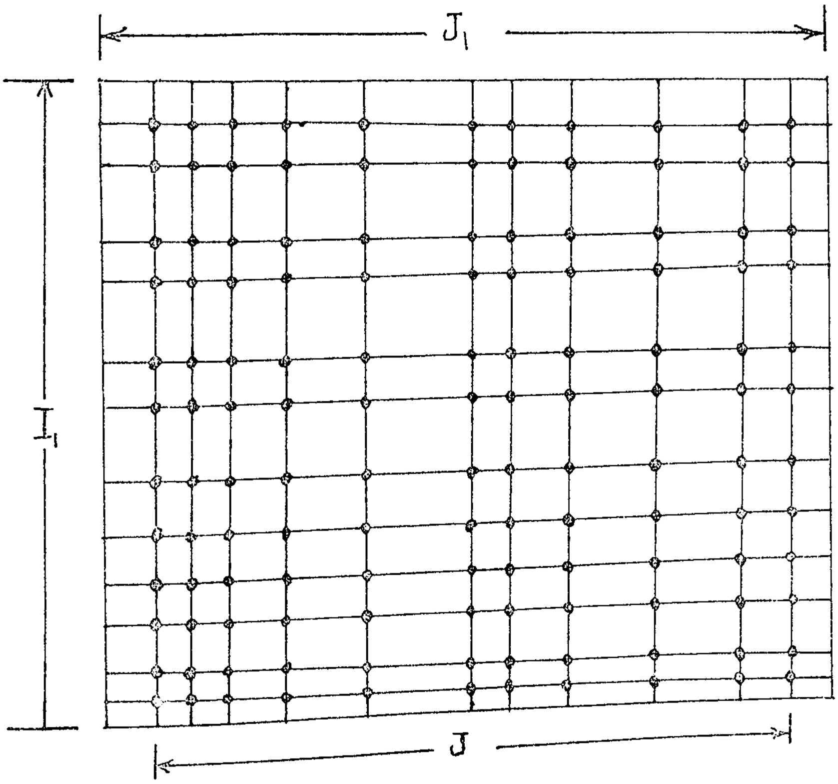

Figure 5.2: Finite element grid of size I_1XJ_1. Nodal equations are generated at the dotted nodes; these nodes are distributed in J columns with I nodes each. $I=I_1-2$, $J=J_1-2$.

2) To store the coefficients of the nodal equations the standard Munro program requires the array P(I,IJ) of size $5(I^2J)$ bytes. By partition technique for equation solving we reduced the array required to P(2I,I) of size $10(I^2)$. For a grid of 19X29 the active store required to store the coefficients is thereby reduced by a factor of 14.

3) To do this, the nodal coefficients for each column of nodal points are calculated and held in the array P(2I,I) before being saved on one disk. The array thus released is re-used to hold the coefficients of the second column of nodal points. This process is repeated until all the coefficients have been calculated and saved in a sequential file. The data thus saved in sequential form can be recalled by reading them in the same way that they were saved, i.e. first saved, first recalled.

4) The nodal equations are then solved by Gaussian elimination; this is carried out by parts as follows. The first 2I equations are recalled from the sequential file on the disk, referred to as disk 0, as shown in Figure 5.3. The elimination is applied to the first I equations which are then saved in a random access file on the other disk, referred to as disk 1. The advantage of a random access file is that the numbers can be saved on the disk in specified blocks which we can access directly. The equations I+1 to 2I are then pushed up to occupy the space that was filled by the equations 1 to I and a new set of I equations are then recalled from the sequential file to fill the space that was occupied by the equations I+1 to 2I, and the situation shown in Figure 5.3 is repeated until all the equations are solved.

5) Back substitution is then carried out by reading the blocks of the random file in the order last written, first read; thus the vector potential distribution of the lens is determined.

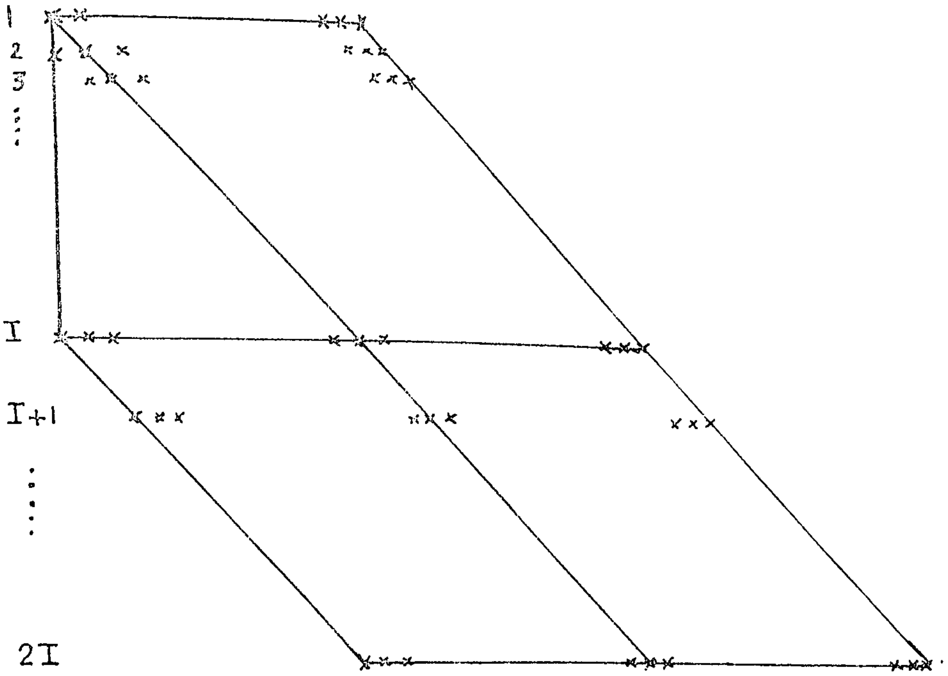

Figure 5.3: Partition technique of equation solving. 2I equations are recalled from disk 0 to active store, eliminate up to I equations then save on drive 1. Push I+1 to 2I equations to occupy the position of 1 to I equations, then recall a new set of equations to occupy the previous I+1 to 2I position. This is repeated until all the equations are solved.

6) From the vector potential distribution, the magnetic flux density and flux distribution in the lens can be obtained.

7) In particular, the flux density distribution can be saved and plotted using a plotting program that was developed for the PET. The saved axial flux density distribution can then be used for the calculation of lens focal properties and aberrations.

An example of the calculations of a magnetic single-polepiece lens using a mini-computer (Mulvey and Nasr, 1981) is given in Appendix 10.

A plotting program was developed for using the HP plotter in conjunction with the PET mini-computer to plot out the calculated axial field distribution of a lens.

Outline of the plotting program:

The program reads the data either from the disk or from data statements in the program. The size of graph is chosen. In plotting the points, the program joins them either by straight lines or by a cubic spline curve. The area under the curve, which is a measure of the ampere turns can be calculated to check for discrepancies in ampere turns. At the same time the lens cross-section can be drawn. An option for other copies of the graph is available. The program also has the facility to take backward steps to correct for mistakes in input data. A block diagram of the plotting program is shown in Figure 5.4. Most of the diagrams in this thesis were produced with the aid of this program.

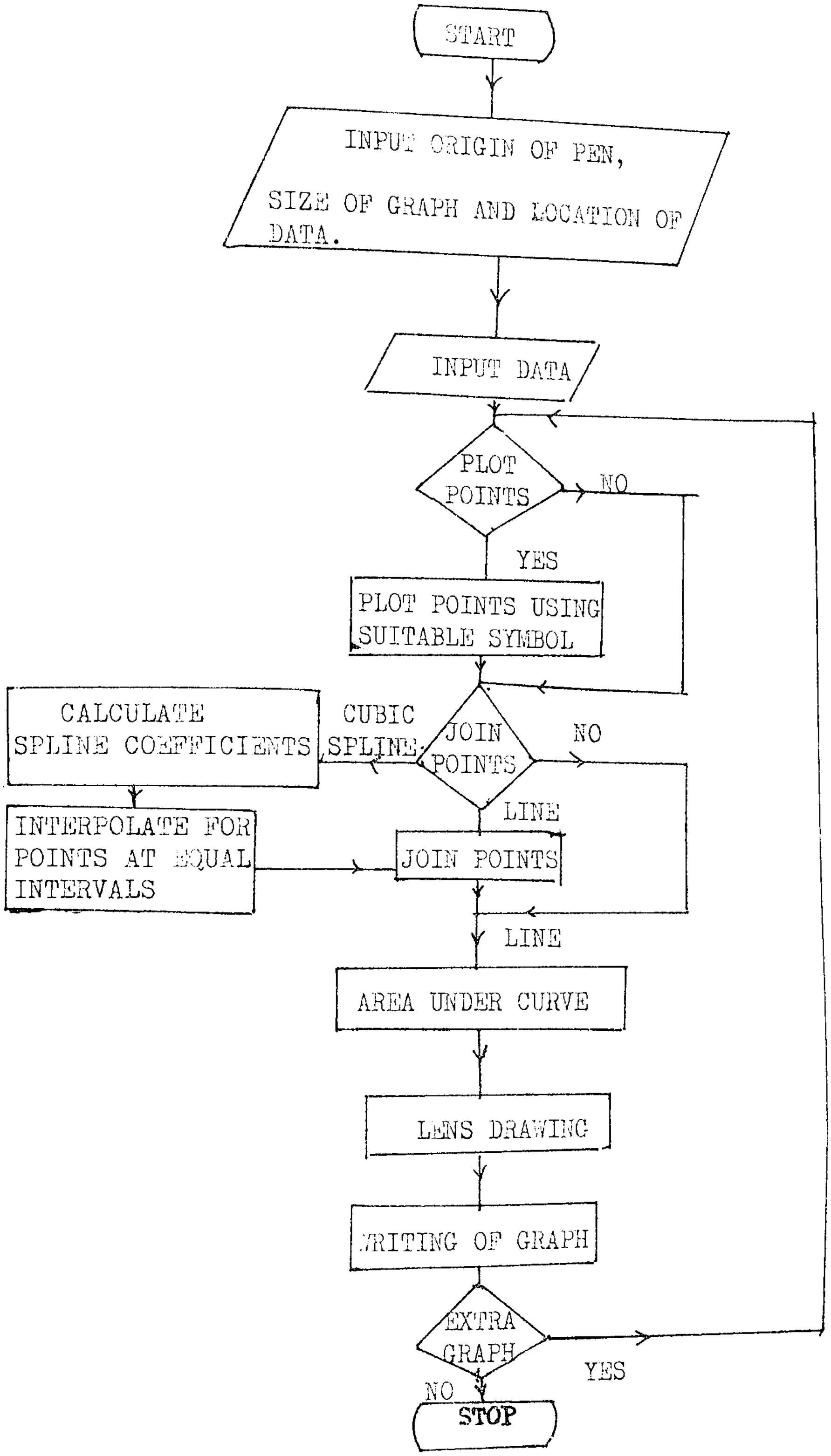

Figure 5.4: Block diagram of the plotting program developed for the HP plotter in conjunction with the PET mini-computer.

CHAPTER 6

CONCLUSION AND DISCUSSION

The finite element method in its two forms, differential and integral, provides a powerful means for calculating electric and magnetic fields. Although this thesis has mainly dealt with magnetic fields, the methods discussed can be equally applied to the calculation of electric fields. In this case a scalar potential program can be used, which is based on the solution of the Laplace's equation, $\nabla^2 U=0$, where U is a scalar potential and the electric field $\underline{E}$ is given by $\underline{E} = -\text{ grad } U$. The corresponding energy functional to the Laplace's equation is given by, $I = \iiint_{\text{Field Volume}} \frac{1}{2} \text{ grad } U . \text{ grad } U \, dv$. Thus, the method employed in the improved differential finite element program could be applied in a revised scalar program. This would have the effect of reducing the large store required at present for calculating the electric field distribution, for example, in field emission guns. Present programs need a very large computer store which makes it impracticable to use in routine analysis for this kind of problem.

In the critical assessment of the differential form of the finite element method with vector potential A=0 on the boundary, the accuracy of the field distribution even in the favourable region near the peak of the field rarely exceeded 1%. The accuracy invariably gets worse as the boundaries are approached. With the improved boundary conditions described in the thesis, not only is the accuracy improved to 0.2% in the favourable region near the peak of the field, but also the gross errors previously encountered near the boundary itself are largely removed.

The integral finite element method avoids these boundary errors.

Moreover it is inherently more accurate in the calculation of the magnetic field on the axis, the chief weakness of the differential method. This makes the integral method, in principle, superior to the differential method. However, the higher computing power needed for the field calculation of electron lenses restricts the method to large computers. Research laboratories with small store computers may therefore not be able to benefit from this method for routine calculations.

The new 'differential-integral' finite element method combines the advantages of both the differential and the integral finite element methods. This method can provide comparable accuracy to that of the integral method but with the lower store requirement of the differential method. Hence, for a limited computing power, the 'differential-integral' finite element method is preferable to either of the above methods used alone.

A new set of programs has been developed for the calculation of the electron optical properties of magnetic electron lens systems. In particular, the new programs provide a powerful tool in the design of wide-angle projection systems for the electron microscope.

Moreover, great efforts have been made to reduce the store requirement needed for the above programs, without loss of accuracy. This makes it feasible to use the above programs on presently available mini-computers, especially when using interactive computing. With such interactive systems it is possible to carry out much of the detailed design of an electron microscope, especially the final optimization of the design, which was previously carried out by time-consuming experiments.

APPENDIX 1

Derivation of the energy functional:

$$I = 2\pi \iint_S (W - JA) r \, dz \, dr \qquad (1.9)$$

From equation 1.4, i.e. $\underline{B} = \text{curl } \underline{A}$, and since $\text{curl} \frac{B}{\mu_o \mu_r} = \underline{J}$, then we have,

$\text{curl}\left(\frac{1}{\mu_o \mu_r} \text{curl } \underline{A}\right) = \underline{J}$ and hence,

$$\frac{1}{\mu_o \mu_r} \nabla \times \nabla \times \underline{A} - \underline{J} = 0 \qquad (A1.1)$$

To find a variational functional we follow the mathematical manipulation below,

$$\int_v \left(\delta \underline{A} \cdot \frac{1}{\mu_o \mu_r} \nabla \times \nabla \times \underline{A}\right) dv - \int_v \underline{J} \cdot \delta \underline{A} \, dv = 0 \qquad (A1.2)$$

The second integral in A1.2 equals $\delta \int JA \, dv$, for a constant current density J.

Using the vector identity,

$$\nabla \cdot \delta \underline{A} \times (\nabla \times \underline{A}) = (\nabla \times \underline{A}) \cdot (\nabla \times \delta \underline{A}) - \delta \underline{A} \cdot \nabla \times (\nabla \times \underline{A}) \qquad (A1.3)$$

the first integral in A1.2 is given by,

$$\int_v \frac{1}{\mu_o \mu_r} (\delta \underline{A} \cdot \nabla \times \nabla \times \underline{A}) \, dv = \int_v \frac{1}{\mu_o \mu_r} (\nabla \times \underline{A}) \cdot (\nabla \times \delta \underline{A}) \, dv - \int \frac{1}{\mu_o \mu_r} \nabla \cdot \delta \underline{A} \times (\nabla \times \underline{A}) \, dv \qquad (A1.4)$$

From Green's theorem,

$$\int_v \frac{1}{\mu_o \mu_r} (\nabla \cdot \delta \underline{A} \times \nabla \times \underline{A}) \, dv = \int_S d\underline{S} \cdot (\delta \underline{A} \times \nabla \times \underline{A}) = 0 \qquad (A1.5)$$

since $\delta A = 0$ on S, the surface area containing the volume v.

Hence,

$$\int_V \frac{1}{\mu_o\mu_r}\left(\delta\underline{A} \cdot \nabla\times\nabla\times\underline{A}\right) dv = \int_V \frac{1}{\mu_o\mu_r}\left(\nabla\times\underline{A}\right) \cdot \left(\nabla\times\delta\underline{A}\right) dv$$

$$= \int_V \frac{1}{2\mu_o\mu_r}\,\delta\left[(\nabla\times\underline{A}) \cdot (\nabla\times\underline{A})\right] dv$$

$$= \delta\int_V \frac{1}{2\mu_o\mu_r}(\nabla\times A) \cdot (\nabla\times A)\, dv \qquad (A1.6)$$

Equation A1.2 becomes,

$$\delta \int_V \left[\frac{1}{2\mu_o\mu_r}\left(\nabla\times\underline{A}\right).\left(\nabla\times\underline{A}\right) - JA\right) dv = 0 \qquad (A1.7)$$

which yields the functional,

$$I = \int_V \left[\frac{1}{2\mu_o\mu_r}\left(\nabla\times\underline{A}\right)\cdot\left(\nabla\times\underline{A}\right) - JA\right] dv \qquad (A1.8)$$

The first term in A1.8, is the stored energy in the linear magnetic material W, and is given by equation 1.11. For a non-linear magnetic material W is given by equation 1.10, and the general expression for the energy functional is given by,

$$I = \int_V (W - JA)\, dv \qquad (A1.9)$$

And for axially symmetric problems,

$$I = 2\pi \iint (W-JA)\, r\, dz\, dr \qquad (A1.10)$$

which is the functional 1.9 .

APPENDIX 2

Proof that the minimisation of the functional 1.9, is equivalent to the solution of the Poisson's equation 1.1.

$$\frac{\partial}{\partial z}\left[\frac{1}{\mu_o\mu_r}\left(\frac{\partial A}{\partial z}\right)\right] + \frac{\partial}{\partial r}\left[\frac{1}{\mu_o\mu_r}\left(\frac{\partial A}{\partial r} + \frac{A}{r}\right) + J = 0\right. \quad (1.1)$$

$$I = 2\pi\iint_S \left(W - JA\right) r \, dz \, dr \quad (1.9)$$

The proof can be carried out by deriving 1.1 from 1.9 through the Euler equations of 1.9, as follows:

Assume I has the form,

$$I = \iint_S f(z,r,A,A_z',A_r')\,dz\,dr \quad (A2.1)$$

where, $A_z' = \frac{\partial A}{\partial z}$ and $A_r' = \frac{\partial A}{\partial r}$

The Euler equation of A2.1 is,

$$\frac{\partial}{\partial z}\left(\frac{\partial f}{\partial A_z'}\right) + \frac{\partial}{\partial r}\left(\frac{\partial f}{\partial A_r'}\right) - \frac{\partial f}{\partial A} = 0 \quad (A2.2)$$

Substituting for f from 1.9 in A2.2, we have,

$$f = (W-JA)\, r \cdot 2\pi \quad (A2.3)$$

$$\frac{\partial}{\partial z}\left[\frac{\partial}{\partial A_z'}(W - JA)r\right] + \frac{\partial}{\partial r}\left[\frac{\partial}{\partial A_r'}(W - JA)r\right] - \frac{\partial}{\partial A}\left[(W-JA)r\right] = 0$$

$$\frac{\partial}{\partial z}\left[r\frac{\partial}{\partial B}(W)\frac{\partial B}{\partial A_z'} - rJ\frac{\partial A}{\partial A_z'}\right] + \frac{\partial}{\partial r}\left[r\frac{\partial}{\partial B}(W)\frac{\partial B}{\partial A_r'} - rJ\frac{\partial A}{\partial A_r'}\right] - r\frac{\partial}{\partial B}(W)\frac{\partial B}{\partial A} + rJ = 0 \quad (A2.4)$$

substituting for $W = \int_0^B \frac{B}{\mu_o\mu_r}\,dB$,

$$\frac{\partial}{\partial z}\left[r\frac{B}{\mu_0\mu_r}\frac{\partial B}{\partial A'_z}\right]+\frac{\partial}{\partial r}\left[r\frac{B}{\mu_0\mu_r}\frac{\partial B}{\partial A'_r}\right]-r\frac{B}{\mu_0\mu_r}\frac{\partial B}{\partial A}+rJ=0 \qquad (A2.5)$$

B is given by,

$$B=\sqrt{B_z^2+B_r^2}=\sqrt{(A'_r+\frac{A}{r})^2+A_z'^2} \qquad (A2.6)$$

and from A2.6 we deduce the following relations,

$$\begin{aligned} B\frac{\partial B}{\partial A'_z} &= A'_z = \frac{\partial A}{\partial z} \\ B\frac{\partial B}{\partial A'_r} &= A'_r+\frac{A}{r} = \frac{\partial A}{\partial r}+\frac{A}{r} \\ B\frac{\partial B}{\partial A} &= \frac{1}{r}\left(A'_r+\frac{A}{r}\right)=\frac{1}{r}\left(\frac{\partial A}{\partial r}+\frac{A}{r}\right) \end{aligned} \qquad (A2.7)$$

and A2.5 becomes,

$$\frac{\partial}{\partial z}\left[r\frac{1}{\mu_0\mu_r}\left(\frac{\partial A}{\partial z}\right)\right]+\frac{\partial}{\partial r}\left[r\frac{1}{\mu_0\mu_r}\left(\frac{\partial A}{\partial r}+\frac{A}{r}\right)\right]-\frac{1}{\mu_0\mu_r}\left(\frac{\partial A}{\partial r}+\frac{A}{r}\right)+rJ=0$$

$$r\frac{\partial}{\partial z}\left[\frac{1}{\mu_0\mu_r}\left(\frac{\partial A}{\partial z}\right)\right]+r\frac{\partial}{\partial r}\left[\frac{1}{\mu_0\mu_r}\left(\frac{\partial A}{\partial r}+\frac{A}{r}\right)\right]+\frac{1}{\mu_0\mu_r}\left(\frac{\partial A}{\partial r}+\frac{A}{r}\right)-\frac{1}{\mu_0\mu_r}\left(\frac{\partial A}{\partial r}+\frac{A}{r}\right)+ \\ +rJ=0$$

$$\frac{\partial}{\partial z}\left[\frac{1}{\mu_0\mu_r}\left(\frac{\partial A}{\partial z}\right)\right]+\frac{\partial}{\partial r}\left[\frac{1}{\mu_0\mu_r}\left(\frac{\partial A}{\partial r}+\frac{A}{r}\right)\right]+J=0$$

which is the Poisson's equation 1.1.

APPENDIX 3

DERIVATION OF NODAL EQUATION FOR VPLIN PROGRAM

For a linear magnetic material, the Poisson's equation 1.1, becomes,

$$\frac{\partial^2 A}{\partial z^2}+\frac{\partial^2 A}{\partial r^2}+\frac{\partial}{\partial r}\left(\frac{A}{r}\right)+\mu_0\mu_r J=0 \qquad (A3.1)$$

The solution of A3.1 is equivalent to the minimisation of the energy functional,

$$\begin{aligned} I &= 2\pi\iint_{\substack{\text{Total}\\\text{area}}}\left[\frac{B^2}{2\mu_0\mu_r}-JA\right] r\,dz\,dr \\ &= 2\pi\iint_{\substack{\text{Total}\\\text{area}}}\left[\frac{1}{2\mu_0\mu_r}(\text{curl}\,\underline{A})\cdot(\text{curl}\,\underline{A})-JA\right] r\,dz\,dr \\ &= 2\pi\iint_{\substack{\text{Total}\\\text{area}}}\left\{\frac{1}{2\mu_0\mu_r}\left[\left(\frac{\partial A}{\partial z}\right)^2+\left(\frac{\partial A}{\partial r}+\frac{A}{r}\right)^2\right]-JA\right\} r\,dz\,dr \end{aligned} \qquad (A3.2)$$

Contribution to the functional from a triangular finite element:

Assume a triangular finite element as shown in Figure A3.1, with vector potentials $A_1(z_1,r_1)$, $A_2(z_2,r_2)$ and $A_3(z_3,r_3)$ at its vertices. The contribution to the functional A3.2, from this element is given by,

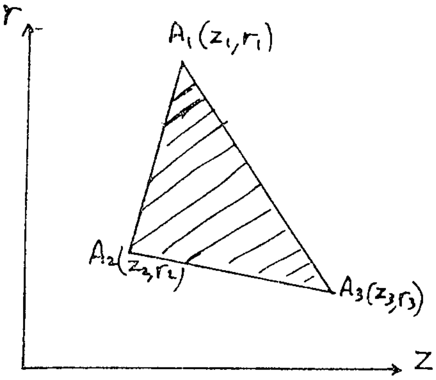

Figure A3.1: Triangular finite element.

$$\Delta I = 2\pi\iint_{\text{Triangle}}\left\{\frac{1}{2\mu_0\mu_r}\left[\left(\frac{\partial A}{\partial z}\right)^2+\left(\frac{\partial A}{\partial r}+\frac{A}{r}\right)^2\right]-JA\right\} r\,dz\,dr \qquad (A3.3)$$

Assume a linear variation of the vector potential A over each element, given by,

$$A = f + gz + hr \qquad (A3.4)$$

where f, g and h are constants over each element. The matrix equation for the vertices,

$$\begin{Bmatrix} A_1 \\ A_2 \\ A_3 \end{Bmatrix} = \begin{bmatrix} 1 & z_1 & r_1 \\ 1 & z_2 & r_2 \\ 1 & z_3 & r_3 \end{bmatrix} \begin{Bmatrix} f \\ g \\ h \end{Bmatrix} \qquad (A3.5)$$

From A3.4 we get,

$$\frac{\partial A}{\partial z} = g, \qquad \frac{\partial A}{\partial r} = h \qquad (A3.6)$$

Hence, A3.3 becomes,

$$\Delta I = 2\pi \iint_{area} \left\{ \frac{1}{2\mu_0\mu_r} \left[g^2 + \left(h + \frac{A}{r}\right)^2 - JA \right\} r \, dz \, dr\right.$$

$$\simeq 2\pi \left\{ \frac{1}{2\mu_0\mu_r} \left[g^2 + \left(h + \frac{\bar{A}}{\bar{r}}\right)^2 \right] - J\bar{A} \right\} \bar{r} \text{ Area} \qquad (A3.7)$$

with, $\bar{r} = (r_1 + r_2 + r_3)/3$

$\bar{A} = (A_1 + A_2 + A_3)/3 \qquad (A3.8)$

Area = area of triangle.

solving A3.6 for g and h we have,

$$g = \frac{\begin{vmatrix} 1 & A_1 & r_1 \\ 1 & A_2 & r_2 \\ 1 & A_3 & r_3 \end{vmatrix}}{\begin{vmatrix} 1 & z_1 & r_1 \\ 1 & z_2 & r_2 \\ 1 & z_3 & r_3 \end{vmatrix}}, \qquad h = \frac{\begin{vmatrix} 1 & z_1 & A_1 \\ 1 & z_2 & A_2 \\ 1 & z_3 & A_3 \end{vmatrix}}{\begin{vmatrix} 1 & z_1 & r_1 \\ 1 & z_2 & r_2 \\ 1 & z_3 & r_3 \end{vmatrix}}$$

$$g = \frac{A_1(r_2-r_3) + A_2(r_3-r_1) + A_3(r_1-r_2)}{2\ \text{Area}}$$

$$h = \frac{A_1(z_3-z_2) + A_2(z_1-z_3) + A_3(z_2-z_1)}{2\ \text{Area}}$$

$$g = \frac{b_1A_1 + b_2A_2 + b_3A_3}{2\ \text{Area}} \qquad (A3.9)$$

$$h = \frac{c_1A_1 + c_2A_2 + c_3A_3}{2\ \text{Area}} \qquad (A3.10)$$

where,

$$\begin{aligned} b_1&=r_2-r_3\ , & c_1&=z_3-z_2 \\ b_2&=r_3-r_1\ , & c_2&=z_1-z_3 \\ b_3&=r_1-r_2\ , & c_3&=z_2-z_1 \\ \text{Area} &= \tfrac{1}{2}(b_1c_2-b_2c_1) \end{aligned} \qquad (A3.11)$$

Substituting for g and h from equations A3.9 and 10, A3.7 yields,

$$\Delta I = \frac{\pi \bar{r}}{4\mu_o\mu_r\text{Area}} \quad (b_1A_1+b_2A_2+b_3A_3)^2 + (d_1A_1+d_2A_2+d_3A_3)^2 \ -$$

$$- \ \frac{2\pi}{3}\ \bar{r}\ \text{Area}\ J(A_1+A_2+A_3) \qquad (A3.12)$$

$$\text{where,}\quad \begin{aligned} d_1 &= c_1 + \frac{2\ \text{Area}}{3\bar{r}} \\ d_2 &= c_2 + \frac{2\ \text{Area}}{3\bar{r}} \\ d_3 &= c_3 + \frac{2\ \text{Area}}{3\bar{r}} \end{aligned} \qquad (A3.13)$$

To minimize the functional A3.12, the derivative of ΔI with respect to A_i must vanish, i.e.,

$$\frac{\partial \Delta I}{\partial A_i} = 0 \qquad (A3.14)$$

At the three vertices, we have,

$$\begin{aligned}\frac{\partial \Delta I}{\partial A_1} &= \frac{\pi \bar{r}}{2\mu_0 \mu_r \cdot Area}\left[b_1(b_1A_1+b_2A_2+b_3A_3) + d_1(d_1A_1+d_2A_2+d_3A_3)\right] - \\ &\quad - \frac{2\pi}{3}\bar{r} \cdot Area \cdot J\end{aligned}$$

$$\begin{aligned}\frac{\partial \Delta I}{\partial A_2} &= \frac{\pi \bar{r}}{2\mu_0 \mu_r \cdot Area}\left[b_2(b_1A_1+b_2A_2+b_3A_3) + d_2(d_1A_1+d_2A_2+d_3A_3)\right] - \\ &\quad - \frac{2\pi}{3}\bar{r} \cdot Area \cdot J\end{aligned} \qquad (A3.15)$$

$$\begin{aligned}\frac{\partial \Delta I}{\partial A_3} &= \frac{\pi \bar{r}}{2\mu_0 \mu_r Area}\left[b_3(b_1A_1+b_2A_2+b_3A_3) + d_3(d_1A_1+d_2A_2+d_3A_3)\right\} - \\ &\quad - \frac{2\pi}{3}\bar{r} \cdot Area \cdot J\end{aligned}$$

and in matrix form, A3.15 becomes,

$$\left\{\frac{\partial \Delta I}{\partial A_i}\right\} = \left[D_{ij}\right] \cdot \left\{A_i\right\} - \left\{Q_i\right\}, \quad i=1,2,3; \; j=1,2,3 \qquad (A3.16)$$

where matrix elements D_{ij} and Q_i are given by,

$$\begin{aligned} D_{ij} &= \frac{\pi \bar{r}}{2\mu_0 \mu_r Area}(b_i b_j + d_i d_j) \\ Q_i &= \frac{2\pi}{3}\bar{r}.Area.J \end{aligned} \qquad (A3.17)$$

Because of symmetry, $\left[D_{ij}\right]$ requires the calculation of 6 elements,

$$\left[D_{ij}\right] = \begin{bmatrix} D_{11} & D_{12} & D_{13} \\ D_{12} & D_{22} & D_{23} \\ D_{13} & D_{23} & D_{33} \end{bmatrix} \qquad (A3.18)$$

<u>The finite element equations</u>:

Figure A3.2 represents a general node o, in contact with twelve finite element triangles. A nodal equation is obtained at point o where the value of the vector potential A_o is affected by the eight neigbouring vector potentials at the other vertices of the twelve triangles in contact. For the numbering of the vector potential values A's we follow two systems; local numbering and global numbering. For a certain triangle, the local numbering is 1, 2 and 3. The convention here is as shown in Figure A3.3. Start from a vertex of the triangle and call it local A_1, the other vertex of the triangle on the opposite corner of the quadrilateral is A_3. The vertex in the way from A_1 to A_3, anti-clockwise, is A_2. The global numbering of the vector potentials over the whole finite element grid is as shown

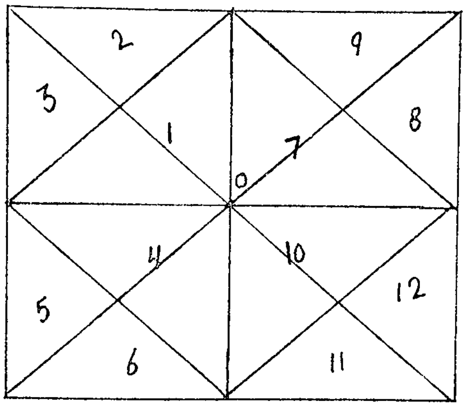

Figure A3.2: A node o in contact with twelve triangular finite elements.

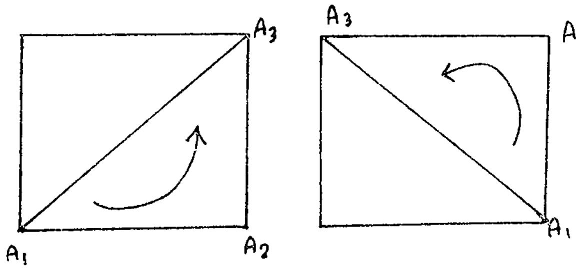

Figure A3.3: Local numbering of vector potential values for each finite element.

in Figure A3.4, which takes the values 1, 2, 3, ... , I , I+1, ..., IJ where I is the number of the radial nodes and J is the number of axial nodes. So, at node I+2 we get a nine-point equation in terms of the vector potentials A_1, A_2, A_3, A_{I+1}, A_{I+2}, A_{I+3}, A_{2I+1}, A_{2I+2} and A_{2I+3}.

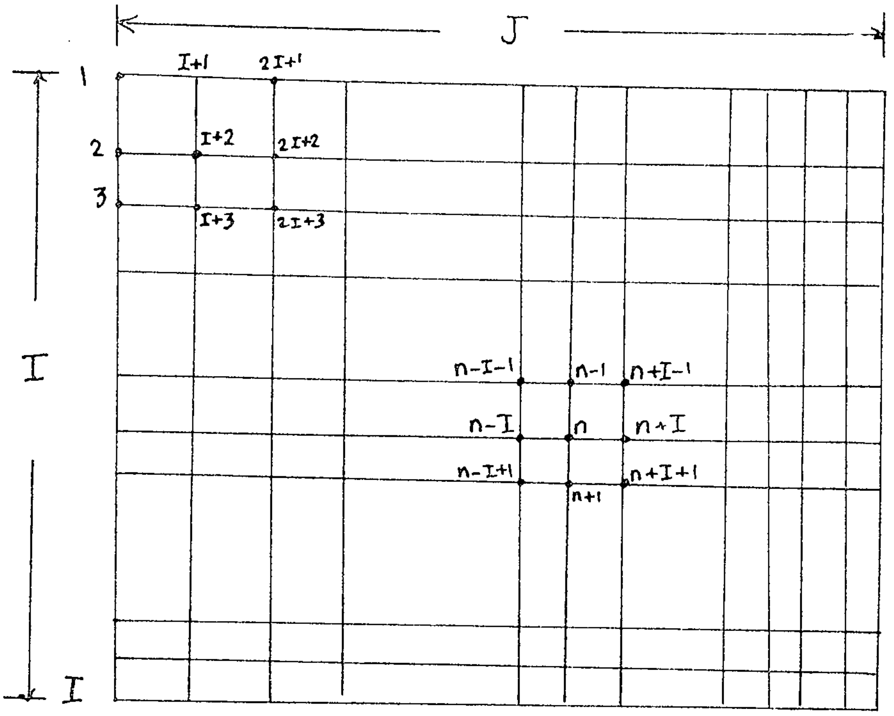

Figure A3.4: Global numbering of the vector potentials at the nodes of a finite element grid.

For a grid of I radial nodes and J axial nodes, the number of equations N_{eq} is given by,

$$\begin{aligned} N_{eq} &= (I-2).(J-2) && \text{for asymmetrical problems,} \\ &= (I-2).(J-1) && \text{for symmetrical problems.} \end{aligned} \qquad (A3.19)$$

To find the coefficients of the nodal equations, assume a general global node n, Figure A3.4. The nodal equation at n is expressed in terms of the vector potentials with global numbers n-I-1, n-I, n-I+1, n-1, n, n+1, n+I-1, n+I and n+I+1. The contribution to the functional A3.12 from the twelve triangles in contact is given by,

$$\Delta I = (\Delta I)_{T_1} + (\Delta I)_{T_2} + (\Delta I)_{T_3} + \dots \dots + (\Delta I)_{T_{12}} \qquad (A3.20)$$

For the functional to be minimised,

$$\left(\frac{\partial \Delta I}{\partial A_n}\right) = \left(\frac{\partial \Delta I}{\partial A_n}\right)_{T_1} + \left(\frac{\partial \Delta I}{\partial A_n}\right)_{T_2} + \dots\dots + \left(\frac{\partial \Delta I}{\partial A_n}\right)_{T_{12}} \qquad (A3.21)$$

where A_n is the vector potential at node n expressed in global numbering. Note that n in global nubering becomes local 2 for T_1, 1 for T_2, 3 for T_3, 1 for T_4, ... and 3 for T_{12}. hence in local numbering equation A3.21 becomes,

$$\frac{\partial \Delta I}{\partial A_n} = \left(\frac{\partial \Delta I}{\partial A_2}\right)_{T_1} + \left(\frac{\partial \Delta I}{\partial A_1}\right)_{T_2} + \left(\frac{\partial \Delta I}{\partial A_3}\right)_{T_3} + \left(\frac{\partial \Delta I}{\partial A_2}\right)_{T_4} + \dots\dots + \left(\frac{\partial \Delta I}{\partial A_3}\right)_{T_{12}} \qquad (A3.22)$$

From equations A3.17 and 18, the terms in equation A3.22, can be expressed in local then global numbering as follows,

$$\begin{aligned}
\left(\frac{\partial \Delta I}{\partial A_2}\right)_{T_1} &= D_{12} A_1 + D_{22} A_2 + D_{23} A_3 - Q_1 \qquad \text{(local)} \\
&= D_{12} A_{n-I-1} + D_{22} A_n + D_{23} A_{n-1} - Q_1 \qquad \text{(global)} \\
\left(\frac{\partial \Delta I}{\partial A_1}\right)_{T_2} &= D_{11} A_1 + D_{12} A_2 + D_{13} A_3 - Q_2 \\
&= D_{11} A_n + D_{12} A_{n-1} + D_{13} A_{n-I-1} - Q_2 \\
\left(\frac{\partial \Delta I}{\partial A_3}\right)_{T_3} &= D_{13} A_1 + D_{23} A_2 + D_{33} A_3 - Q_3 \\
&= D_{13} A_{n-I-1} + D_{23} A_{n-I} + D_{33} A_n - Q_3 \\
\left(\frac{\partial \Delta I}{\partial A_2}\right)_{T_4} &= D_{12} A_1 + D_{22} A_2 + D_{23} A_3 - Q_4 \\
&= D_{12} A_{n+1} + D_{22} A_n + D_{23} A_{n-I} - Q_4 \\
\left(\frac{\partial \Delta I}{\partial A_1}\right)_{T_5} &= D_{11} A_1 + D_{12} A_2 + D_{13} A_3 - Q_5 \\
&= D_{11} A_n + D_{12} A_{n-I} + D_{13} A_{n-I+1} - Q_5 \\
\left(\frac{\partial \Delta I}{\partial A_3}\right)_{T_6} &= D_{13} A_1 + D_{23} A_2 + D_{33} A_3 - Q_6 \\
&= D_{13} A_{n-I+1} + D_{23} A_{n+1} + D_{33} A_n - Q_6
\end{aligned} \qquad (A3.23)$$

$$\begin{aligned}
\left(\frac{\partial \Delta I}{\partial A_2}\right)_{T_7} &= D_{12}A_1 + D_{22}A_2 + D_{23}A_3 - Q_7 \\
&= D_{12}A_{n-1} + D_{22}A_n + D_{23}A_{n+I} - Q_7 \\
\left(\frac{\partial \Delta I}{\partial A_1}\right)_{T_8} &= D_{11}A_1 + D_{12}A_2 + D_{13}A_3 - Q_8 \\
&= D_{11}A_n + D_{12}A_{n+I} + D_{13}A_{n+I-1} - Q_8 \\
\left(\frac{\partial \Delta I}{\partial A_3}\right)_{T_9} &= D_{13}A_1 + D_{23}A_2 + D_{33}A_3 - Q_9 \\
&= D_{13}A_{n+I-1} + D_{23}A_{n-1} + D_{33}A_n - Q_9 \qquad \text{(A3.23)} \\
\left(\frac{\partial \Delta I}{\partial A_2}\right)_{T_{10}} &= D_{12}A_1 + D_{22}A_2 + D_{23}A_3 - Q_{10} \\
&= D_{12}A_{n+I} + D_{22}A_n + D_{23}A_{n+1} - Q_{10} \\
\left(\frac{\partial \Delta I}{\partial A_1}\right)_{T_{11}} &= D_{11}A_1 + D_{12}A_2 + D_{13}A_3 - Q_{11} \\
&= D_{11}A_n + D_{12}A_{n+1} + D_{13}A_{n+I+1} - Q_{11} \\
\left(\frac{\partial \Delta I}{\partial A_3}\right)_{T_{12}} &= D_{13}A_1 + D_{23}A_2 + D_{33}A_3 - Q_{12} \\
&= D_{13}A_{n+I+1} + D_{23}A_{n+I} + D_{33}A_n - Q_{12}
\end{aligned}$$

From equations A3.23 and 22 we get a nine-point equation for the node n, given by,

$$\begin{aligned}
P_1A_{n-I-1} + P_2A_{n-I} + P_3A_{n-I+1} + P_4A_{n-1} + P_5A_n + P_6A_{n+1} + p_7A_{n+I-1} + P_8A_{n+I} + \\
+ P_9A_{n+I+1} = C_n \qquad \text{(A3.24)}
\end{aligned}$$

where,

$$\begin{aligned}
P_1 &= (D_{13})_{T_2} + (D_{13})_{T_3} \\
P_2 &= (D_{12})_{T_1} + (D_{23})_{T_3} + (D_{23})_{T_4} + (D_{12})_{T_5} \\
P_3 &= (D_{13})_{T_5} + (D_{13})_{T_6} \\
P_4 &= (D_{23})_{T_1} + (D_{12})_{T_2} + (D_{12})_{T_7} + (D_{23})_{T_9} \\
P_5 &= (D_{22})_{T_1} + (D_{11})_{T_2} + (D_{33})_{T_3} + (D_{22})_{T_4} + \cdots\cdots + (D_{33})_{T_{12}} \qquad \text{(A3.25)} \\
P_6 &= (D_{12})_{T_4} + (D_{23})_{T_6} + (D_{23})_{T_{10}} + (D_{12})_{T_{11}} \\
P_7 &= (D_{13})_{T_8} + (D_{13})_{T_9} \\
P_8 &= (D_{23})_{T_7} + (D_{12})_{T_8} + (D_{12})_{T_{10}} + (D_{23})_{T_{12}} \\
P_9 &= (D_{13})_{T_{11}} + (D_{13})_{T_{12}} \\
C_n &= Q_1 + Q_2 + Q_3 + Q_4 + Q_5 + Q_6 + Q_7 + Q_8 + Q_9 + Q_{10} + Q_{11} + Q_{12}
\end{aligned}$$

The nodal equations can be expressed in matrix form as,

$$\updownarrow N_{eq}\;\overset{\xleftrightarrow{\;N_{eq}\;}}{\left[\quad P \quad\right]}\begin{Bmatrix}A_{I+2}\\ \vdots\\ A_{2I-1}\\ A_{2I+1}\\ \vdots\\ A_{IJ-1+\ell}\end{Bmatrix}=\begin{Bmatrix}C_{I+2}\\ \vdots\\ C_{2I-1}\\ C_{2I+1}\\ \vdots\\ C_{IJ-1+\ell}\end{Bmatrix} \tag{A3.26}$$

where $\ell=0$ for asymmetrical problems and $\ell=I$ for symmetrical problems.

Since each nodal equation is expressed in terms of the vector potential at the node and the eight neigbouring vector potential values, the matrix $\left[P\right]$ is sparse. The resulted matrix $\left[P\right]$ also has the property of a banded matrix as shown in Figure A3.5, with half-band width equal I. The matrix also, has the other important property of symmetry about the diagonal, and hence only the coefficients of the banded matrix in the upper triangle of the matrix need to be stored. The array of coefficients will be of size $P(N_{eq},I)$. The matrix equation is solved by Gaussian elimination, a subroutine for the solution is given in Appendix 4.

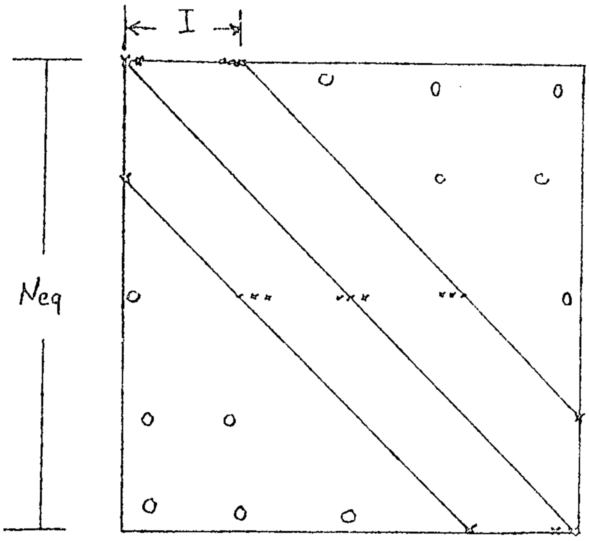

Figure A3.5: Banded matrix for the coefficients of nodal equations.

APPENDIX 4

SUBROUTINE FOR EQUATION SOLVING BY GAUSSIAN ELIMINATION

```
      SUBROUTINE EQNS (C,IT,IS,P,I1,IM,IJM)
      DIMENSION C(IJM),P(IJM,IM)

      NC=I1
      IS1=IS-1
      DO 70 NT=1,IS1
      IF (NT.GT.IT) NC=IS-NT+1
      DO 71 I=2,NC
      IC=NT+I-1
      RC=P(NT,I)/P(NT,1)
      C(IC)=C(IC)-RC*C(NT)                  Gaussian
      II11=I1-I+1                          elimination
      DO 72 J=1,II11
      P(IC,J)=P(IC,J)-RC*P(NT,I+J-1)
   72 CONTINUE
   71 CONTINUE
   70 CONTINUE
      C(IS)=C(IS)/P(IS,1)
      IS1=IS-1
      DO 80 I=1,IS1
      II=IS-I
      NC=I1
      IF (II.GT.IT) NC=IS-II+1                 Back
      S=0.                                 substitution
      DO 81 J=2,NC
      JJ=NC+2-J
      S=S+P(II,JJ)*C(II+JJ-1)
   81 CONTINUE
      C(II)=(C(II)-S)/P(II,1)
   80 CONTINUE
      RETURN
      END
```

Variables:

I1 Number of radial nodes in the finite element grid

IS Number of equations to be solved

P Array which holds the lefthand side coefficients of the equations

C Array which holds the righthand side coefficients of the equations

Appendix 5

DERIVATION OF NODAL EQUATIONS FOR THE VPSAT PROGRAM

For non-linear magnetic material the Poisson's equation is given by equation 1.1 as,

$$\frac{\partial}{\partial z}\left[\frac{1}{\mu_o\mu_r}\frac{\partial A}{\partial z}\right]+\frac{\partial}{\partial r}\left[\frac{1}{\mu_o\mu_r}\left(\frac{\partial A}{\partial r}+\frac{A}{r}\right)\right]+J=0 \qquad (A5.1)$$

The solution of equation A5.1 is equivalent to the minimisation of the energy functional,

$$I = 2\pi\iint_{\substack{\text{Total}\\\text{area}}}(W - JA)\ r\,dz\,dr \qquad (A5.2)$$

$$I = 2\pi\iint_{\substack{\text{Total}\\\text{area}}}\left[\int_0^B\frac{B}{\mu_o\mu_r}dB - JA\right] r\,dz\,dr \qquad (A5.3)$$

The contribution to the functional from a triangular finite element:

Assume a triangular finite element with the vector potential values $A_1(z_1,r_1)$, $A_2(z_2,r_2)$ and $A_3(z_3,r_3)$ at its vertices as shown in Figure A5.1. The contribution to the Functional A5.3 from this triangular finite element is given by,

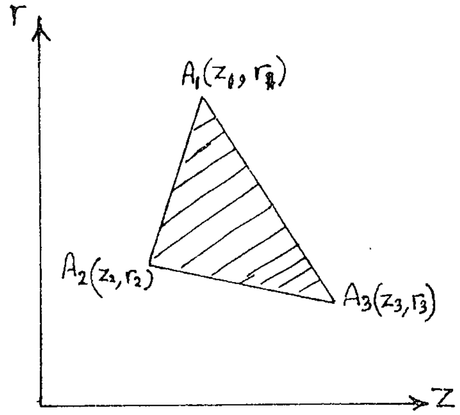

Figure A5.1: Triangular finite element.

$$\Delta I = 2\pi\iint_{\text{Triangle}}\left[\int_0^B\frac{B}{\mu_o\mu_r}dB - JA\right] r\,dz\,dr$$

$$\Delta I \simeq 2\pi\left[\int_0^B\frac{B}{\mu_o\mu_r}dB - J\bar{A}\right]\bar{r}\,dz\,dr \qquad (A5.4)$$

For the functional to be minimised, the derivative of I with respect to the vector potential values at the vertices should vanish,

$$\frac{\partial \Delta I}{\partial A_i} = 2\pi \left[\frac{\partial}{\partial A_i}\int_0^B \frac{B}{\mu_0 \mu_r}\, dB - \frac{\partial}{\partial A_i}(J\bar{A})\right] \bar{r}\,.\,\text{Area}$$

$$= 2\pi \;\left(\frac{B}{\mu_o \mu_r}\,\frac{\partial B}{\partial A_i} - \tfrac{1}{3}J\right) \bar{r}\,.\,\text{Area}$$

$$= 2\pi r \;\text{Area}\; \left(\frac{B}{\mu_o \mu_r}\,\frac{\partial B}{\partial A_i} - \frac{1}{3}J\right) = 0 \qquad \text{(A5.5)}$$

The flux density at each triangle is calculated using equations 1.10 and 1.12 at the centroid of the triangle,

$$B_r = -\frac{\partial A}{\partial z}\,, \qquad B_z = \frac{\partial A}{\partial r} + \frac{\bar{A}}{\bar{r}} \qquad \text{(A5.6)}$$

Assume linear variation of A across the triangle, given by,

$$A = f + gz + hr \qquad \text{(A5.7)}$$

where f, g and h are constants over each triangle. At the vertices of the triangle we have the matrix equation,

$$\begin{Bmatrix} A_1 \\ A_2 \\ A_3 \end{Bmatrix} = \begin{bmatrix} 1 & z_1 & r_1 \\ 1 & z_2 & r_2 \\ 1 & z_3 & r_3 \end{bmatrix} \begin{Bmatrix} f \\ g \\ h \end{Bmatrix} \qquad \text{(A5.8)}$$

As in Appendix 4(equations A4.9-11),

$$g = \frac{b_1 A_1 + b_2 A_2 + b_3 A_3}{\text{Det}} \qquad \text{(A5.9)}$$

$$h = \frac{c_1 A_1 + c_2 A_2 + c_3 A_3}{\text{Det}} \qquad \text{(A5.10)}$$

$$\text{where Det} = 2.\text{Area} = b_1 c_2 - b_2 c_1 \qquad \text{(A5.11)}$$

$$b_1=r_2-r_3\,,\qquad c_1=z_3-z_2$$
$$b_2=r_3-r_1\,,\qquad c_2=z_1-z_3 \qquad\qquad (A5.12)$$
$$b_3=r_1-r_2\,,\qquad c_3=z_2-z_1$$

From equations A5.6 and 7 we have,

$$B_r = -g = -\frac{b_1A_1 + b_2A_2 + b_3A_3}{\text{Det}} \qquad (A5.13)$$

$$B_z = h + \frac{\bar{A}}{\bar{r}} = \frac{c_1A_1 + c_2A_2 + c_3A_3}{\text{Det}} + \frac{\bar{A}}{\bar{r}} \qquad (A5.14)$$

$$B = \sqrt{B_r^2 + B_z^2} \qquad (A5.15)$$

$$\frac{\partial B}{\partial A_i} = \tfrac{1}{2}(B_r^2+B_z^2)^{-\frac{1}{2}}.(2B_r\frac{\partial B_r}{\partial A_i}+2B_z\frac{\partial B_z}{\partial A_i})$$

$$= \frac{1}{B}\left(\quad \frac{\partial B_r}{\partial A_i} + B_z\frac{\partial B_z}{\partial A_i}\right)$$

$$= \frac{1}{B}\left[B_r\cdot\left(-\frac{b_i}{\text{Det}}\right) + B_z\left(\frac{c_i}{\text{Det}} + \frac{1}{3\bar{r}}\right)\right] \qquad (A5.16)$$

Hence equation A5.5, yields,

$$\frac{\partial \Delta I}{\partial A_i} = \pi\bar{r}\,\text{Det}\left\{\frac{1}{\mu_0\mu_r}\left[\frac{-b_i\,B_r}{\text{Det}} + \frac{B_z}{\text{Det}}\left(c_i + \frac{\text{Det}}{3\bar{r}}\right)\right] - \frac{1}{3}J\right\}$$

$$= \pi\bar{r}\,\text{Det}\,\frac{1}{\mu_0\mu_r}\left[\frac{-b_iB_r}{\text{Det}} + \frac{\left(c_i + \frac{\text{Det}}{3\bar{r}}\right)}{\text{Det}}B_z\right] - \frac{\pi\bar{r}\,\text{Det}}{3}J = 0 \qquad (A5.17)$$

For the three vertices of the triangle we get,

$$\left\{\frac{\partial \Delta I}{\partial A_i}\right\} = \left[D_{ij}\right]\left\{A_i\right\} - \left\{Q_i\right\} \qquad (A5.18)$$

where the general elements of $\left[D_{ij}\right]$ and $\left\{Q_i\right\}$ are given by,

$$D_{ij} = \frac{\pi \bar{r}\, Det}{\mu_o \mu_r}\left[\frac{b_i b_j}{Det^2} + \frac{\left(c_i + \frac{Det}{3\bar{r}}\right)\left(c_j + \frac{Det}{3\bar{r}}\right)}{Det^2}\right]$$

$$Q_i = \frac{\pi \bar{r}\, Det}{3} \cdot J \qquad , \; i=1,2,3, \; j=1,2,3. \qquad \text{(A5.19)}$$

The finite element equations:

For a general node m,

$$\frac{\partial I}{\partial A_m} = \sum_{k=1}^{12}\left(\frac{\partial \Delta I}{\partial A_m}\right)_{T_k}$$

$$= \left(\frac{\partial \Delta I}{\partial A_2}\right)_{T_1} + \left(\frac{\partial \Delta I}{\partial A_1}\right)_{T_2} + \left(\frac{\partial \Delta I}{\partial A_3}\right)_{T_3} + \left(\frac{\partial \Delta I}{\partial A_2}\right)_{T_4} + \cdots + \qquad \text{(A5.20)}$$

$$+ \left(\frac{\partial \Delta I}{\partial A_3}\right)_{T_{12}}$$

where $\left(\frac{\partial \Delta I}{\partial A_m}\right)_{T_k}$, k=1, ... ,12 are given as equations A3.23.

A set of nine-point non-linear equations are generated at each node of the finite element grid and of the general form, where m has the values from I+2 to IJ-1+ℓ. ℓ=0 for symmetrical structures and ℓ=I for asymmetrical structures,

$$\frac{\partial I}{\partial A_m} = P_1 A_{m-I-1} + P_2 A_{m-I} + P_3 A_{m-I+1} + P_4 A_{m-1} + P_5 A_m + P_6 A_{m+1} + P_7 A_{m+I-1} +$$

$$+ P_8 A_{m+I} + P_9 A_{m+I+1} - C_m = 0 \qquad \text{(A5.21)}$$

where the P and C coefficients are as given by the equations A3.25.

These non-linear equations are solved by Newton-Raphson iteration, (see Appendix 6), by calculating the matrix equation,

$$\left[J_{nm}\right]\left\{\Delta A_m\right\} = E_m \qquad \text{(A5.22)}$$

with,

$m=I+2, \ldots, 2I-1, 2I+1, \ldots, IJ-1+\ell$

$n=I+2, \ldots, 2I-1, 2I+1, \ldots, IJ-1+\ell$.

where J_{nm} is called the Jacobian matrix of the non-linear equations of general form given in equation A5.21; it is given by,

$$\left[J_{nm}\right] = \begin{bmatrix} \frac{\partial}{\partial A_{I+2}}\left(\frac{\partial I}{\partial A_{I+2}}\right) & \frac{\partial}{\partial A_{I+3}}\left(\frac{\partial I}{\partial A_{I+2}}\right) & \cdots & \frac{\partial}{\partial A_{IJ-1+\ell}}\left(\frac{\partial I}{\partial A_{I+2}}\right) \\ \frac{\partial}{\partial A_{I+2}}\left(\frac{\partial I}{\partial A_{I+3}}\right) & \cdots & & \\ \vdots & & & \\ \frac{\partial}{\partial A_{I+2}}\left(\frac{\partial I}{\partial A_{IJ-1+\ell}}\right) & \cdots & & \frac{\partial}{\partial A_{IJ-1+\ell}}\left(\frac{\partial I}{\partial A_{IJ-1+\ell}}\right) \end{bmatrix} \qquad (A5.23)$$

Each element of this matrix is given by,

$$J_{nm} = \frac{\partial}{\partial A_n}\left(\frac{\partial I}{\partial A_m}\right) \qquad (A5.24)$$

which is to be calculated below, and, $\left\{E_m\right\}$ is the matrix of residuals where the element E_m is given by,

$$E_m = \left(\frac{\partial I}{\partial A_m}\right) \quad \text{calculated at } A_{I+2}, \ \ldots\ A_{IJ-1+\ell} \qquad (A5.25)$$

and to be calculated below. $\left\{\Delta A_m\right\}$ is the matrix of variations in the vector potentials. The element ΔA_m is given by,

$$\Delta A_m = (A_m)^k - (A_m)^{k+1} \qquad (A5.26)$$

i.e. the difference in vector potential at the mth node between two consecutive iterations, k and k+1.

$$\frac{\partial}{\partial A_n}\left(\frac{\partial I}{\partial A_m}\right) = \sum_{k=1}^{12}\left[\frac{\partial}{\partial A_n}\left(\frac{\partial \Delta I}{\partial A_m}\right)\right]_{T_K} \qquad (A5.27)$$

with,

$$\frac{\partial}{\partial A_n}\left(\frac{\partial \Delta I}{\partial A_m}\right) = \frac{\pi\bar{r}}{\mu_o\mu_r\,Det}\left\{\left[b_m b_n + \left(c_m + \frac{Det}{3\bar{r}}\right)\left(c_n + \frac{Det}{3\bar{r}}\right)\right] - \frac{1}{B\mu_r}\frac{\partial\mu_r}{\partial B}\cdot\right.$$
$$\left.\cdot\left[-b_m B_r + \left(c_m + \frac{Det}{3\bar{r}}\right)B_z\right]\left[-b_n B_r + \left(c_n + \frac{Det}{3\bar{r}}\right)B_z\right]\right\} \qquad (A5.28)$$

$$E_m = \left(\frac{\partial I}{\partial A_m}\right) = \sum_{K=1}^{12} \left(\frac{\partial \Delta I}{\partial A_m}\right)_{T_K} \qquad (A5.29)$$

with,

$$\frac{\partial \Delta I}{\partial A_m} = \frac{\pi \bar{r}}{\mu_0 \mu_r} \left[-b_m B_r + \left(c_m + \frac{Det}{3\bar{r}}\right) B_z \right] - \frac{\pi \bar{r}\, Det}{3} J \qquad (A5.30)$$

The matrix equation A5.22 is then solved by Gaussian elimination and a new approximation for the vector potential values is calculated.

$$\left\{A\right\}^{K+1} = \left\{A\right\}^{K} + \left\{\Delta A\right\}^{K} \qquad (A5.31)$$

This process is repeated until the changes $\left\{\Delta A\right\}^{K}$ are within a certain accuracy limit.

APPENDIX 6

NEWTON-RAPHSON ITERATION METHOD FOR SOLVING SIMULTANEOUS EQUATIONS

Consider the two simultaneous equations,

$$P_{11}A_1 + P_{12}A_2 + C_1 = 0 \qquad (A6.1)$$

$$P_{21}A_1 + P_{22}A_2 + C_2 = 0 \qquad (A6.2)$$

The above equations are called linear equations if the coefficients P_{11}, P_{12}, P_{21}, P_{22}, C_1 and C_2 are constants. But if these coefficients depend on the variables A_1 and A_2, the equations are called non-linear. Newton-Raphson iteration method is used for the solution of non-linear simultaneous equations. Here, the method is demonstrated by solving two linear equations,

$$f_1(A_1,A_2) \equiv \quad A_1 + \quad A_2 \quad = 0 \qquad (A6.3)$$

$$f_2(A_1,A_2) \equiv 2A_1 + 3A_2 + 2 = 0 \qquad (A6.4)$$

In these two equations the P coefficients are constant. Assume the first guess of A values $(A_1)^1 = 0$, $(A_2)^1 = 0$. Then we form the matrix equation,

$$\begin{bmatrix} J_{nm} \end{bmatrix} \begin{Bmatrix} \Delta A_m \end{Bmatrix} = \begin{Bmatrix} E_m \end{Bmatrix} \qquad (A6.5)$$

$$\begin{bmatrix} \frac{\partial f_1}{\partial A_1} & \frac{\partial f_1}{\partial A_2} \\ \frac{\partial f_2}{\partial A_1} & \frac{\partial f_2}{\partial A_2} \end{bmatrix} \begin{Bmatrix} \Delta A_1 \\ \Delta A_2 \end{Bmatrix} = \begin{Bmatrix} (f_1)^1 \\ (f_2)^1 \end{Bmatrix} \qquad (A6.6)$$

where f_1 and f_2 are written for $f_1(A_1,A_2)$ and $f_2(A_1,A_2)$ respectively. $(f_1)^1$ and $(f_2)^1$ are the values of f_1 and f_2 at the current values of A_1 and A_2 . Hence,

$$\begin{bmatrix} 1 & 1 \\ 2 & 3 \end{bmatrix} \begin{Bmatrix} \Delta A_1 \\ \Delta A_2 \end{Bmatrix} = \begin{matrix} 0 \\ 2 \end{matrix} \qquad (A6.7)$$

Solving this equation for A_1 and A_2 by elimination we have,

$$\begin{bmatrix} 1 & 1 \\ 0 & 1 \end{bmatrix} \begin{Bmatrix} \Delta A_1 \\ \Delta A_2 \end{Bmatrix} = \begin{Bmatrix} 0 \\ -2 \end{Bmatrix} \qquad (A6.8)$$

$$\begin{aligned} (\Delta A_2)^1 &= -2 \\ (\Delta A_1)^1 &= 2 \end{aligned} \qquad (A6.9)$$

The next values of A will be,

$$\begin{aligned} (A_1)^2 &= (A_1)^1 + (\Delta A_1)^1 = 0 + 2 = 2 \\ (A_2)^2 &= (A_2)^1 + (\Delta A_2)^1 = 0 - 2 = -2 \end{aligned} \qquad (A6.10)$$

Repeat the steps connected with equations A6.6-9, until the values of $\left\{E_m\right\}$ are zeros or when the change in the A values are within a certain accuracy limit.

$$\begin{bmatrix} 1 & 1 \\ 2 & 3 \end{bmatrix} \begin{Bmatrix} \Delta A_1 \\ \Delta A_2 \end{Bmatrix} = \begin{Bmatrix} 0 \\ 0 \end{Bmatrix} \qquad (A6.7a)$$

$$\begin{bmatrix} 1 & 1 \\ 0 & 1 \end{bmatrix} \begin{Bmatrix} \Delta A_1 \\ \Delta A_2 \end{Bmatrix} = \begin{Bmatrix} 0 \\ 0 \end{Bmatrix} \qquad (A6.8a)$$

$$\left(\Delta A_2\right)^2 = 0$$

$$\left(\Delta A_1\right)^2 = 0 \qquad \text{(A6.9a)}$$

In this example the solution is complete from the results of equation A6.8a since $\left\{E_m\right\}$ are zeros. Equations A6.9a shows the variations in A values are zero. The solution is $A_1 = 2$, $A_2 = -2$.

For non-linear equations the same procedure is followed, but the $\left[J_{nm}\right]$ matrix will be different for each step since the P coefficients vary with each iteration. These coefficients need to be calculated after each iteration.

APPENDIX 7

CALCULATION OF THE MAGNETIC FLUX DENSITY FROM THE VECTOR POTENTIAL DISTRIBUTION

The magnetic flux density distribution can be calculated when the vector distribution is known, since,

$$\underline{B} = \text{curl } \underline{A} \qquad (A7.1)$$

where $\underline{B}$ is the flux density and $\underline{A}$ is the magnetic vector potential. For axial symmetric problems with cylindrical coordinates (z, θ, r), the vector potential $\underline{A}$ has only the A_θ component, so

$$\underline{B}(z,r) = \frac{1}{r}\begin{vmatrix} \underline{a}_r & \underline{a}_\theta & \underline{a}_z \\ \frac{\partial}{\partial r} & \frac{\partial}{\partial \theta} & \frac{\partial}{\partial z} \\ 0 & rA_\theta & 0 \end{vmatrix} \qquad (A7.2)$$

where $\underline{a}_r$, $\underline{a}_\theta$ and $\underline{a}_z$ are the unit vectors in the r, θ and z coordinates respectively.

From equation A7.2 we get,

$$\underline{B}(z,r) = \frac{1}{r}\left[\frac{\partial}{\partial r}(rA)\,\underline{a}_z - \frac{\partial}{\partial z}(rA)\,\underline{a}_r\right] \qquad (A7.3)$$

where we put A for A_θ.

And hence $\underline{B}$ has the two components B_z and B_r given by,

$$B_z = \frac{1}{r}\frac{\partial}{\partial r}(rA) = \frac{\partial A}{\partial r} + \frac{A}{r} \qquad (A7.4)$$

$$B_r = -\frac{\partial A}{\partial z} \qquad (A7.5)$$

The magnitude of the flux density, $B(z,r)$, is given by,

$$B(z,r) = \sqrt{B_z^2 + B_r^2} \qquad \text{(A7.6)}$$

Assume the variation of A over each quadrilateral, given by,

$$A = f + gz + hr + izr \qquad \text{(A7.7)}$$

where f, g, h and i are constants over each quadrilateral. Hence the flux density components at the centroid of the quadrilateral,

$$B_z = h + iz + \frac{\overline{A}}{\overline{r}} \qquad \text{(A7.8)}$$

$$B_r = -g - ir \qquad \text{(A7.9)}$$

where $\overline{A}$ and $\overline{r}$ are the vector potential and the radial distance of the centroid of the quadrilateral.

The object now is to find the values of g, h and i as follows. Figure A7.1 represents a general quadrilateral abcd. e is the centroid of the quadrilateral. Table A7.1 shows the vector potentials and coordinates of the different points in Figure A7.1.

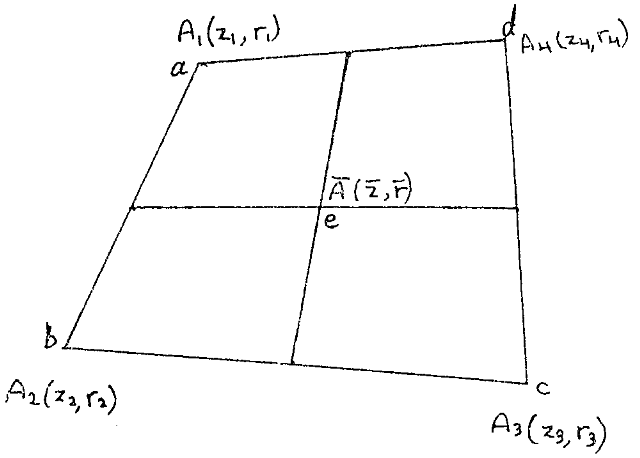

Figure A7.1: A general quadrilateral abcd, the centroid is e. Vector potentials and coordinates of different points.

POINT	VECTOR POTENTIAL	Z COORDINATE	R COORDINATE
a	A_1	z_1	r_1
b	A_2	z_2	r_2
c	A_3	z_3	r_3
d	A_4	z_4	r_4
e	$\overline{A}$	$\overline{z}=(z_1+z_2+z_3+z_4)/4$	$\overline{r}=(r_1+r_2+r_3+r_4)/4$

Table A7.1: Vector potentials and coordinates of different points shown in Figure A7.1.

Substituting for A, z and r in equation A7.7, by the corresponding values at the vertices of the quadrilateral, we get four linear simultaneous equations in f, g, h and i,

$$A_1 = f + gz_1 + hr_1 + iz_1r_1 \quad (A7.10)$$

$$A_2 = f + gz_2 + hr_2 + iz_2r_2 \quad (A7.11)$$

$$A_3 = f + gz_3 + hr_3 + iz_3r_3 \quad (A7.12)$$

$$A_4 = f + gz_4 + hr_4 + iz_4r_4 \quad (A7.13)$$

These equations (A7.10-13) are then solved for f, g, h and i; and $\overline{A}$ at the centre is given by,

$$\overline{A} = f + g\overline{z} + h\overline{r} + i\overline{z}\overline{r} \quad (A7.14)$$

Hence, using equations A7.8 and A7.9, the flux density components B_z and B_r can be found, and B is calculated from equation A7.6.

Calculation of the axial flux density:

In particular the axial flux density can be calculated from vector potential values near the axis. Since the vector potential is a singular function, it can be expressed as a series in odd powers in r,

$$A = c_1 r + c_2 r^3 + c_3 r^5 + \ldots \qquad (A7.15)$$

The axial flux density can be found from equation A7.4 as,

$$B_z(z) = \lim_{r \to 0} \left[\frac{\partial A}{\partial r} + \frac{A}{r} \right] \qquad (A7.16)$$

$$B_z(z) = \lim_{r \to 0} \left[c_1 + 3c_2 r^2 + \ldots + c_1 + c_2 r^2 + \ldots \right]$$

$$= 2c_1 \qquad (A7.17)$$

From two vector potential values A_1 and A_2 at radial distances r_1 and r_2 respectively (Figure A7.2), we have the two simultaneous equations, truncated to two terms,

$$A_1 = c_1 r_1 + c_2 r_1^3 \qquad (A7.18)$$

$$A_2 = c_1 r_2 + c_2 r_2^3 \qquad (A7.19)$$

which when solved for c_1, yield,

$$c_1 = \frac{(A_1 r_2^3 - A_2 r_1^3)}{r_1 r_2^3 - r_2 r_1^3} \qquad (A7.20)$$

Hence, equation A7.17 yields the axial flux density, B(z), at point P,

$$B_z(z) = \frac{2(A_1 r_2^3 - A_2 r_1^3)}{r_1 r_2 (r_2^2 - r_1^2)} \qquad (A7.21)$$

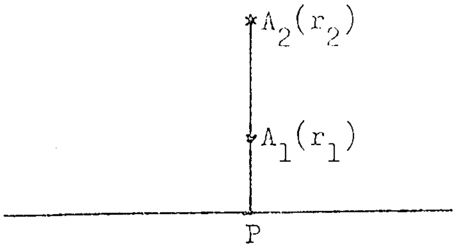

Figure A7.2: Calculation of axial flux density at point P from two near axis vector potential values A_1 and A_2.

APPENDIX 8

Inst. Phys. Conf. Ser. No. 52 © 1980: Chapter 1 53

LIMITATIONS OF THE FINITE ELEMENT METHOD

T Mulvey and H Nasr
Physics Department, The University of Aston in Birmingham B4 7ET (UK)

APPENDIX 9

AN IMPROVED FINITE ELEMENT PROGRAM FOR CALCULATING THE FIELD DISTRIBUTION IN MAGNETIC LENSES

T.Mulvey and H.Nasr

Department of Physics, The University of Aston in Birmingham
Birmingham B4 7ET (UK)

APPENDIX 10

Nuclear Instruments and Methods 000 (1981) NIM W 125
North-Holland Publishing Company

AN IMPROVED FINITE ELEMENT METHOD FOR CALCULATING THE MAGNETIC FIELD DISTRIBUTION IN MAGNET ELECTRON LENSES AND ELECTROMAGNETS

Tom MULVEY and Hamed NASR
Department of Physics, The University of Aston in Birmingham, B4 7ET, UK

REFERENCES

Al-Hilly, S. M. (1980)

Private communication.

Christofides, S. (1980a)

Private communication.

Christofides, S. and Mulvey T. (1980b)

'A HIGH DENSITY SINGLE-POLEPIECE OBJECTIVE LENS'

in: Electron Microscopy 1980, vol.1.

Seventh European Congress on Electron Microscopy. P.70.

Eds. P. Brederoo and G. Boom (Seventh European Congress on Electron Microscopy Foundation, Leiden 1980)

Denegri, G. B., Molinari, G. and Viviani, A. (1976)

'A GENERALIZED FINITE DIFFERENCE METHOD FOR THE COMPUTATION OF ELECTRIC AND MAGNETIC FIELDS'

Proc. COMPUMAG Conference on the Computation of Magnetic fields, Oxford 1976. P.104.

Ed. C. W. Trowbridge (Rutherford Laboratory, Didcot, Oxford 1976)

Glaser, W. (1952)

GRUNDLAGEN DER ELEKTRONENOPTIK

Wien, Springler-Verlag.

Glaser, W. (1956)

'ELEKTRONEN UND IONENOPTIK'

Handbuch der Physik. 33 (1956). P.123.

Hawkes, P. W. (1970)

'ASYMPTOTIC ABERRATION INTEGRALS FOR ROUND LENSES'

Optik. P.213.

Hawkes, P. W. (1972)

ELECTRON OPTICS AND ELECTRON MICROSCOPY

Taylor & Francis Ltd, London.

Hill, R. and Smith, K. C. A. (1980)

'ANALYSIS OF THE SINGLE-POLE LENS BY FINITE ELEMENT COMPUTATION'

EMAG'79, Inst. Phys. Conf. Series (1980). Chapter 1. P.49.

Ed. T. Mulvey.

James, M. L., Smith, G. M. and Wolford, J. C. (1967)

APPLIED NUMERICAL METHODS FOR DIGITAL COMPUTATION WITH FORTRAN.

International Textbook Company, Scranton, Pennsylvania.

Kasper, E. and Lenz, F. (1980)

'NUMERICAL METHODS IN GEOMETRICAL ELECTRON OPTICS'

in: Electron Microscopy 1980, vol.1.

Seventh European Congress on Electron Microscopy. P.10.

Eds. P. Brederoo and G. Boom (Seventh European Congress on Electron Microscopy Foundation, Leiden 1980)

Marai, F. Z. A. (1977)

Ph.D. Thesis. The Department of Physics, The Unvirsity of Aston in Birmingham.

Mulvey, T. and Nasr, H. (1980a)

'LIMITATIONS OF THE FINITE ELEMENT METHOD'

EMAG'79, Inst. Phys. Conf. Series (1980). Chapter 1. P.53.

Ed. T. Mulvey.

Mulvey, T. and Nasr, H. (1980b)

'AN IMPROVED FINITE ELEMENT PROGRAM FOR CALCULATING THE FIELD DISTRIBUTION IN MAGNETIC LENSES'

in: Electron Microscopy 1980, vol.1.

Seventh European Congress on Electron Microscopy. P.64.

Eds. P. Brederoo and G. Boom (Seventh European Congress on Electron Microscopy Foundation, Leiden 1980)

Mulvey, T. and Nasr, H. (1981)

'AN IMPROVED FINITE ELEMENT METHOD FOR CALCULATING THE MAGNETIC FIELD DISTRIBUTION IN MAGNETIC ELECTRON LENSES AND ELECTROMAGNETS'

Journal of Nuclear Instruments and Methods, 1981 (in press)

North-Holland Publishing Company.

Munro, E. (1970)

'COMPUTER-AIDED DESIGN OF MAGNETIC ELECTRON LENSES USING THE FINITE-ELEMENT METHOD'

Microscopie Electronique 1970, vol.II. Physique, P.55.

Ed. P. Favard. Societe Francais de Microscopie Electronique, Paris.

Munro, E. (1971)

Ph.D. Thesis, University of Cambridge.

Munro, E. (1973)

'COMPUTER AIDED DESIGN OF ELECTRON LENSES BY THE FINITE ELEMENT METHOD'

IMAGE PROCESSING AND COMPUTER-AIDED DESIGN IN ELECTRON OPTICS, P.284. (Ed. P. W. Hawkes), Academic Press.

Munro, E. (1975)

A SET OF COMPUTER PROGRAMS FOR CALCULATING THE PROPERTIES OF ELECTRON LENSES. Department of Engineering, University of Cambridge.

Nasr, H. (1978)

MSc Project, Department of Physics, The University of Aston in Birmingham.

Newman, M. J., Trowbridge, C. W. and Turner, L. R. (1972)

'GFUN: AN INTERACTIVE PROGRAM AS AN AID TO MAGNET DESIGN'

Proc. 4th. Int. Conf. on Magnet Technology, Brookhaven, P.117.

Pugh, E. M. and Pugh, E. W. (1970)

PRINCIPLES OF ELECTRICITY AND MAGNETISM, 2nd edition,

Addison-Wesley Publishing Company.

Shampine, L. F. and Allen, R. C. (1973)

NUMERICAL COMPUTING: AN INTRODUCTION

W. B. Saunders Company, London.

Silvester, P. and Chari, M. V. K. (1970)

'FINITE ELEMENT SOLUTION OF SATURABLE MAGNETIC FIELD PROBLEMS'

I.E.E.E., PAS (1970), vol.(PAS-89), P.1642.

Zienkiewicz, O. C. and Cheung, Y. K. (1965)

'FINITE ELEMENTS IN THE SOLUTION OF FIELD PROBLEMS'

The Engineer, vol.220, P.507.